The Polar Transmitter: Analysis and Algorithms

Von der Fakultät Informatik, Elektrotechnik und Informationstechnik
der Universität Stuttgart
zur Erlangung der Würde eines Doktor-Ingenieurs (Dr.-Ing.)
genehmigte Abhandlung

Vorgelegt von
Mohamed Abolfadl Ibrahim
aus Al Baha, Saudi-Arabien

Hauptberichter:	Prof. Dr.-Ing. Bin Yang
Mitberichter:	Prof. Dr. techn. Mario Huemer
Tag der mündlichen Prüfung:	20.10.2015

Institut für Signalverarbeitung und Systemtheorie
der Universität Stuttgart

2015

Acknowledgements

I would like to sincerely thank Prof. Dr.-Ing. Bin Yang for providing me the opportunity to write my Bachelor's, Master's, and PhD theses at his group. While working with Prof. Yang, I have received tremendous amount of technical and non-technical support. His doors were always opened at any time for any discussion.
A huge amount of gratitude goes to Dr.-Ing. Andreas Menkhoff and Intel Mobile Communications. Over the three years time I spent with Dr. Menkhoff at Intel Mobile Communications, I have learnt how to apply theoretical concepts to realizable circuits in the simplest manor. I enjoyed conversations with Dr. Menkhoff in Intel's restaurant about ethical engineering, politics, and the beyond next generation of wireless communications.
Thanks for all my colleagues at ISS, especially Martin Kreissig for his cheerful spirit and for guiding me through my first days at ISS. I would like to thank Elisabeth Fellmann for helping me out with numerous paper work at the institute. I enjoyed the hours of conversation with Dr. Christoph Zeile about history and politics. Thanks to my friends Ahmed Samhout and Mohamed Adel for filling the weekends with memorable events.
On the personal level, I would like to thank my mother, Dr. Ghada Sayed, and my father, Dr. Amr Abolfadl for urging me to work towards a Dr. title at a young age. Without their immense support from Cairo to Stuttgart, nothing would have been possible. The best way to thank my parents is to say: "Thanks for your genes".
Last but not least, a warm thanks goes to the person who provided me a huge moral support. The person who blessed me with a warm atmosphere of compassion. The person whom I discovered the 6 continents of the world with. Thanks Amina.

Contents

Notation and abbreviations

Mathematical operations

$*$	linear convolution
$\lvert \cdot \rvert$	absolute value of scalar
$(\cdot)^*$	complex conjugate
$E(\cdot)$	expectation
$E_x(\cdot)$	conditioned expectation on x
$\mathcal{F}\{\cdot\}$	Fourier transform
$p(\cdot)$	probability
$Q(\cdot)$	quantization
$Q_a(\cdot)$	amplitude quantization in DAC oversampling
$Q_p(\cdot)$	phase quantization in DAC oversampling
$Var(\cdot)$	variance
r_{xx}	autocorrelation function of x
R_{xx}	power spectral density of x
C_{xx}	covariance spectrum of x
σ_x^2	variance of x

Symbols

a_i	i-th complex baseband symbol
$a_{i,j}$	complex OFDM symbol at the i-th sub-carrier during the j-th OFDM frame
A	amplitude of DTC or DCO output

$\breve{A}_m$	amplitude of the m-th rectangular error pulse
$\breve{b}_j$	information bit stream
$\bar{b}$	binary representation of $r[n]$
b_{os}	number of bits used to set the quantization levels of DAC oversampling
$B_{spacing}$	frequency spacing between adjacent sub-carriers in an OFDM system f_b/N_u
B_N	notch width
$\breve{d}_a$	quantized $\breve{\theta}$ for clock generation in amplitude quantization DAC oversampling
$\breve{d}_p$	quantized $\breve{\theta}$ for clock generation in phase quantization DAC oversampling
$\breve{d}$	time quantization error pulse duration
$\breve{d}_d$	distorted time quantization erro pulse duration
D	time quantization error pulse duration
$\hat{e}_r$	aggregation of radius quantization and all DAC distortions error
e_p	repartitioning error
e_{qa}	quantization error in amplitude quantization
e_{qp}	quantization error in phase quantization
e_c	cosine approximation error
e_r	radius quantization error
e_θ	phase quantization error
e_s	additive polar quantization error
$\tilde{e}_r$	filtered radius quantization noise
$\tilde{e}_\theta$	filtered phase quantization noise
$\breve{e}$	quantization noise when quantizing x
$\tilde{e}_{FB}$	noise shaped quantization noise when using feedback noise shaping

$\tilde{e}$	noise shaped quantization noise when using feedforward noise shaping
$\bar{e}$	time quantization error of DTC
$\tilde{E}_n$	DTFT bin of $\tilde{e}$ at the n-th sample
f_b	Baud rate
f_{IF}	intermediate frequency
f_c	carrier frequency
f_s	sampling rate
f_l	sampling rate of DAC
f_{eff}	effective sampling rate when using DAC oversampling
$g_{i,j}$	pulse shaping filter of i-th sub-carrier during the j-th OFDM frame
$G(\omega)$	spectrum of pulse shaping filter
$G(z)$	z-transform of pulse shaping filter
h_{DAC}	impulse response of DAC
h_{DAC}^{DDavr}	impulse response of data dependent DAC
h_a	analog filter to fprce s to abide to spectral mask
h_i	filter of in-phase component
h_q	filter of quadrature-phase component
h_r	filter of radius signal
h_θ	filter of phase signal
H_{FB}	frequency response of feedback noise shaping filter
H_{IF}	z-transform of intermediate frequency bandpass filter
$\tilde{H}_r$	frequency response of radius quantization error filter
$\tilde{H}_\theta$	frequency response of phase quantization error filter
i	in-phase component
i_i	real part of i-th complex baseband signal
$\tilde{i}_\beta^\lambda$	noise shaped in-phase component using the parameters β and λ

$I_o(z)$	Modified Bessel function of 1st kind
$\jmath$	imaginary unit $\sqrt{-1}$
$\bar{l}_s$	quantization levels of amplitude quantization
$\bar{l}_p$	quantization levels of phase quantization
L	word-length of radius signal
L_p	number of levels of $\bar{l}_p$ in phase quantization
L_a	number of levels of $\bar{l}_s$ in amplitude quantization
$\breve{m}$	complex phasor $e^{\jmath\theta}$
m	theoretical phase modulated signal $\cos(\omega_c t + \theta(t))$
$\dot{m}$	$\cos(\theta)$
$\mathring{m}$	output of DCO
$\bar{m}$	output of DTC
$\bar{m}_o$	time quantization free DTC output
M	interpolation rate f_s/f_b
N_{OS}	DAC oversampling factor
N_u	number of sub-carriers in OFDM system
q	quadrature-phase component
q_i	imaginary part of i-th complex baseband signal
q_o	quantization step
$\tilde{q}_\beta^\lambda$	noise shaped quadrature-phase component using the parameters β and λ
q_{DAC}	smallest amplitude change a DAC can support
q_a	quantization step in DAC oversampling
$\hat{q}$	transmitted time quantization error with radius distortions
$\bar{q}$	transmitted time quantization error $r(t)\bar{e}(t)$
$\bar{\bar{q}}$	transmit time quantization noise when having averaged radius
$\tilde{\tilde{\mathrm{q}}}$	distorted transmit time quantization noise

r	amplitude of a complex signal
r_{notch}	notch width control parameter of IIR second order notch filter
$\tilde{r}_{\beta}^{\lambda}$	noise shaped radius using the parameters β and λ
r_p	repartitioned radius signal in DAC oversampling
$\hat{r}_p$	repartitioned radius signal with repartitioning error
$\hat{r}_r$	radius signal containing all DAC distortions
$\bar{r}$	digital averaged radius
$\hat{r}_{avr}$	analog averaged radius signal
$\hat{r}_{qa}$	radius signal in amplitude quantization
$\hat{r}_{qp}$	radius signal in phase quantization
r_f	filtered radius signal using h_r
s	theoretical transmitted signal $r(t) \cdot \cos(\omega_c t + \theta(t))$
$\check{s}$	baseband complex signal $r(t) \cdot e^{j\theta(t)}$
$\check{s}$	passband complex signal $r(t) \cdot e^{j(\omega_c t + \theta(t))}$
$\bar{s}$	transmitted signal using DTC
$\bar{s}_o$	transmitted signal using a time quantization free DTC
$\mathring{s}$	transmitted signal when using a DCO
$\check{s}_{IQ}^{\lambda\beta}$	complex baseband signal with noise shaping its IQ components using the parameters β and λ
$\check{s}_{RP}^{\lambda\beta}$	complex baseband signal with noise shaping its polar components using the parameters β and λ
$\check{s}_q$	quantized polar signal
$\hat{s}$	transmitted signal with quantized radius and time quantized DTC
$\hat{s}_r$	transmitted signal with all radius and phase distortions
$\check{s}_d$	complex baseband signal with time mismatch between radius and phase
s_{ϖ}	transmitted signal with quadrature error
$s_{\kappa_{CL}}$	transmitted signal with carrier leakage

$\tilde{s}_q$	complex baseband signal with filtered polar quantization noise
s_a	transmit signal filtered using analog filter h_a
s_f	complex signal with filtered i and q components
s_p	complex signal with filtered r and θ components
$\ddot{s}$	transmitted signal with DAC repartitioning
$\check{s}_{non-ofdm}$	baseband complex signal of an traditional pulse shaped non-OFDM transmitted
$\check{s}_{non-ofdm}$	baseband complex signal of an OFDM system
$\check{S}_{non-ofdm}(\omega)$	spectrum of non-OFDM baseband signal
T_q	quantized instant of DTC toggle
T_o	exact instant of DTC toggle
T_p	distorted instant of DTC toggle
T_s	sampling duration
T_b	symbol time
T_{frame}	OFDM frame duration
u	amplitude analog value of r
V_{DD}	supply voltage of power amplifier
x	low precision signal
x_q	quantized signal
y	noise shaped signal
β	notch width control parameter
γ	signal to quantization noise ratio defined for noise shaping
γ_o	signal to quantization noise ratio without using noise shaping
γ_b	signal to quantization noise ratio when using feedback noise shaping
γ_f	signal to quantization noise ratio when using feedforward noise shaping
ϵ_c	delay time of DTC delay element

ε	quadrature error in radians
ε_d	time mismatch between radius and phase
ε_r	radius distortion
η	instantaneous frequency
θ	phase of a complex baseband signal
θ_{av}	data-dependent DAC averaging phase
$\breve{\theta}_m$	modified phase signal for DAC oversampling $mod(\breve{\theta}(t), \pi)$
$\breve{\theta}$	modified phase signal for DAC oversampling
θ_f	filtered phase signal using h_θ
$\tilde{\theta}_\beta^\lambda$	noise shaped phase using the parameters β and λ
$\breve{\theta}$	passband phase signal $mod(\theta[n] + 2\pi\omega_c / f_s n, 2\pi) - \pi$
κ_{CL}	carrier leakage
κ_{IM}	IQ imbalance
λ	notch depth control parameter
μ_r	mean of radius
υ	instantaneous period
υ_o	exact instantaneous period
$\upsilon_{distorted}$	distorted instantaneous period
Υ	event corresponding to instantaneous period distortion
ρ	autocorrelation coefficient
ψ	modified phase signal for adaptive polar filtering $\theta[n - i] - \sum_{i=0}^{N} \theta[n - i]$
ψ_m	mapped signal ψ
ω_c	angular carrier frequency
ω_o	notch angular frequency
ω_{co}	cut-off angular frequency
ϖ	quadrature error in IQ transmitters

Abbreviations

AGC	Automatic gain control
AM	Amplitude modulation
CNR	Carrier-to-noise ratio
CORDIC	Coordinate rotation digital computer
DAC	Digital-to-analog converter
DTC	Digital-to-time converter
DTFT	Discrete time Fourier transform
DVB	Digital video broadcast
EDGE	Enhanced data rate for GSM evolution
EVM	Error vector magnitude
FFT	Fast Fourier transform
FIR	Finite impulse response
FM	Frequency modulation
GPS	Global positioning service
GSM	Global system for mobile communication
Hz	Hertz
IIR	Infinite impulse response
IQ	In-phase / quadrature phase
ISI	Inter-symbol interference
LC	Inductor capacitor
LSB	Least significant bit
LTE	Long term evolution
LTE-A	Long term evolution advanced
LTI	Linear time invariant
MSB	Most significant bit
OFDM	Orthogonal frequency division modulation

PA	Power amplifier
PAPR	Peak to average power ratio
PDF	Probability density function
PLL	Phase locked loop
PM	Phase modulation
QAM	Quadrature amplitude modulation
QPSK	Quadrature phase shift keying
RF	Radio frequency
Rx	Receiver
SC-FDMA	Single carrier frequency division multiple access
SEM	Spectral emission mask
SNR	Signal-to-noise ratio
SQNR	Signal-to-quantization noise ratio
TDC	Time-to-digital converter
Tx	Transmitter
WLAN	Wireless local area network

Abstract

The polar transmitter architecture is a promising candidate for future mobile communications. It can outperform traditional IQ transmitters in terms of power efficiency and space consumption. The massive increase in bandwidth demand makes the design of the polar transmitter a challenging task. Since the polar transmitter incorporates digital signals at RF sampling rates, then signal processing principles and algorithms could be implemented to relax the physical constraints of designing the polar transmitter components. In this thesis, the polar transmitter is analyzed from the architectural point of view. Properties of the polar signals which result from the Cartesian-to-polar conversion will be investigated. Moreover, mathematical models of the polar transmitter components, as well as their distortions, will be introduced. The strict requirements imposed on the polar transmitter components will be relaxed by introducing several novel digital signal processing algorithms. The suitability of the presented algorithms will be evaluated by simulating LTE up-link signals using the polar transmitter.

Der Polar Sender-Architektur ist ein vielversprechender Kandidat für zukünftige mobilekommunikation. Es kann traditionellen IQ-Sender in Bezug auf Energieeffizienz und Platzverbrauch übertreffen . Der massive Anstieg der Bandbreitenbedarf macht das Entwurf das Polare Sender eine anspruchsvolle Aufgabe. Da die Digital Signale im Polare Sender an RF Abtastraten abgetastet sind, dann könnte Signalverarbeitung Grundsätze und Algorithmen implementiert werden, um die physikalischen Beschränkungen der Entwurf der polaren Senderkomponenten vereinfachen. In dieser Arbeit, wird die Polartransmitter vom architektonischen Standpunkt aus analysiert. Eigenschaften der Polar Signale, die von der Cartesischen zu polaren Umwandlung Ergebnis werden untersucht. Ausserdem, mathematischen Modellen der polaren Senderkomponenten, sowie deren Verzerrungen werden eingeführt. Die strengen Anforderungen an die auferlegten Polar Sender-Komponenten werden durch die Einführung von mehreren neuen Algorithmen vereinfacht. Die Eignung der angegebenen Algorithmen werden durch LTE UL Signal simulationen validiert.

1. Introduction

Communication between people is a fundamental human instinct. In the late 20th century, a massive evolution of the communication technology has dramatically changed the way people communicate. The development of the transistor played a major role in creating the mobile device, which is the overall masterpiece of the communication evolution. Since the early years of its creation, the mobile phone had to satisfy the soaring demand of 3 main aspects:

- Speed, which corresponds to the information rate.
- Compactness, which is the physical size of the device.
- Durability, which corresponds to the battery life.

With the prices of smart phones getting cheaper than 100$, and their average price falling significantly, as shown in figure 1.1b, more and more people are now able to access mobile Internet. This has led to a drastic growth of mobile Internet traffic, as shown in figure 1.1c. Statistics predict that by the year 2018, mobile Internet traffic will be nearly 17 times the traffic in 2014 as depicted in figure 1.1a. This is motivated by the fact that in some big markets like India, the Internet traffic from mobile devices has already overtaken the Internet traffic from desktop devices, as illustrated in figure 1.1d. All those facts lead to the fundamental conclusion that the future utmost challenge in mobile communications will not be in base stations, nor cellular network architecture or radio planning, but is rather developing new compact efficient mobile devices which can support the explosive market demand of data communications and specifically the three demands mentioned above.

In this thesis, we focus on one of the most critical components of the mobile device, which is the transmitter. The polar transmitter architecture is investigated from the system level, additionally novel algorithms are presented in order to facilitate the adoption of polar transmitters in future mobile communication systems.

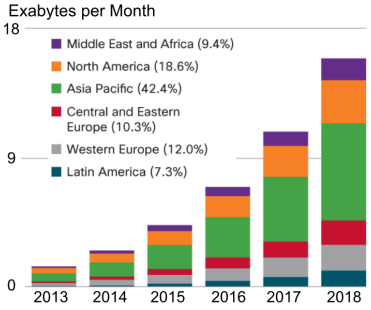

(a) Expected mobile traffic per month [Cisco, 2014]

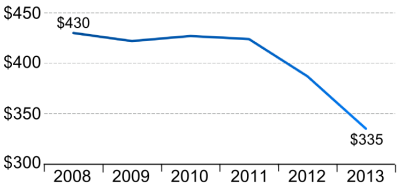

(b) Average cost of smart phones over time [Belson, 2014]

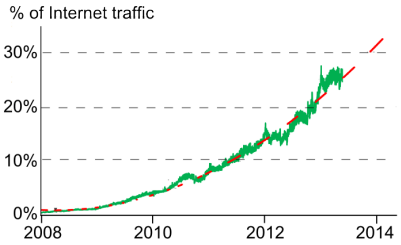

(c) Mobile traffic as % of total Internet traffic [Meeker and Wu, 2013]

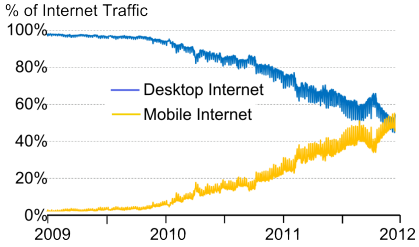

(d) Mobile traffic vs desktop traffic in India [Belson, 2014]

Figure 1.1: Statistics of mobile communications

1.1. Motivation

Since the introduction of the first mobile phone in 1973 [Cooper et al., 1975] which weighed 1.1 kg and was 32 cm long, there have been tremendous achievements in shrinking the size of the mobile phone, increasing its data rate and extending the battery life. At a point of time, mobile phone manufacturers will reach a physical limit where no further improvements and shrinkage are physically possible. The question which arises at this point is: how far are we from reaching this limit? The answer to this question is not simple and needs thorough investigation of all components of the mobile phones.

One of the most crucial components of the mobile phone which consumes a large

amount of battery power, occupies large space, and moderates the data rate is the RF front-end. Hence, it is important to analyze the RF front-end and investigate possible architectures and algorithms which can shrink the RF front-end's size, reduce its power consumption and of course align it with modern communication standards.

Traditionally, the IQ transmitter has been regarded as *de facto standard* of transmitters due to its simplicity and direct relationship to the baseband Cartesian complex signals. However, the IQ transmitter exhibited some hardware limitations in terms of shrinkage, reduction of power consumption, and scalability to multi-mode communications. This has urged hardware designers to investigate alternative architectures which could be more shrinkable and power efficient.

The polar transmitter has offered itself as a promising architecture to overtake the long term dominance of the IQ transmitter. This is based on the fact that polar transmitters are more capable of replacing most of the analog components with digital counterparts. Digitization of the RF front-end shrinks the chip size, and reduces energy consumption considerably. Nonetheless, several challenges emerge with the adoption of the polar transmitter.

1.2. Evolution of the polar transmitter

Although the concept of polar transmitters is relatively old, there has been no significant investigation of its viability except recently. The recent works of R. Stazewski, F. Raab, D. Lie and others have revived the polar transmitter concept and made the mobile communications society reconsider the polar transmitter as a potential replacement of the IQ transmitter in mobile devices.

The research on polar transmitter has been mostly limited to hardware investigations. Valuable efforts have been exerted to design electronic components which can perform their theoretical functionality. However, research on the architectural level of the polar transmitter are relatively scarce in literature. This fact has motivated the hardware designers to acquire deep theoretical understanding of the polar transmitter and its signals, as well as solving hardware limitations using signal processing algorithms. The thesis in hand is a humble effort to fulfill those requirements. By the end of this thesis, the reader should acquire two main outcomes:

- A theoretical understanding of the properties of the polar signals and their distortions, as well as mathematical modeling of the hardware components.
- Understanding of novel signal processing algorithms which relax the hard limitations imposed on various hardware components of the polar transmitter.

1.3. Contributions

This thesis analyzes the polar transmitter from an architectural point of view. The functions of each block in the polar transmitter are investigated and different implementations in literature are briefly considered. The novel contributions in this thesis can be divided into 2 main classes: Theoretical contributions, and practical contributions. The details of those contributions can be summarized as follows.

1.3.1. Theoretical contributions

The transmitted signal can be represented as

$$\begin{aligned} s(t) &= i(t)\cos(\omega_c t) - q(t)\sin(\omega_c t) \\ &= r(t)\cos(\omega_c t + \theta(t)) \end{aligned} \tag{1.1}$$

with

$$r(t) = \sqrt{i^2(t) + q^2(t)} \quad , \quad \theta(t) = \arctan\left(\frac{q(t)}{i(t)}\right) . \tag{1.2}$$

where $\arctan(\cdot)$ yields the 2π version of $\arctan(\cdot)$. The properties of the Cartesian signals $i(t)$ and $q(t)$ are well known from literature. However, the non-linear conversion from the Cartesian domain to the polar domain shown in equation (1.2) introduces new characteristics to the polar signals $r(t)$ and $\theta(t)$. The theoretical contributions of this thesis consider the properties of the polar signals and can be summarized as follows:

Theoretical analysis of polar signals

Before applying signal processing algorithms to the polar signals, we need to have a deep understanding of the statistical and spectral properties of the polar signals. For example, choosing an appropriate sampling rate for the polar signals requires the knowledge of the Nyquist frequency of the polar signals. A theoretical study of the polar signals' properties are summarized in chapter 3.

As mentioned earlier, the polar transmitter digitizes the RF front-end. The digitization of polar signals introduces quantization noise. The theoretical effect of quantization noise in the polar domain on the spectrum of the complex signal will be presented in section 3.4 [1].

[1] The contributions done in chapter 3 are done by B. Yang. The author contributed with simulations which verified the theoretical analysis done by B. Yang.

Time/frequency quantization analysis

Time/frequency quantization is one of the basic limitations of polar transmitters, as it has direct influence on the spectrum of the transmitted signal and consequently limits the adoption of polar transmitters. In section 4.4, a theoretical analysis of the influence of time/frequency quantization on the spectrum of the transmitted signal is presented [2].

1.3.2. Practical contributions

Polar transmitters were ideally fitted for modulation techniques which have a constant amplitude such as GSM. With the growing need to have higher spectral efficiency, amplitude modulation became coupled with phase modulation in modern communication standards. Polar transmitters were reported to exhibit a poor performance for communication standards having amplitude modulation. Specifically, the out-of-band noise of the transmitted signal using polar transmitters is relatively high. Hence, signal processing algorithms are needed in order to filter and suppress the out-of-band noise in polar transmitters. The following novel algorithms are presented in this thesis to counteract the excessive out-of-band noise in polar transmitters.

Digital-to-Analog Converter oversampling

In section 5.4, a novel algorithm is presented which processes the digital radius signal $r[n]$ fed into the Digital-to-Analog Converter (DAC) in order to suppress the overall out-of-band noise.

Feedforward noise shaping

Quantization noise shaping has been traditionally done using *feedback* structures such as the sigma-delta noise shaping circuit [Norsworthy et al., 1997]. In chapter 6, a novel approach to shape the quantization noise using a *feedforward* structure will be presented. The approach offers the flexibility of easily controlling the shape of the notch in the noise shaped signal by tuning single scalar parameters rather than changing filter coefficients as done in the feedback approach.

[2] The theoretical approach of deriving the time/frequency quantization was done by the author. However, B. Yang assisted the author with refining the absolute value of the spectrum of the time /frequency quantization.

Polar predistortion

Filtering the Cartesian signals $i(t)$ and $q(t)$ results in a complex signal $s(t) = i(t) + \jmath q(t)$ [3] which has similar spectral shape as $i(t)$ and $q(t)$ given that $i(t)$ and $q(t)$ are uncorrelated. Filtering the polar signals $r(t)$ and $\theta(t)$ in $s(t) = r(t)e^{\jmath\theta(t)}$ does not yield the same effect as filtering the Cartesian signals. In section 7.2, a novel adaptive filtering algorithm will be presented which filters the polar signals in order to yield a similar spectral shape as filtering in the Cartesian domain. In section 7.3, another novel predistortion algorithm is introduced which filters the time quantization error in polar transmitters by predistorting the polar signals before the digital-to-analog conversion.

1.4. Thesis guide

This thesis starts with the basics of the current IQ transmitters and highlights their drawbacks in chapter 2. Based on those drawbacks the polar architecture is introduced in chapter 2 as well. Afterwards, the theoretical contributions of this thesis mentioned earlier are summarized in chapter 3. Similar to the IQ transmitter, the polar transmitter has 2 main branches, the radius branch and the phase branch. For each branch a chapter is dedicated, chapter 4 analyzes the phase branch and chapter 5 analyzes the radius branch. Each of those chapters considers all signal processing steps starting from the generation of the digital polar signals, all the way till the transmission of the passband analog signal. Later in chapter 6, the novel feedforward noise shaping approach is presented with its possible application to communication systems. Two polar predistortion algorithms are then presented in chapter 7. Finally, a summary of the work as well as a future outlook is given in chapter 8.

Please note that after presenting a concrete structure of the polar transmitter in chapter 2, a more detailed overview of the thesis will be illustrated in figure 2.9.

[3] Note that throughout this thesis the symbol $\jmath$ will be used to represent the imaginary unit $\jmath = \sqrt{-1}$.

2. IQ transmitters vs polar transmitters

This chapter highlights the main motivation to adopt polar transmitters instead of IQ transmitters. In section 2.1, the main disadvantages of the IQ transmitters are highlighted. Afterwards in section 2.2, the polar transmitter architecture is described together with an explanation of the superiority of the polar transmitters over IQ transmitters. Finally, in section 2.3, the most significant challenges in the polar transmitters are listed.

2.1. IQ transmitter and common transmitter artifacts

A typical IQ transmitter can be shown in figure 2.1. A symbol encoder converts the input bit stream $\check{b}_j$ into complex symbols a_i. The real part i_i and the imaginary part q_i are split into two separate paths. The symbols operate at the Baud rate f_b. The symbols are then up-sampled to a sampling rate $f_s = M \cdot f_b$ by inserting $M - 1$ zeros between each 2 consecutive samples. Then the up-sampled signal is pulse-shaped using a filter $G(z)$. The digital outputs of the filter, $i[n]$ and $q[n]$, are then converted into an analog signal using a DAC. Up to this point $i(t)$ and $q(t)$ undergo identical signal processing operations. $i(t)$ is then multiplied by $\cos(2\pi f_{IF} t)$ and $q(t)$ is multiplied by $-\sin(2\pi f_{IF} t)$, where f_{IF} is an intermediate frequency which is less than the carrier frequency f_c. The output of both products are then summed up and the sum is filtered using an analog bandpass filter which removes the undesired out-of-band noise. The resultant signal is then up-converted to the passband frequency f_c and finally amplified using a power amplifier PA and transmitted through the antenna.

Traditionally, the pulse shaping filter $G(z)$ is implemented as an analog component and is placed after the DAC. However, a digital filter occupies less space than an analog one, therefore the filtering is done in the digital domain as depicted in figure 2.1.

Contrary to the previously explained hypothetical signal flow, a real IQ transmitter introduces several distortions. The imperfections of the transmitter are combined with channel aberrations to yield a signal at the receiver side which can be severely distorted. The distortions introduced by the channel are generally unpredictable and cannot be controlled by the transmitter. However, transmitter imperfections can be reduced by

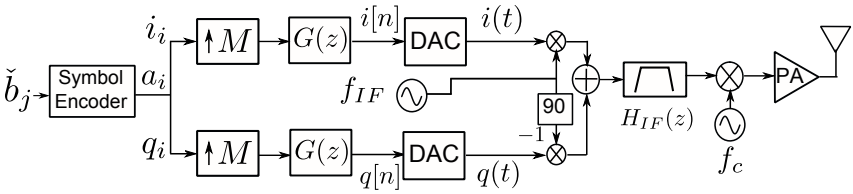

Figure 2.1: Basic IQ transmitter block diagram

signal processing approaches or hardware improvements. In the coming section, an overview about the most important transmitter imperfections in the IQ transmitter will be shortly discussed.

2.1.1. Carrier leakage

Theoretically, the analog Cartesian signals $i(t)$ and $q(t)$ have a zero mean. However, due to some hardware imperfections, a DC component might be included in one or both of the baseband Cartesian signals. When the Cartesian signals are modulated by multiplication with the carrier, the DC component *leaks* the carrier into the transmitted signal. Assuming that a DC component κ_{CL} is added to $i(t)$, then the transmitted signal can be represented as

$$\begin{aligned} s_{\kappa_{CL}}(t) &= (i(t) + \kappa_{CL}) \cdot \cos(\omega_c t) - q(t) \cdot \sin(\omega_c t) \\ &= i(t) \cdot \cos(\omega_c t) - q(t) \cdot \sin(\omega_c t) + \kappa_{CL} \cdot \cos(\omega_c t) \ . \end{aligned} \tag{2.1}$$

As shown in equation (2.1), the transmitted signal has a certain tone at the carrier frequency ω_c whose power is controlled by the DC component κ_{CL}. This tone can violate the spectral mask, and also mix with other antenna distortions which produces in-band distortion noise. Figure 2.2 shows the effect of carrier leakage on the constellation diagram (figure 2.2a) and on the spectrum of the transmitted signal (figure 2.2b). In this case, QPSK is used as the modulation scheme. As shown, the constellation diagram is shifted slightly to the positive real axis direction due to the presence of κ_{CL} in $i(t)$. In the spectrum, there is a spike at $f = f_c$ due to the presence of the carrier in the transmitted signal.

2.1.2. IQ imbalance

Theoretically, $i(t)$ and $q(t)$ signals undergo identical signal processing blocks except for a 90 degrees phase shift between the carrier signals. In practice, this is not necessarily

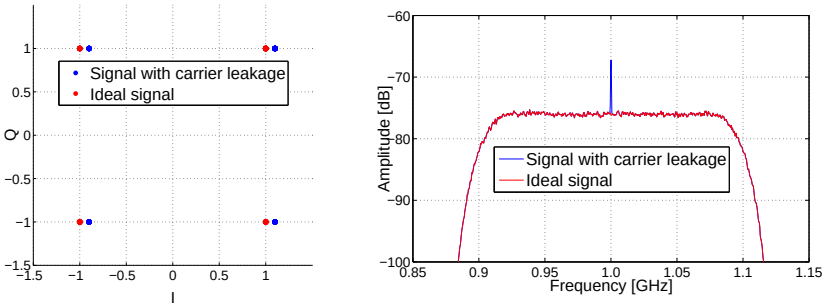

(a) (b)

Figure 2.2: Constellation diagram and spectrum of transmitted signal with carrier leakage at the in-phase branch

true. It is quite common that the gain of the $i(t)$ and $q(t)$ paths are different. This results in a distorted constellation diagram. IQ imbalance occurs usually due to DAC gain mismatch. Figure 2.3 shows the effect of IQ imbalance on the constellation diagram and the spectrum of the transmitted signal when $i(t)$ has a gain of $\kappa_{IM} = 0.75$ and $q(t)$ has a gain of 1. The constellation in 2.3a becomes rectangular rather than the ideal square shaped. The spectral level of the transmitted signal is slightly reduced as the power of the in-phase component is reduced by the factor κ_{IM}.

2.1.3. Amplitude-Amplitude distortion

Mobile devices need to transmit a high power signal to reach the base stations. The low voltage signal in the transmitter is amplified using a PA. A theoretical PA should have a linear transfer function with a slope greater than one for amplification. In reality this is not the case. The transfer function of the PA is divided into two regions as shown in figure 2.4c, a linear but power non-efficient region for the input in the range 0 to 1.5, and a non-linear but power efficient region for input greater than 1.5. PA linearization is an on-going research topic and there are several approaches to overcome the trade-off between linearity and energy efficiency.

Figure 2.4a shows the track taken on a constellation diagram when the PA is ideal and has a linear fixed amplification factor of 100. In figure 2.4b, the track when a real PA is used to amplify the low voltage signal is shown. It is observable that the complex track using a real PA is compressed into a circular shape. The effect of the non-ideal

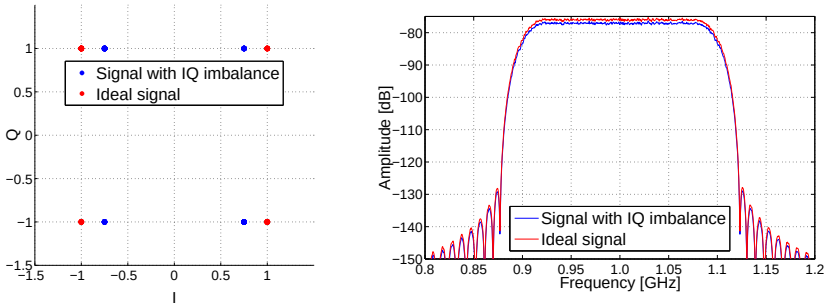

(a) (b)

Figure 2.3: Constellation diagram and spectrum of transmitted signal with IQ imbalance

PA on the spectrum is shown in figure 2.4d. As shown, the out-of-band noise increases considerably.

2.1.4. Quadrature error

In figure 2.1, it is shown that there is a 90 degrees phase shift between the carriers of the $i(t)$ and the $q(t)$ branches. In practice, this cannot be guaranteed. There will always be a carrier *spill* from the real to the imaginary part or vice-versa. This carrier spill is formally defined as quadrature error. Assume that there is a time varying phase error $\varpi(t)$ between the oscillators modulating $i(t)$ and $q(t)$, then the transmitted signal can be represented as

$$\begin{aligned} s_{\varpi}(t) &= i(t) \cdot \cos(\omega_c t + \varpi(t)) - q(t) \cdot \sin(\omega_c t) \\ &= i(t) \cdot (\cos(\omega_c t) \cdot \cos(\varpi(t)) - \sin(\omega_c t) \cdot \sin(\varpi(t))) - q(t) \cdot \sin(\omega_c t) \quad .(2.2) \end{aligned}$$

Assuming that the phase shift is small enough $\varpi(t) \ll \pi/2$, then we can assume $\sin(\varpi(t)) \approx \varpi(t)$ and $\cos(\varpi(t)) \approx 1$. Therefore, equation (2.2) becomes

$$s_{\varpi}(t) \approx i(t) \cdot \cos(\omega_c t) - (q(t) + i(t)\varpi(t)) \sin(\omega_c t) \; . \tag{2.3}$$

This shows that a small part of the information in $i(t)$ spills into the quadrature phase channel which distorts the transmitted signal. Figure 2.5a shows the constellation diagram of a QPSK signal with a fixed phase error $\varpi(t) = 0.087$ radians. As shown, the constellation diagram shifts from being square shaped to a parallelogram shape. However, the power spectral density of the transmitted signal shown in figure 2.5b does not

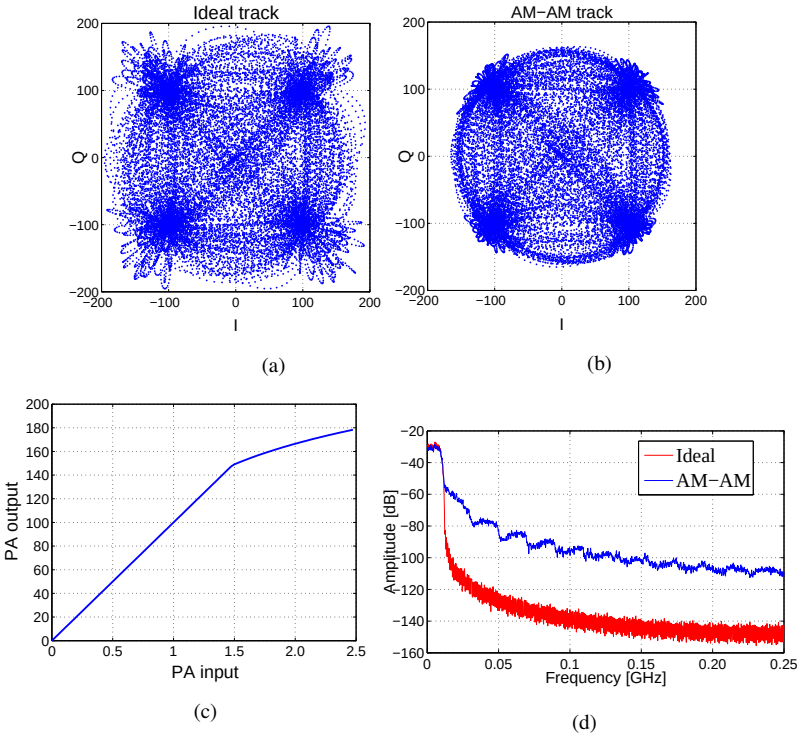

Figure 2.4: Effect of AM-AM distortion on complex track and spectrum of transmitted signal (a) and (b). Typical power amplifier transfer function (c). Single-sided spectrum (equivalent baseband) (d)

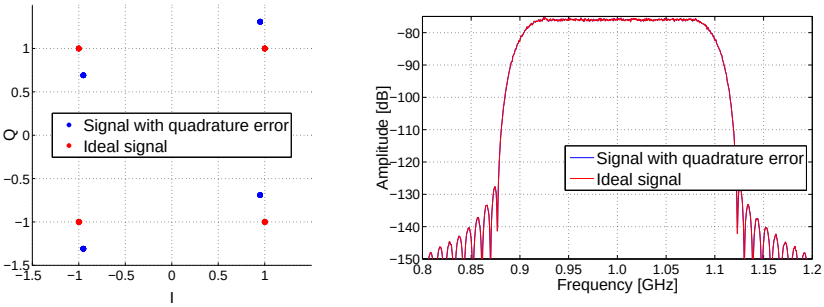

(a) (b)

Figure 2.5: Constellation diagram and spectrum of transmitted signal with quadrature error

change. Note that $\varpi(t)$ is usually a random variable which continuously distorts the constellation of the transmitted signal.

2.1.5. Path difference delay

In practical IQ transmitters, the $i(t)$ and the $q(t)$ branches may have non-equal delay for processing the signals. This means that when summing both signals, $i(t)$ and $q(t)$ might not be synchronized. From the spectrum point of view, the path difference delay will not have an effect on the transmitted signal power spectral density, since $i(t)$ and $q(t)$ are uncorrelated in modern communication systems (ie. OFDM), and therefore their spectra are simply added. However, the path difference delay may lead to loss of synchronization between the transmitter and receiver clocks. If $i(t)$ is slightly delayed compared to the $q(t)$, then the receiver will sample $i(t)$ too early and the synchronization is shifted between the transmitter and receiver. Figure 2.6 shows an ideal and a delayed signal at the receiver. Since we are using QPSK, then the $i(t)$ should be ± 1 at the symbol sampling rate f_b. However, as we can see at the sampling instant $t = 1$, the delayed signal is more than 1. If we use high M-QAM modulation techniques, then the path delay will become more serious and will lead to modulation errors.

2.1.6. General limitations of the IQ transmitter

Although the previously stated imperfections can be mitigated in several ways, there are still some major restrictions which limit the usability of IQ transmitters for future

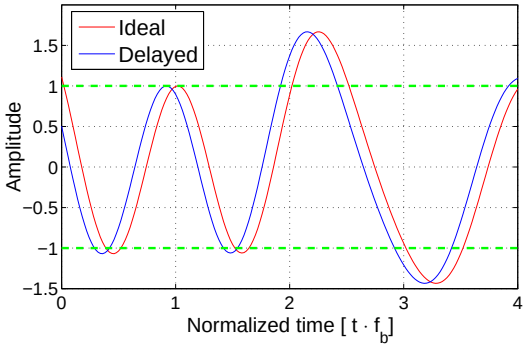

Figure 2.6: Ideal and path delayed signals

data, energy and space requirements. Considering figure 2.1, it is clear that the IQ transmitter contains a considerable amount of analog components: 3 mixers, 2 DACs, 3 analog multipliers, 2 local oscillators at f_{IF} and f_c. Moreover, other components such as PLL and analog PA pre-distorter were not included. Those analog components occupy large space, and since space is actually very scarce in mobile devices, it is highly desirable to *shrink* the analog components or replace them with digital components.

For the past decade, digital components shrank significantly compared to their analog counterparts. This fact proofs Gordon Moore's (Intel co-founder) famous statement "*The number of transistors incorporated in a chip will approximately double every 24 months*". Figure 2.7 shows the number of transistors within some Intel microprocessors over time. The increasing number of transistors confirm Moore's law. The main reason that more transistors can be packed in smaller area is that the transistor gate length is getting shorter. Moreover, the cost of transistors has dropped significantly over time as shown in figure 2.8.

On the other hand, if we consider analog circuits, it is observed that analog circuits do not shrink (if at all) as much as digital circuits. This implies, that if we want to shrink the transmitter size, we need to replace the analog components with digital components. This has been done for the pulse shaping filter which is nowadays mostly implemented in the digital domain. However, other analog components such as mixers, oscillators, and multipliers cannot be replaced by digital circuits. Those limitations restrict the usability of IQ transmitters for future highly demanding communication requirements.

Another limitation of having a significant amount of analog components is the integrability with the application processor. In mobile devices, there is an application proces-

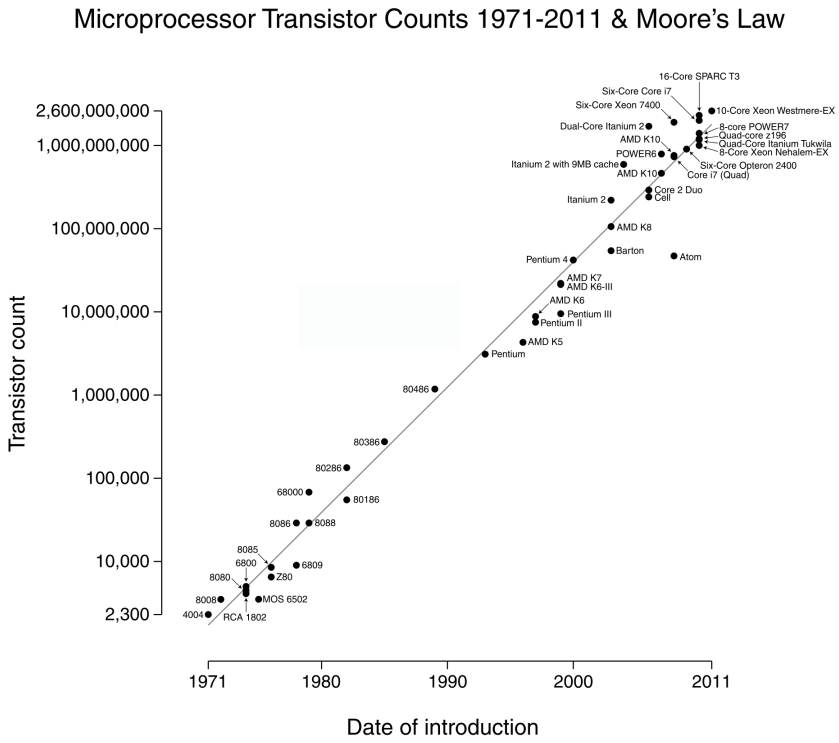

Figure 2.7: Actual number of transistors in Intel products [Moore]

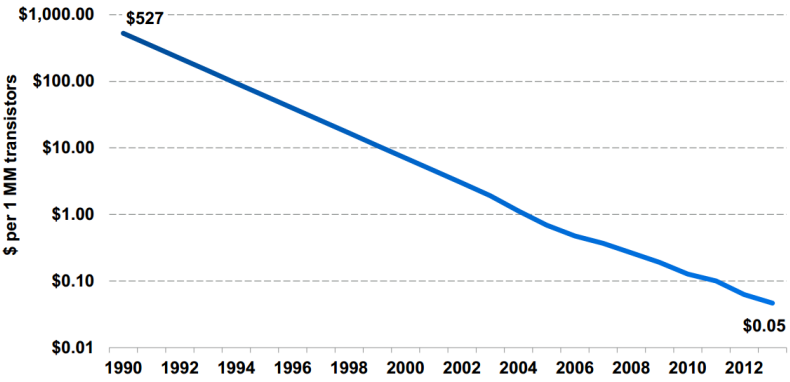

Figure 2.8: Cost of 1 mm^2 of transistors over time [Belson, 2014]

sor which is responsible of running services on the handset such as games, applications, and the operating system. Additionally, there is a communication modem which contains a baseband processor and an RF-front end for wireless communications. It is highly desirable to integrate both the application processor and the modem on a single die. This would save a significant amount of space. However, this integration requires that the modem will contain mostly digital components which share with the application processor a single clock signal. Due to the presence of analog components in IQ transmitters, this integration is difficult to achieve.

The final main limitation of IQ transmitters is the multi-modal functionality of the modem. In the first days of mobile communications, the data transmitted was mostly voice. The carrier frequencies at that time were around 1 and 2 GHz. Nowadays, there are a lot of protocols which the handset should support such as WLAN, Bluetooth, GPS, and DVB. Each protocol operates at a different carrier frequency. In IQ transmitters, there is a dedicated local oscillator for each carrier frequency (mode). This approach was acceptable for some time when the number of modes were limited. But with the growing number of different protocols, we can forecast that in the future a multi-modal transmitter which has a single high frequency oscillator will be favored which can support several carrier frequencies without the need to dedicate an oscillator for each communication protocol.

So far, the main limitations of the IQ transmitter were highlighted. In the next section, the basics of the polar transmitter are presented. Whenever applicable, we will highlight the polar transmitter features which counteract the imperfections of the IQ transmitter explained above.

2.2. Fundamentals of the polar transmitter

The polar transmitter is a promising candidate for transmitters which tries to overcome most of the imperfections incurred in the IQ transmitter. In this section, a fundamental overview about the polar transmitter from the architectural point of view will be discussed. we also explain the main reasons why the polar transmitter can outperform the IQ transmitter.

2.2.1. Block diagram

Theoretically, the polar transmitter should transmit the same signal as the IQ transmitter. However, the method of generating the signal is completely different. The polar transmitter generates the passband signal in the form of

$$s(t) \quad = \quad r(t)\cos(\omega_c t + \theta(t)) \ . \tag{2.4}$$

Figure 2.9 shows a general block diagram of the polar transmitter. Similar to the IQ transmitter, the symbol encoder generates baseband complex symbols defined as

$$a_j \quad = \quad i_j + jq_j \ , \tag{2.5}$$

which operate at the Baud rate f_b. The pulse shaping is done to limit the spectrum of the baseband signal by up-sampling a_j by a factor of $M = f_s/f_b$ followed by a digital pulse shaping filter. The resultant signal can be represented as

$$\check{s}[n] \quad = \quad i[n] + jq[n] \ . \tag{2.6}$$

The complex digital Cartesian signal $\check{s}$ is then converted to the polar domain using a CORDIC module which generates the digital polar signals $r[n]$ and $\theta[n]$ where

$$r[n] \quad = \quad \sqrt{i^2[n] + q^2[n]}, \quad \theta[n] = \arctan\left(\frac{q[n]}{i[n]}\right) \ . \tag{2.7}$$

In this structure the digital radius $r[n]$ is converted into an analog radius signal $r(t)$ using a DAC. In the phase branch, there are two possible variants of the polar transmitters:

- Digitally Controlled Oscillator (DCO) based polar transmitter: In this variant, the instantaneous frequency $\eta[m]$ is calculated from the phase signal $\theta[n]$. $\eta[m]$ is then fed into the DCO which generates a cascade of continuous-time cosine waves $\mathring{m}(t)$ with each cycle having a frequency equal to the input instantaneous frequency $\eta[m]$. $\mathring{m}(t)$ is then multiplied with the radius signal which yields the transmitted signal represented as

$$\mathring{s}(t) \quad = \quad r(t)\mathring{m}(t) \ . \tag{2.8}$$

- Digital to Time Converter (DTC) based polar transmitter: In this variant, the instantaneous period $\upsilon[m]$ is calculated from the phase signal $\theta[n]$. $\upsilon[m]$ is then fed into the DTC which generates a cascade of continuous-time square waves with each cycle having a period equal to the input instantaneous period $\upsilon[m]$. $\bar{m}(t)$ is then multiplied with the radius signal which yields the transmitted signal represented as

$$\bar{s}(t) \quad = \quad r(t)\bar{m}(t) \; . \tag{2.9}$$

Both DCO and DTC are tuned to a certain carrier frequency f_c, and the perturbations of the instantaneous frequency/period occur due to the modulation done by the baseband phase signal $\theta[n]$. After yielding $\bar{s}(t)$ or $\mathring{s}(t)$, the signal is amplified using a PA and transmitted over the antenna.

The DTC based polar transmitter is considered a newer concept and has some advantages over DCO. Specifically it is more digital than the DCO. This will be discussed in details in chapter 4. In figure 2.9, a processing block before the DTC and DAC is shown. This block contains possible algorithms to improve the spectrum of the transmitted signal by introducing notches or suppressing the out-of-band noise.

The organization of the thesis can now be clearly seen in figure 2.9. In chapter 3, the theoretical properties of the polar signals based on the non-linear conversion from Cartesian-to-polar coordinates done by the CORDIC are discussed. In chapter 4, we investigate the processing blocks in the phase branch. In chapter 5, we investigate the radius branch as well as analyze the recombination and amplification processes which occur at the PA. In chapter 6 and 7, a novel algorithms for filtering the out-of-band noise is presented. The reader is encouraged to use figure 2.9 as a guide throughout this thesis.

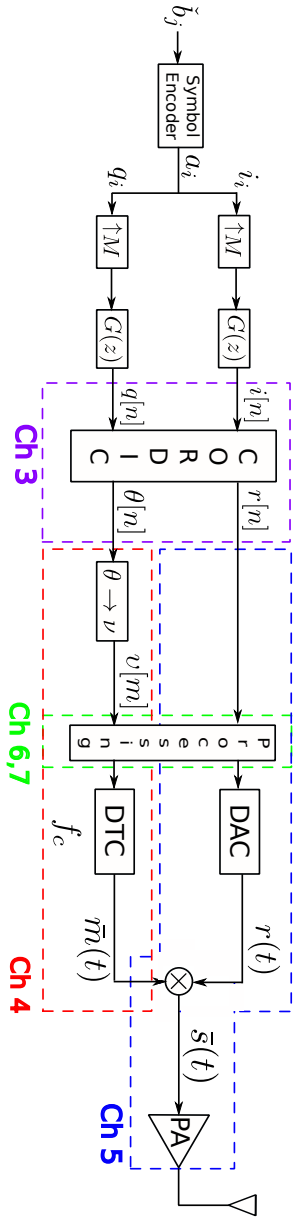

Figure 2.9: Block diagram of a DTC-based polar transmitter and thesis organization

2.2.2. Advantages over IQ transmitter

By comparing figures 2.1 and 2.9, we can see that the polar transmitter has relatively more components than the IQ transmitter. The following points summarize why the polar transmitter is advantageous compared to the IQ transmitter although it contains more components:

- **Reduction of the number of analog components**: As mentioned earlier, the IQ transmitter must contain at least the following analog components: 3 mixers, 2 DACs, 3 analog multipliers, 2 local oscillators at f_{IF} and f_c. However, the polar transmitter has only 1 DAC, and 1 DTC or DCO. The PA in the polar transmitter inherently contains the recombination process of the radius and phase branches as will be shown later in chapter 5. This is a significant reduction in the number of analog components which allows the possibility to shrink the transmitter's size. Additionally, several imperfections of the IQ transmitter are eliminated such as IQ imbalance, quadrature error, carrier leakage due to the absence of analog oscillators in the polar transmitter.

- **Efficiency**: The PA uses a large part of the overall energy consumption of the mobile device. Efficiency of the PA can be boosted by operating the PA in the non-linear region. It was shown in section 2.1.3 that operating the PA in the non-linear region introduces AM-AM distortions. In the polar transmitter, the radius signal $r(t)$ is available which is actually the amplitude of the complex signal. This enables us to power the supply voltage of the PA using the radius signal $r(t)$ and thus operate the PA in the non-linear region. The details of the relationship between the radius signal and the PA will be explained in section 5.2. Generally speaking, being able to process the amplitude of the transmitted signal is highly desirable. For example, the Peak to Average Power Ratio (PAPR) can be easily monitored from the radius signal. In addition, the Automatic Gain Control (AGC) in IQ transmitters requires the knowledge of the signal transmitted power, which is not directly available in IQ transmitters but is available in polar transmitters from the radius signal.

- **Multimode functionality**: In section 2.1.6, it was mentioned that IQ transmitters are not scalable for multi-mode communication because for each protocol we need to have a separate oscillator. However, in the polar transmitter, a single high speed clock is used as the oscillator. From this clock several lower frequency clocks can be easily derived and used for different carrier frequencies in the phase branch in the digital domain. Whereas in IQ transmitters, lower frequency oscillators can only be obtained using expensive analog filters.

- **Integrability**: Since the polar transmitter contains more digital components than the IQ transmitter, the digital RF front-end can be integrated to the baseband and the application processors. This way, the mobile device could be made more compact in size and more efficient compared to the non-integrable IQ transmitters.
- **Digital signal processing**: Having digital signals enables us to apply digital signal processing concepts to enhance signal properties. Digital filters tend to have higher accuracy compared to analog filters due to less degradation. Additionally, digital filters occupy smaller space and consume less energy than analog filters.
- **PA predistortion in radius branch**: In transmitters, there is usually a predistorter to linearize the PA's transfer function. In IQ transmitters, this is done either in the analog domain or in baseband. However, in polar transmitters, since the radius signal is available at RF sampling rates which makes the digital radius signal close to the analog signal, a predistorter block may be inserted before the DAC in order to linearize the PA.

2.3. Challenges of the polar transmitter

The advantages of the polar transmitter mentioned in the previous section come at a certain expense. In this final part of the chapter, we indicate which challenges of the polar transmitter exist. The concept of polar transmitters is highly debatable among the RF community. The main criticism of the polar transmitter is based on the fact that current RF resources cannot support the high hardware requirements of the polar transmitter. The main challenges of the polar transmitter can be listed as following:

- **High sampling rate**: The sampling rate f_s of the polar signals should be at least equal to the carrier frequency f_c. Some communication protocols such as WLAN operate at 5GHz. Having such high sampling rates which are referred to as *digital-RF*, implies maintaining an ideal clock and applying digital signal processing at such high RF-sampling rates which is challenging.
- **Time/frequency resolution of DTC/DCO**: As mentioned earlier, the DTC is driven by the instantaneous period υ. Since υ is a digital signal, the DTC is limited to a certain time resolution due to the quantized amplitude of the instantaneous period. Similarly, the DCO is limited by the frequency resolution of η. Quantizing the instantaneous period/frequency increases the out-of-band noise. It has been shown through simulations that a time accuracy in the range of 100 femto-seconds is needed in order to suppress the out-of-band noise within an ac-

ceptable level. Such fine time resolution in the range of femto seconds is difficult to attain.

- **DAC sampling rate**: Available DACs are mostly used in audio application where a sampling rate in the range of 50 kHz is sufficient. However, in polar transmitters the DAC should be able to support digital signals with a sampling rate at least equal to the carrier frequency, which could be up to $f_c \approx$ 5GHz. Such high sampling frequencies are considered challenging for current DAC specifications.

- **Interpolation in polar domain**: The CORDIC which converts the Cartesian signals to polar signals contains several processing steps. The energy consumption of the CORDIC is directly proportional to the sampling rate of the input digital signal. Therefore, it is desirable to interpolate the polar signals after the CORDIC, rather than operating the CORDIC at a high sampling rate. Interpolation of polar signals is not intuitive, as the radius and phase signals are coupled, unlike Cartesian interpolation which can be done separately for the real and imaginary parts.

- **Spectral regrowth**: It will be shown in chapter 3 that the polar signals r and θ have broader spectra compared to the spectra of i and q. This implies that the physical channel (RF waveguide) which carries the polar signals should operate at a high sampling rate in order to support the wide band polar signals. Consequently, the CORDIC should operate at a high sampling rate, which means that it will consume more energy. If the CORDIC operates at a low sampling rate, then some components of the polar spectra will be lost due to aliasing.

- **Time mismatch**: Similar to the IQ transmitter path delay mismatch mentioned in section 2.1.5, the polar transmitter is even more sensitive to the time mismatch at the recombination of the radius and the phase.

- **Spurious noise**: The fact that the polar transmitter is digitally *intensive* implies the existence of lots of quantization effects during the processing of the digital signals. This yields a considerable amount of flat out-of-band noise referred to as spurious noise.

- **Noise shaping**: In IQ transmitters, there is an analog filter before the PA responsible of suppressing the out-of-band noise as shown in figure 2.1. This analog filter can possibly introduce notches at certain frequencies where the antenna receives a down-link signal in order to reduce TxRx interference. Alternatively, one can filter $i(t)$ and $q(t)$ signals using a notch filter separately. Since the spectrum of the transmitted signal is the summation of the spectra of $i(t)$ and $q(t)$, the notches in the spectra of $i(t)$ and $q(t)$ will be conserved in the transmitted signal.

In polar transmitters, filtering the radius and phase separately does not necessarily yield a notch in the transmitted signal. This happens due to the fact that $r(t)$ and $\theta(t)$ are coupled and because the recombination of $r(t)$ and $\theta(t)$ is a nonlinear operation. This implies the need to apply advanced algorithms to process the radius and phase signals jointly in order to filter the out-of-band noise.

3. Statistical and spectral properties of polar signals

In most of the reported literature, the challenges of polar transmitters were mostly tackled from the circuits perspective. The fundamental knowledge of the spectral and statistical properties of the polar signals was limited but sufficient for narrow band communications. With the growing need for wide-band communication reaching data rates up to 1 Gbps [Ghosh et al., 2010], acquiring solid knowledge of the fundamental properties of the polar signals as well as their relationship to baseband signals became of paramount importance.

Circuit designers relied heavily on simulations and measurements to obtain their knowledge about the polar signals. As much as simulations and measurements are always possible and are close to the actual hardware, they do not give a deep understanding of the fundamental properties of the polar signals. In this chapter, an overview of the fundamentals of the polar signals from the literature is presented and applied to modern communication standards. We are specifically interested in the spectrum and distribution of the radius and phase signals.

This chapter is organized as follows: The first part recaps the reported literature about the analysis of polar signals. In the second part, the contribution of this thesis to the analysis of polar signals is presented.[1] In the third part, the theoretical results are compared to the simulations of different communication standards. Finally, the quantization of polar signals as well as filtering of quantization noise will be explained in the fourth section.

3.1. Literature

The first concept of a polar transmitter was presented in [Kahn, 1952]. However, the analysis of the radius and phase properties were presented much earlier. In 1944-1945, the statistical properties of a random wide band noise was studied [Rice, 1944][Rice, 1945]. In this work, the autocorrelation function of the current due to shot noise was

[1] Theoretical analysis has been done by B. Yang

studied for the first time by considering 2 samples of the same signal within a short time shift. In 1948, the study continued for the specific case of narrow band noise at a certain frequency [MacDonald, 1948]. The studied signal was represented as

$$s(t) \quad = \quad r(t)\cos(\omega_c t + \theta(t)) \ , \tag{3.1}$$

which is similar to the transmitted signal in its polar form. In [MacDonald, 1948], the probability density function of the phase signal for a Gaussian spectrum was investigated. In addition, the influence of the carrier frequency ω_c was investigated. The formulas for the autocorrelation and spectrum in [Rice, 1944] and [MacDonald, 1948] were rather complex. In [Price, 1955], the author used series approximation to find a simplified expression for the autocorrelation and spectrum of the radius $r(t)$ and phase modulated signal $\cos(\omega_c t + \theta(t))$.

Around 40 years later, the attention was drawn once again to polar transmitters due to the emergence of mobile communication devices where power efficiency is critical. This has induced a plethora of investigations to verify the usability of polar transmitters. In [Raab, 1996], the non-linearity of the PA in the polar transmitter was investigated through laboratory simulations. In [Rudolph, 2002] and [Rudolph, 2003], the author investigated the effect of the roll-off factor of the pulse shaping filter on the spectrum of the transmitted signal for different communication standards by means of simulations. In [Pedro et al., 2007], the author measured the non-linear effects of the polar transmitter, such as the finite bandwidth of the medium carrying the polar signals and the non-linear PA.

In this thesis, the fundamentals of polar signals in literature are to the modern communication standards. Of particular interest are the spectrum and distribution of the radius $r(t)$ and phase $\theta(t)$ signals based on the spectrum, distribution, and second order moments of the Cartesian signals $i(t)$ and $q(t)$.

3.2. Theoretical analysis

The analysis of the properties of the polar signals is not new and can be rooted to the old literature presented in section 3.1. However, some modern communication parameters such as roll-off factor were not clearly discussed in the fundamental literature.

In this section, a signal model of OFDM and non-OFDM communication systems will be described. Afterwards, the problem of deriving the theoretical properties of the polar signals will be stated. Finally an overview of the derivation of the statistical and spectral properties of polar signals will be presented.

3.2.1. Communication model

Early communication systems started with analog modulation techniques such as radio AM/FM. Digital modulation started to emerge where the baseband signal is represented as a stream of bits. If we consider the latest communication standards we can group them into two main classes: non-OFDM standards such as GSM/EDGE and OFDM systems such as LTE/DVB/WLAN. For each class we will give a signal model and explain the difference each system imposes on the statistical analysis.

Non-OFDM signal model

The baseband processor generates a series of discrete-time complex-valued symbols a_n, which are distributed according to the constellation points of the digital modulation technique. The complex symbols are convolved with a real analog pulse shaping filter $g(t)$. The output of the pulse shaping filter can be denoted as

$$\check{s}_{non-ofdm}(t) = \sum_{n=-\infty}^{\infty} a_n g(t - nT_b) = i(t) + jq(t) \tag{3.2}$$

$$= r(t)e^{j\theta(t)} = r(t)\check{m}(t) \ , \tag{3.3}$$

where T_b is the symbol period corresponding to the Baud rate $f_b = 1/T_b$. The frequency response $G(\omega)$ of the pulse shaping filter defines the spectrum $\check{S}_{non-ofdm}(\omega)$ of the complex analog signal. Usually, the spectral shape of the complex signal $\check{S}_{non-ofdm}(\omega)$ is enforced by the communication standard, and accordingly the pulse shaping filter is designed.

Ideally, the baseband signal should have a rectangular spectrum with a sharp cut-off at $f_b/2$. To realize the rectangular spectrum, we need to have an ideal Nyquist filter which is practically impossible to design, due to its infinite impulse response. Consequently, the spectral shape of $\check{S}_{non-ofdm}(\omega)$ is modified slightly. The *root raised-cosine* filter is a widely used filter to satisfy both spectral limitations and Inter-Symbol-Interference (ISI).

OFDM signal model

Usually, the channel exhibits different distortions for different frequency bands. OFDM divides the in-band spectrum into N_u sub-channels each having a sub-carrier with a narrow bandwidth signal f_b/N_u. Each sub-carrier has a fixed symbol period $N_u \cdot T_b$ but a variable modulation scheme M_i-QAM for the i-th sub-channel. The modulation rate M_i

can be varied according to the sub-channel quality. If a certain sub-channel has a low SNR, then the corresponding modulation rate M_i can be reduced to avoid increasing the bit error rate, and vice-versa. OFDM systems are particularly advantageous in scenarios when the communication channel is highly dynamic and frequency selective. A predetermined pilot signal is regularly transmitted at certain sub-carriers and fixed time instants. The receiver uses the received signal at the pilot locations to estimate the impulse response of the channel, and accordingly, try to accurately equalize the distorted received signal.

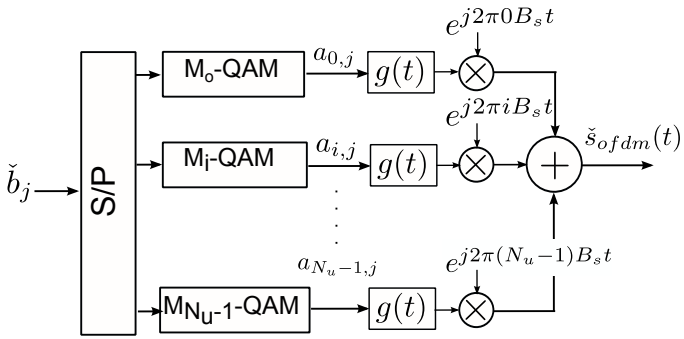

Figure 3.1: Block diagram of an OFDM transmitter

Figure 3.1 shows a conceptual model of an OFDM transmitter. The bit stream is interleaved to N_u sub-channels. Each sub-channel has a M_i-QAM modulator. Each modulator generates a complex baseband symbol $a_{i,j}$ which corresponds to the i-th sub-channel at the j-th OFDM frame. The period of each frame is fixed $T_{frame} = N_u \cdot T_b$. The output of all channels are summed up and then filtered using $g(t)$ to yield the signal $\check{s}_{ofdm}(t)$ which can be expressed as

$$\check{s}_{ofdm}(t) = \sum_{j=-\infty}^{\infty} \sum_{i=-N_u/2}^{N_u/2-1} a_{i,j} e^{j2\pi i B_s t} g(t - jT_b) \; . \tag{3.4}$$

where $B_s = f_b/N_u$ is the spacing between two neighbouring sub-channels in Hz. The inner summation in equation (3.4) denotes the aggregation of all sub-channels during the frame period T_{frame}, whereas the outer summation denotes the time propagation over all frames.

Abstractly speaking, OFDM systems can be regarded as an aggregation of closely packed non-OFDM systems. This summation has a key statistical consequence that will be exploited in the coming sections.

The baseband complex signals $\check{s}_{non-ofdm}(t)$ and $\check{s}_{ofdm}(t)$ are modulated to a carrier angular frequency ω_c. Since we can transmit only real signals (electromagnetic waves), the real part of the modulated signal is extracted and the transmitted signal whether for OFDM or non-OFDM systems is represented as

$$\begin{aligned} s(t) = \Re(\check{s}(t)e^{j\omega_c t}) &= i(t)\cdot\cos(\omega_c t) - q(t)\cdot\sin(\omega_c t) \\ &= r(t)\cdot\cos(\omega_c t + \theta(t)) \\ &= r(t)\cdot m(t)\ . \end{aligned} \tag{3.5}$$

3.2.2. Spectral uncertainty

As mentioned before, the pulse shaping filter defines the spectrum of the Cartesian signals $i(t)$ and $q(t)$. Since $i(t)$ and $q(t)$ can be considered uncorrelated, the covariance spectrum of $\check{s}(t)$ can be simply defined as

$$C_{\check{s}\check{s}}(\omega) = C_{ii}(\omega) + C_{qq}(\omega)\ . \tag{3.6}$$

In most cases, we have the same pulse shaping filter $g(t)$ for $i(t)$ and $q(t)$. Therefore $C_{ii}(\omega) = C_{qq}(\omega)$. This implies $C_{\check{s}\check{s}}(\omega) = 2C_{ii}(\omega)$.

The polar representation of the same baseband complex signal can be written as

$$\begin{aligned} \check{s}(t) &= r(t)\cdot e^{j\theta(t)} \\ &= r(t)\cdot\check{m}(t)\ , \end{aligned} \tag{3.7}$$

where the real part of $m(t)$ is

$$\begin{aligned} m(t) &= \Re\{e^{j\theta(t)}\} \\ &= \cos(\theta(t))\ . \end{aligned} \tag{3.8}$$

The spectral and statistical properties of $r(t)$, $\theta(t)$ and $m(t)$ are of physical significance. However, the Cartesian-to-polar conversion is a non-linear function in contrast to the addition in $\check{s}(t) = i(t) + jq(t)$. This implies that knowing only the spectra of $i(t)$ and $q(t)$ is not sufficient to derive the spectra of $r(t)$, $\theta(t)$ and $m(t)$. Consequently, we need to resort to a statistical method to derive the theoretical properties. Since the spectrum of a stochastic signal is a second order moment in the frequency domain, we will need the statistical distribution of $\check{s}(t)$ in order to derive the spectra of $r(t)$, $\theta(t)$ and $m(t)$.

In this chapter, the derivation of the spectral and statistical properties will not be covered in detail. Only an overview of the approach made in [Ibrahim and Yang, 2014b] will be summarized, as well as some results will be presented in the coming sections.

3.2.3. Approach

The approach for deriving the spectrum of $r(t)$, $\theta(t)$ and $m(t)$ is summarized in figure 3.2. The target of the derivation is to find $C_{rr}(\omega)$, $C_{\theta\theta}(\omega)$, and $C_{\dot{m}\dot{m}}(\omega)$. As shown, moving from the covariance spectra of the Cartesian signals $i(t)$ and $q(t)$ to the covariance spectra of the polar signals is not possible due to the non-linear Cartesian to polar conversion.

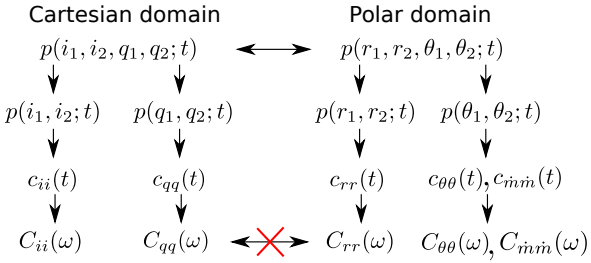

Figure 3.2: Path to derive the spectra of $C_{rr}(\omega)$, $C_{\theta\theta}(\omega)$, and $C_{\dot{m}\dot{m}}(\omega)$

The derivation starts with the joint PDF for 2 signal instants $\check{s}_1$ and $\check{s}_2$ denoted as $p(i_1, i_2, q_1, q_2; t)$. The corresponding joint PDF for the polar signals $p(r_1, r_2, \theta_1, \theta_2; t)$ is found by transform of variables. The bivariate distribution $p(r_1, r_2)$ is then derived by integrating $p(r_1, r_2, \theta_1, \theta_2; t)$ over θ_1 and θ_2, the same is done for $p(\theta_1, \theta_2)$. The auto-covariance function is then calculated by finding the correlation function as follows

$$\begin{aligned} C_{rr}(t) = Cov(r_1, r_2) &= \left(\int_0^{\infty} \int_0^{\infty} r_1 \cdot r_2 \cdot p(r_1, r_2) \mathrm{d}r_1 \mathrm{d}r_2 \right) \\ &\quad - E(r_1) E(r_2) \ , \\ C_{\theta\theta}(t) = Cov(\theta_1, \theta_2) &= \int_{-\pi}^{\pi} \int_{-\pi}^{\pi} \theta_1 \cdot \theta_2 \cdot p(\theta_1, \theta_2) \mathrm{d}\theta_1 \mathrm{d}\theta_2 \ , \end{aligned} \tag{3.9}$$

where $E(\cdot)$ is the expectation operation. Finally, the auto-covariance spectrum is found by finding the Fourier transform of the auto-covariance function.

In order to reach the spectra of the polar signals, we need to take into account two main inputs to the path depicted in figure 3.2:

- The Cartesian auto-covariance function $c_{ii}(t)$. This is simply determined by the pulse shaping filter.
- An important assumption made for this derivation is that the Cartesian signal $\check{s}(t)$ is a circular complex Gaussian signal. This implies that $r(t)$ is Rayleigh dis-

tributed and $\theta(t)$ has a uniform distribution. Later, the validity of this assumption for different communication protocols will be investigated.

3.3. Results

In this section, a comparison of the theoretical investigations made in [Ibrahim and Yang, 2014b] to selected communication protocols will be presented. In [Ibrahim and Yang, 2014b], the authors presented an analytical study of the spectral and statistical properties of the polar signals. Those properties were derived based on the following assumptions:

- The Cartesian signals are Gaussian distributed and mutually uncorrelated. This results in an equal distribution of the phase signal and a Rayleigh distribution of the radius signal.
- The Cartesian signals are filtered using a pulse shaping filter which usually has a rectangular spectrum.

Based on the aforementioned properties, the spectrum and distribution of the polar signals can be derived. In the following part, we consider 3 communication protocols to verify the validity of the analysis made in [Ibrahim and Yang, 2014b].

EDGE

Figure 3.3 compares the theoretical and actual spectral and statistical properties presented in [Ibrahim and Yang, 2014b] with 1000 simulated EDGE symbols. In the first column, the PDFs of $i(t)$, $r(t)$, $\theta(t)$, and $\cos(\theta(t))$ are shown. As shown, the PDF of $i(t)$ is not perfectly Gaussian. Consequently, $r(t)$ does not have an ideal Rayleigh distribution. However, if we observe the covariance function, we see that the theory matches the simulation to a great extent. The spectrum of $i(t)$ agrees with the theory. The simulated spectrum of $r(t)$ is similar to the theory except for spikes at factors of the symbol rate. This can be intuitively explained based on the fact that all EDGE symbols have equal radius, which is revisited every symbol time. This periodicity contributes to the spikes at factors of the symbol rate. The spectrum of $\theta(t)$ agrees with the theory, while the actual spectrum of $\cos(\theta(t))$ does not agree with the theory at high frequencies.

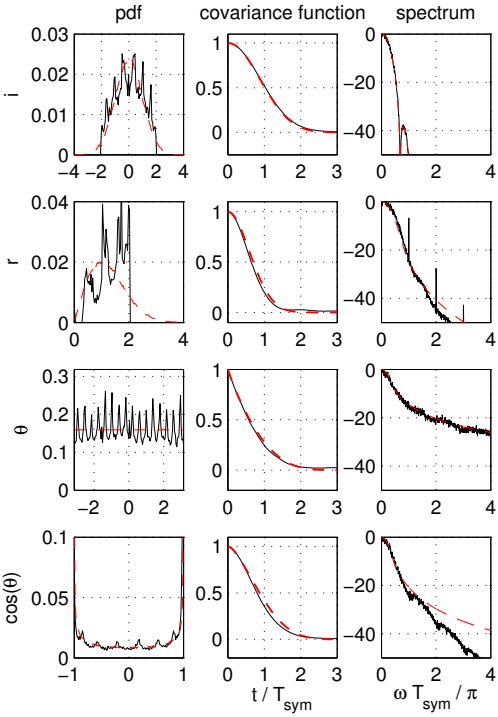

Figure 3.3: Comparison between theory and simulation in EDGE

LTE

LTE is the 4G communication standard which can support up to 20 MHz bandwidth. This corresponds to up to 300 Mbps for downlink and 75 Mbps for uplink. As an OFDM system, several sub-channels are aggregated together to generate the baseband signal as shown in figure 3.1. The aggregation of many independent channels implies that the Cartesian signal $\check{s}(t)$ has a Gaussian PDF due to the central limit theorem. Figure 3.4 confirms the Gaussian PDF of $i(t)$. Since the Gaussian PDF condition is fulfilled, then the analysis made in [Ibrahim and Yang, 2014b] applies better than the EDGE case. We can see that both PDF and spectrum for all signals agree perfectly to theory.

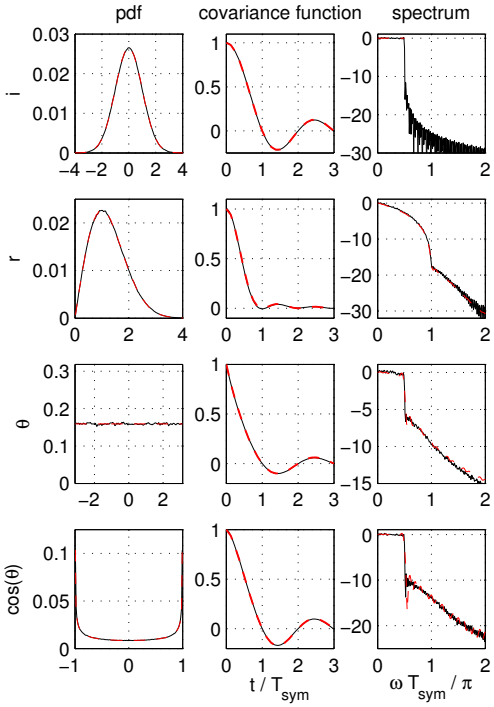

Figure 3.4: Comparison between theory and simulation in LTE

LTE-Advanced

LTE has a later release called LTE-Advanced (LTE-A). Data rates up to 1 Gbps are achievable in LTE-A. Such high rates are attainable due to the better management of the available spectrum as well as extra spectrum allocation from other communication protocols.

In LTE, the sub-carriers are allocated to the user in consecutive blocks. This means that all sub-carriers are adjacent and centered around the carrier frequency. In LTE-A, the user can be allocated sub-carriers from different bands, which means that the sub-carriers are not allocated in blocks but are rather distributed.

The validity of the theory compared to actual LTE-A simulations are displayed in figure 3.5. As shown, the theoretical spectrum of $i(t)$ has no active sub-carriers around zero frequency, but has allocated sub-carriers in positive and negative frequencies. The simulated and the theoretical PDFs still agree due to the Gaussian PDF of $i(t)$ which is preserved in LTE-A. Similarly, the spectra of $r(t)$, $\theta(t)$, and $\cos(\theta(t))$ still agree with the theoretical spectra.

The results shown in figures 3.3, 3.4, and 3.5 imply that the Gaussian distribution is the fundamental requirement for matching actual simulations with the theory. Since modern communication standards tend to have large bandwidths, this implies that the Cartesian signals will always have a near Gaussian distribution, which makes the theoretical analysis made in [Ibrahim and Yang, 2014b] valid.

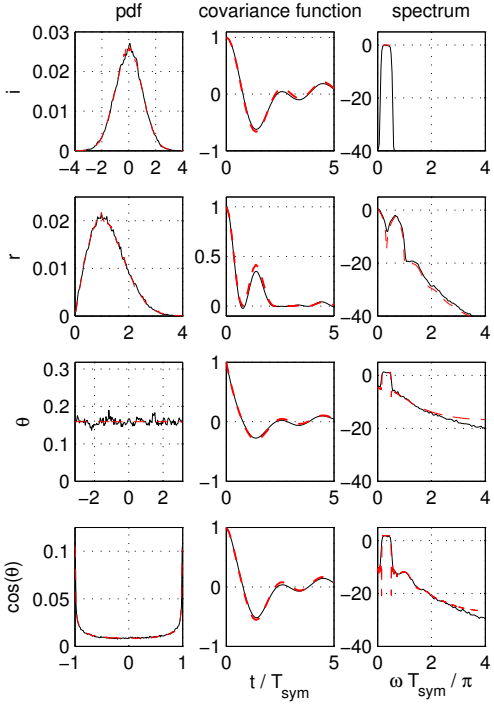

Figure 3.5: Comparison between theory and simulation in LTE-A

3.4. Quantization of polar signals

As mentioned in chapter 2, polar transmitters occupy smaller physical space due to the digitization of the transmitter components. Digitizing the polar transmitter comes at the expense of attaining a considerable amount of quantization noise. Generally speaking, quantization noise tends to have a white spectrum. When the spectral level of quantization noise exceeds a certain level, the spectral mask of the transmitted signal might be violated. Usually, the quantization noise is filtered in order to have a better SNR at certain frequencies. Therefore, there is a need to analyze the quantization noise in polar signals in order to understand its exact influence on the out-of-band noise. In this section, a general analysis of the quantization of polar signals in baseband is presented.

3.4.1. Spectrum

The quantization process can be modeled in several ways. In our case, we assume that the quantization noise power is low compared to the signal power. Based on that, we can assume that the quantization noise is an additive error signal. The quantization noise is assumed to have zero mean, equally distributed, and uncorrelated to the input signal [Widrow and Kollár, 2008]. Based on those assumptions, we model the polar-quantized complex signal as

$$\check{s}[n] = r[n]e^{(\jmath\theta[n])} \tag{3.10}$$

$$\check{s}_q[n] = (r[n] + e_r[n])e^{(\jmath\theta[n]+e_\theta[n])} \ . \tag{3.11}$$

Ultimately, we need to model the quantized signal in the form of

$$\check{s}_q[n] = Q(\check{s}[n]) = \check{s}[n] + e_s[n] \ , \quad \text{with} \quad \check{s}[n] = r[n]e^{\jmath\theta[n]} \tag{3.12}$$

where the additive term $e_s[n]$ contains the polar quantization error. This can be done by finding the total derivative to estimate the error such that

$$\begin{aligned} e_s[n] &= \frac{d\check{s}}{dr}e_r[n] + \frac{d\check{s}}{d\theta}e_\theta[n] \\ &= e^{\jmath\theta[n]}e_r[n] + \jmath \cdot \check{s}[n]e_\theta[n] \\ &= \check{m}[n]e_r[n] + \jmath \cdot \check{s}[n]e_\theta[n] \ . \end{aligned} \tag{3.13}$$

From Appendix A, it can be shown that the power spectral density of $e_s[n]$ can be represented as

$$R_{e_s e_s}(\omega) = \sigma^2_{e_r} + \sigma^2_{\check{s}}\sigma^2_{e_\theta} \ , \tag{3.14}$$

where $\sigma^2_{e_r}$, $\sigma^2_{\check{s}}$, and $\sigma^2_{e_\theta}$ correspond to the variance of e_r, $\check{s}$, and e_θ, respectively. Equation (3.14) implies that the quantization of the polar signals r and θ results in a flat spectrum as shown in figure 3.6. It is worth noting that according to equation (3.14), in case $\sigma^2_{\check{s}} > 1$, the phase quantization e_θ is more critical than radius quantization e_r as its variance is scaled with the signal power $\sigma^2_{\check{s}}$. This is intuitive, since the phase signal $\theta[n]$ is always confined within a range of 2π unlike the radius which might have a larger range.

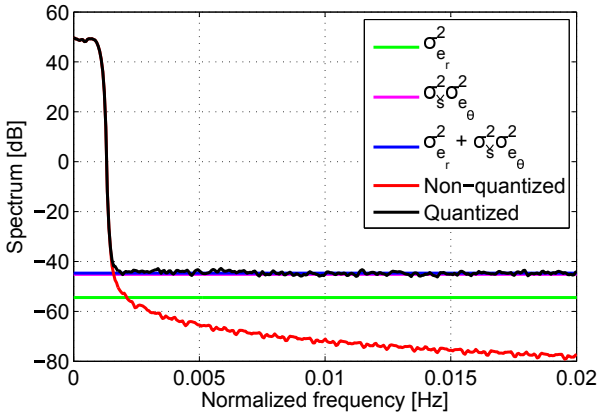

Figure 3.6: Verification of the out-of-band noise for polar quantization

3.4.2. Filtering of quantization noise

After analyzing the quantization noise of polar signals, we need to investigate the effect of filtering the quantization noise on the spectrum of the baseband complex signal $\check{s}_q[n]$. Assume that $\tilde{H}_r(\omega)$ and $\tilde{H}_\theta(\omega)$ are the filters which are applied to the quantization error signals e_r and e_θ, respectively. The filtered quantization noise can be denoted as $\tilde{e}_r[n]$ and $\tilde{e}_\theta[n]$. Therefore, the noise-shaped complex signal can be represented as

$$\tilde{s}_q[n] = \check{s}[n] + e^{\jmath\theta[n]}\tilde{e}_r[n] + \jmath\check{s}[n]\tilde{e}_\theta[n] \,, \tag{3.15}$$

while the covariance spectrum of $\tilde{s}_q[n]$ can be represented as

$$\begin{aligned} C_{\tilde{s}_q\tilde{s}_q}(\omega) &= C_{\check{s}\check{s}}(\omega) + C_{\check{m}\check{m}}(\omega) * C_{\tilde{e}_r\tilde{e}_r}(\omega) + C_{\check{s}\check{s}}(\omega) * C_{\tilde{e}_\theta\tilde{e}_\theta}(\omega) \\ &= C_{\check{s}\check{s}}(\omega) + C_{\check{m}\check{m}}(\omega) * \left(|\tilde{H}_r(\omega)|^2 C_{e_re_r}(\omega)\right) + C_{\check{s}\check{s}}(\omega) * \left(|\tilde{H}_\theta(\omega)|^2 C_{e_\theta e_\theta}(\omega)\right) \,. \end{aligned} \tag{3.16}$$

Since the spectrum of the quantization noise is assumed to be white and equal to the quantization noise variance, we get

$$C_{e_\theta e_\theta}(\omega) = \sigma^2_{e_\theta} . \tag{3.17}$$

$$C_{e_r e_r}(\omega) = \sigma^2_{e_r} . \tag{3.18}$$

Equation (3.16) becomes

$$C_{\check{s}_q \check{s}_q}(\omega) = C_{\check{s}\check{s}}(\omega) + \sigma^2_{e_r} C_{\check{m}\check{m}}(\omega) * |\tilde{H}_r(\omega)|^2 + \sigma^2_{e_\theta} C_{\check{s}\check{s}}(\omega) * |\tilde{H}_\theta(\omega)|^2 . \tag{3.19}$$

From equation (3.14) we know that in case that $\sigma^2_{\check{s}} > 1$, then the phase quantization error $e_\theta[n]$ contributes to a significant part of the overall noise $e_s[n]$. This implies that the filter $\tilde{H}_\theta(\omega)$ has more influence on $e_s[n]$ than $\tilde{H}_r(\omega)$. Assume that $C_{\check{s}\check{s}}(\omega)$ is a rectangular spectrum with a cut-off frequency ω_{co}, while $\tilde{H}_\theta(\omega)$ is a notch filter with a notch at $\omega_o > \omega_{co}$ and notch width B_N. From equation (3.19) we see that the spectrum $C_{\check{s}\check{s}}(\omega)$ is convolved with $|\tilde{H}_\theta(\omega)|^2$ and the output is scaled by $\sigma^2_{e_\theta}$. The effect of convolving the rectangular spectrum $C_{\check{s}\check{s}}(\omega)$ with the notch frequency response of $\tilde{H}_\theta(\omega)$ can be explained using figure 3.7.

As shown in figure 3.7, the notch in the spectrum $C_{\check{s}\check{s}}(\omega) * |\tilde{H}_\theta(\omega)|^2$ is not as deep as the notch in $\tilde{H}_\theta(\omega)$. The notch depth is $(B_N/\omega_{co})\sigma^2_{\check{s}}$. The notch width is $2\omega_{co} - B_N$ with a transition width of B_N. This implies that for a wide band signal ($\omega_{co}/(2\pi f_s)$ is large), the overall notch is broad and not deep and vice-versa. This means that just using a traditional notch filter for $\tilde{H}_\theta(\omega)$ will not result in a notch in the transmitted signal which has similar shape as the notch in $\tilde{H}_\theta(\omega)$ as in the Cartesian case. Two simulations have been done for narrow and wide band signals. The results are shown in figures 3.8 and 3.9.

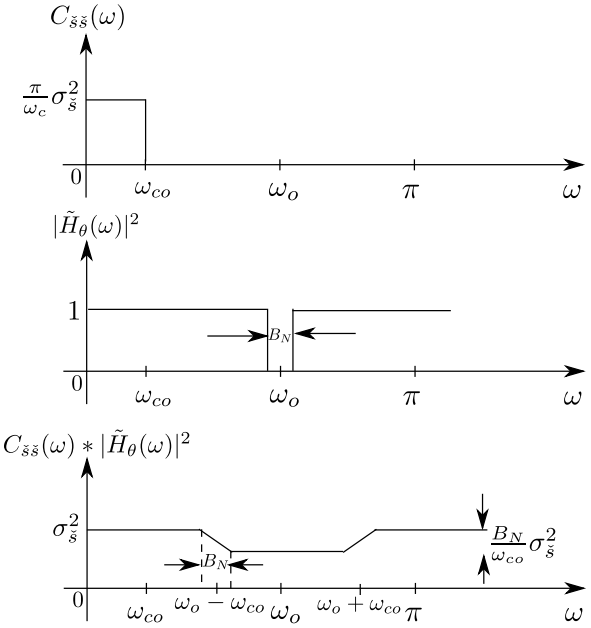

Figure 3.7: Effect of filtering phase quantization error e_θ

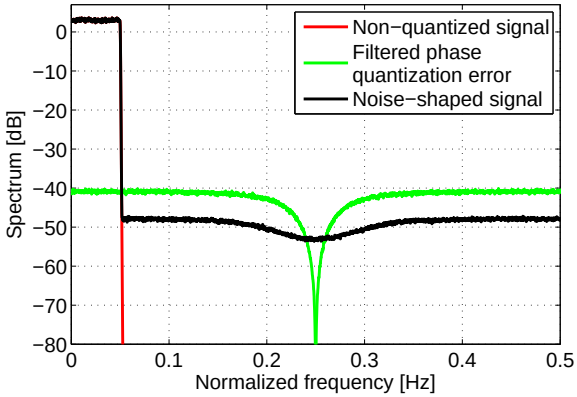

Figure 3.8: Effect of filtering phase quantization error e_θ for signal with normalized bandwidth = 0.1

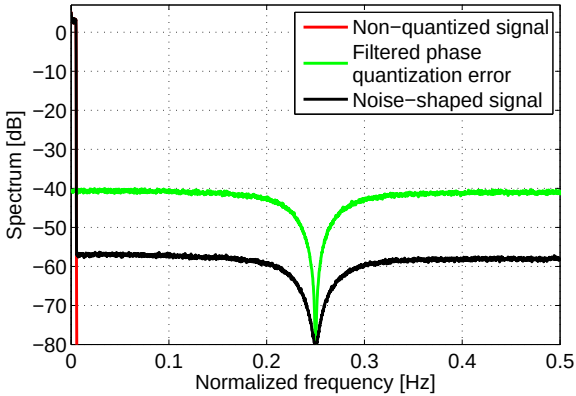

Figure 3.9: Effect of filtering phase quantization error e_θ for signal with normalized bandwidth = 0.01

4. Phase processing

In many communication standards, the baseband signal modulates both the amplitude and phase of the carrier wave. If there is no amplitude modulation, then the transmitted signal has a fixed amplitude and a varying phase. In IQ transmitters, Amplitude Modulation (AM) and Phase Modulation (PM) are coupled in the I and Q branches. On the other hand, polar transmitters isolate AM and PM separately. AM is done in the radius branch and PM is done in the phase branch.

In this chapter, we will be focusing on the phase branch. It will be explained how to generate the ideal phase modulated signal $m(t) = \cos(\omega_c t + \theta(t))$ from the baseband phase signal $\theta(t)$. The analysis starts with the digital phase $\theta[n]$ generated by the CORDIC and ends with the phase modulated signal $m(t)$. Unlike the radius, the phase signal needs to pass through several processing blocks in order to generate $m(t)$. Distortions in the phase branch tend to be more critical than the radius branch.

This chapter can be divided into four major sections. In the first section, the phase signal in baseband and passband is analyzed. In the second section, we explain how to extract the instantaneous period from the passband phase signal. In the third section, the DTC and DCO which convert the instantaneous period/frequency into a real phase modulated sinusoidal signal will be analyzed. Finally, we analyze the effect of quantizing the instantaneous frequency/period on the spectrum of the transmitted signal.

4.1. Baseband and passband phase signals

In this section, we explain the influence of the baseband phase signal $\theta[n]$ and the passband phase signal $\breve{\theta}[n]$ on the track of the complex baseband $\check{s}[n]$ and passband $\breve{s}[n]$ signals.

4.1.1. Complex track

In chapter 3, the statistical and spectral properties of the phase signal in baseband were analyzed. However, since we modulate the baseband signal onto a carrier frequency,

the phase signal changes when modulating from baseband to passband. The theoretical passband signal is

$$\breve{s}[n] \quad = \quad \check{s}[n]\, \mathrm{e}^{\jmath(\omega_c/f_s)n} \ , \tag{4.1}$$

while the phase of $\check{s}[n]$ is

$$\breve{\theta}[n] \quad = \mathrm{mod}\ (\theta[n] + \frac{\omega_c}{f_s} n, 2\pi) - \pi \ . \tag{4.2}$$

It is worth noting that up-conversion in the polar transmitter architecture is done in a much easier way when compared to traditional IQ transmitters. In order to modulate a baseband signal in IQ transmitters, a pair of analog oscillators and multipliers are needed. However, in order to modulate a baseband signal in polar transmitters, a linear phase component $(\omega_c/f_s)n$ is simply added to the baseband phase $\theta[n]$ which is generated by the CORDIC. The output of this addition is wrapped to $[-\pi, \pi)$ range using a modulo operation. This process is shown in figure 4.1.

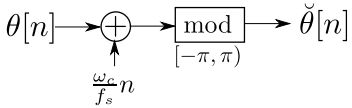

Figure 4.1: Modulation of baseband phase $\theta[n]$ to passband phase $\breve{\theta}[n]$

In order to visualize the track taken by $\check{s}[n]$ and $\breve{s}[n]$ in the complex plane, figure 4.2 shows the difference between baseband and passband complex tracks of the signals $\check{s}[n]$ and $\breve{s}[n]$, respectively.

In Figure 4.2a, the complex track of a signal with 16-QAM symbols a_i is shown, which are filtered using a raised cosine pulse shaping filter. The left plot shows the baseband track of the complex signal $\check{s}[n]$ for a short period of time. As shown, the track is smooth due to filtering using a digital raised cosine filter which limits its spectrum. However, the track of the modulated passband signal $\breve{s}[n]$ is different as shown in the middle figure. On the right figure, we use the z-axis to depict the time propagation. As shown, the 3D track is similar to a *helical* track with variable radius. The reason for this circular motion is the linear phase of the carrier signal $(\omega_c/f_s)n$, which is a complex signal with fixed amplitude and continuously rotating phase.

To further elaborate this principle, the complex track for a single fixed complex symbol $\check{s}[n] = 1 + \jmath$ is shown in figure 4.2b . In this case the passband phase is a strictly linear function defined as

$$\breve{\theta}[n] \quad = \quad \mathrm{mod}\ (\frac{\pi}{4} + \frac{\omega_c}{f_s} n) - \pi \ . \tag{4.3}$$

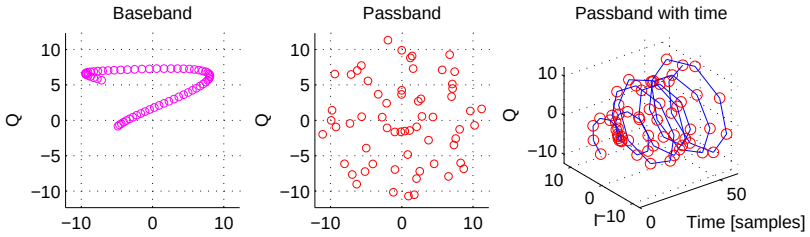

(a) Baseband and passband complex tracks for a random complex pulse shaped signal

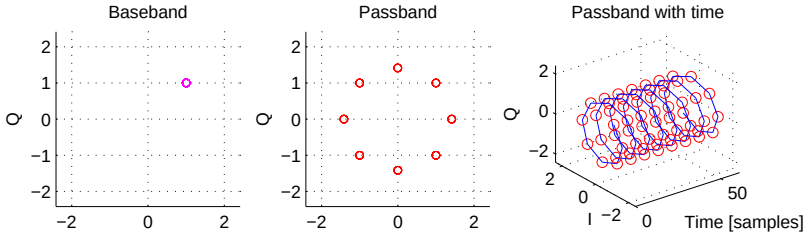

(b) Baseband and passband complex tracks for a fixed complex signal

Figure 4.2: Complex tracks of baseband and passband signals

As shown on the right plot in figure 4.2b, the track is moving in an exact helical track due to the linear phase of the carrier and the constant amplitude of the baseband symbol.

4.2. Instantaneous period

The phase modulated signal $m(t) = \cos(\omega_c t + \theta(t))$ can be approximately regarded as a cascade of sinusoidal waves with each wave having a variable period. The period of each wave is defined as the instantaneous period $\upsilon[m]$, where m corresponds to the m-th sinusoidal wave. The varying baseband phase $\theta[n]$ changes the instantaneous period $\upsilon[m]$. If the phase of the baseband signal is kept constant, then the instantaneous period becomes constant and equal to $\upsilon[m] = 1/f_c$ seconds.

Figure 4.3 shows 3 examples of simple baseband test signals which can easily explain the relationship between $\theta[n]$ and $\upsilon[m]$. In the first row, the baseband complex signal has a fixed phase of $\pi/4$. In the second row, the baseband phase signal is increasing linearly. In the third row, the baseband phase is increasing quadratically.

For each case, the phase modulated signal $m(t)$ is plotted in the middle column. At the right column, the instantaneous period signal $\upsilon[m]$ is plotted. As shown in the case of

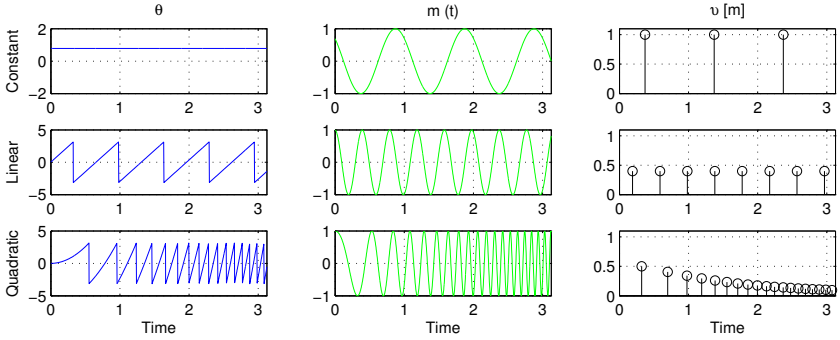

Figure 4.3: Instantaneous period for different baseband phase signals

constant phase in the upper row, the instantaneous period of $m(t)$ is fixed and is equal to the period of the carrier signal $1/f_c$, which is normalized to 1. For the linear phase case in the middle row, $m(t)$ has a fixed instantaneous period which is shorter than $1/f_c$ seconds since $\theta[n]$ is increasing at a constant rate. Finally, the quadratically increasing phase in the last row generates the signal $m(t)$ which has decreasing instantaneous periods.

Note that the instantaneous period has non-equidistant samples regarding the time index m. The value of the current instantaneous period sample $\upsilon[m_o]$ is equal to the time till the next instantaneous period sample $\upsilon[m_o + 1]$ arrives.

The instantaneous period is a critical signal in the polar transmitter. The accuracy of calculating $\upsilon[m]$ has a significant impact on the reduction of the out-of-band noise of the transmitted signal. Since we are considering mobile communication operating in the Giga-hertz range, the instantaneous period of the carrier signal is in the nano-second range. The changes of baseband phase signals cause very fine changes in the instantaneous period (in the femto-second range). The main challenge of the phase branch is to compute those fine changes in time using digital circuits as well as to generate a signal which is as close as possible to the theoretical signal $m(t) = \cos(\omega_c t + \theta(t))$.

Instantaneous period computation

In this section, the extraction of the instantaneous period from the passband phase signal $\breve{\theta}[n]$ is described. The method proposed to calculate the instantaneous period in this thesis is based on processing the passband phase signal $\breve{\theta}[n]$. In order to illustrate a

typical time-domain behavior of $\breve{\theta}[n]$, consider figure 4.4.

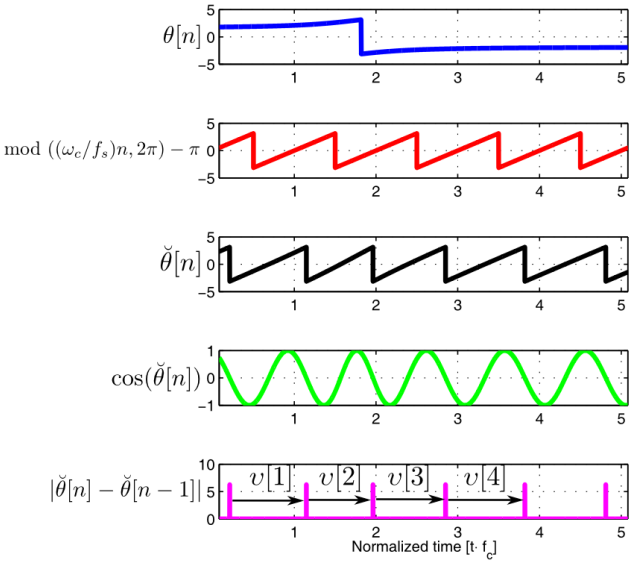

Figure 4.4: Sample of the baseband phase $\theta[n]$, the carrier phase $(\omega_c/f_s)n$, the passband phase $\breve{\theta}[n]$, the phase modulated signal $m[n] = \cos(\breve{\theta}[n])$ and also the values of the first derivative of the pass band phase $|\breve{\theta}[n] - \breve{\theta}[n-1]|$

Figure 4.4 shows three plots of a short sample of the phase signals. In this plot, the carrier frequency is $f_c = 0.5$GHz, the baseband signal has a bandwidth of $f_b = 20$MHz, and the sampling frequency is $f_s = 1$THz. The x-axis is normalized to the period of the carrier signal. The first row shows the baseband phase signal $\theta[n]$, the second row shows the wrapped carrier phase $\mod((\omega_c/f_c)n, 2\pi) - \pi$, the third plot shows the resultant passband phase $\breve{\theta}[n]$ according to equation (4.2), the fourth row is the phase modulated signal $m[n] = \cos(\breve{\theta}[n])$, and the fifth row shows the absolute value of the first derivative of the passband phase $\breve{\theta}'[n] = \breve{\theta}[n] - \breve{\theta}[n-1]$.

From the plot we see that the baseband phase changes relatively slowly compared to the carrier phase signal as the signal bandwidth is much lower than the carrier frequency $f_b \ll f_c$. Due to the varying baseband phase $\theta[n]$, the toggling instant of the passband phase $\breve{\theta}[n]$ from π to $-\pi$ is shifted in time. Accordingly, the instantaneous period changes.

The proposed way of calculating the instantaneous period is to calculate the absolute

value of the first derivative of the passband phase $|\breve{\theta}'[n]|$. This signal has spikes at the instants when the passband phase toggles from π to $-\pi$ as shown in figure 4.4. By measuring the time lag between the spikes in $|\breve{\theta}'[n]|$, we can compute the instantaneous period as the time between two consecutive spikes.

The instantaneous periods $\upsilon[m]$ are shown on the fifth row in figure 4.4. It is shown that $\upsilon[1] > \upsilon[2]$. This is caused due to the increasing phase $\theta[n]$ during the period of $\upsilon[2]$. However, during the period of $\upsilon[1]$, $\theta[n]$ remains more or less constant, hence the instantaneous period is equal to the carrier period $\upsilon[1] \approx 1$.

4.3. Phase modulation devices

This section is dedicated to discuss the concept of operation of the DTC and DCO, which are the phase modulation devices in the polar transmitter. Both devices can be used to generate the signal $m(t) = \cos(\omega_c t + \theta(t))$ using the input instantaneous period/frequency. However, in real polar transmitters, the DTC and DCO transmit approximations of $m(t)$. The effect of those approximations on the spectrum of the transmitted signal will be analyzed later.

4.3.1. Digital-to-Time Converter

The DTC is a fairly new concept of phase modulators. However, the *time-to-digital* (TDC) converter is used more often in various applications. The TDC is usually used to convert analog timing instants to digital output time which correspond to the time duration between two simultaneous events.

Previous work on DTC mainly targeted other applications than mobile communication such as interpolation [Al-Ahdab et al., 2010]. One work was reported using the DTC for giving digital delays in a polar transmitter [Yong-Chang et al., 2009]. However, not enough information was provided about the exact mechanism of the DTC.

The DTC can be formally defined as a device which takes instantaneous periods $\upsilon[m]$ as a digital input and outputs a cascade of continuous-time square waves $\bar{m}_o(t) = \text{sgn}(\cos(\omega_c t + \theta(t)))$. Each square wave has a period corresponding to the input instantaneous period $\upsilon[m]$. Figure 4.5 shows the principle of operation of the DTC. As shown, non-equidistant samples of $\upsilon[m]$ arrive at the DTC. The generated square waves have periods corresponding to $\upsilon[m]$. As shown, the time instant when the square wave changes its polarity happens at the time instants when the phase is multiples of π.

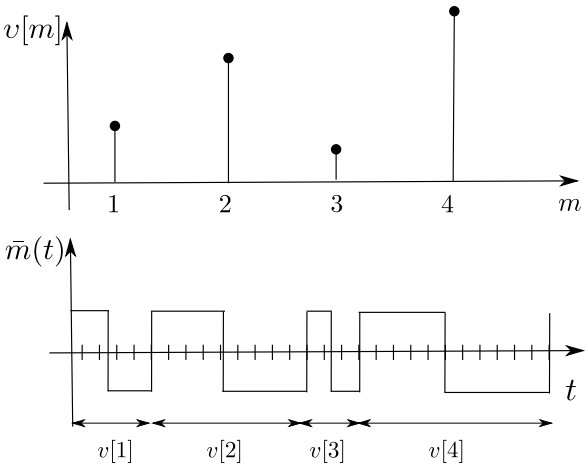

Figure 4.5: Operation of DTC

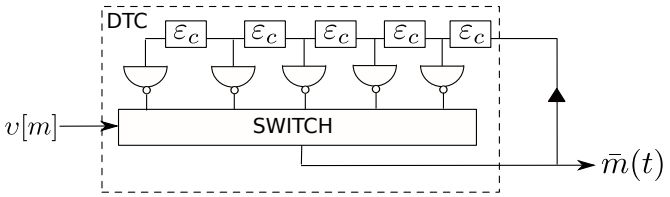

Figure 4.6: Internal components of DTC

Figure 4.6 gives an insight into the components of the DTC. As shown, the DTC is composed of an array of inverters with cascaded delay elements ε_c. The array is connected to a switch which is controlled by the input instantaneous period $\upsilon[m]$. The switch maps each possible value of $\upsilon[m]$ to one of the inverters' output. That means that each inverter corresponds to a certain time delay.

The left most inverter in figure 4.6 corresponds to the longest delay. The smaller ε_c is (shorter time), the finer the time grid and the more accurate the output $\bar{m}(t)$ becomes.

However, there are two main disadvantages for having a fine time grid. First, having smaller ε_c implies a larger number of delay elements in order to cover the complete range of possible instantaneous periods. More elements mean that the DTC will consume more energy for powering a large number of inverters. Second, we are limited to physical boundaries of the smallest possible achievable time delay which is in the range of femto seconds, under which we cannot physically design a delay element.

When comparing the output of the DTC denoted by $\bar{m}_o(t) = \text{sgn}(\cos(\omega_c t + \theta(t)))$ to the theoretical signal $m(t) = \cos(\omega_c t + \theta(t))$, we notice that there are several differences. The implications of those differences will be analyzed in section 4.3.3 in details.

Now, a mathematical expression for the output of the DTC in terms of the instantaneous period $\upsilon[j]$ will be presented. First we define the square function as

$$\text{sq}(t) \quad = \quad \begin{cases} 1 & \text{for } \; 0 \leq t < 0.5 \; , \\ -1 & \text{for } \; 0.5 \leq t < 1 \; , \\ 0 & \text{otherwise.} \end{cases} \tag{4.4}$$

A single square pulse with an instantaneous period $\upsilon[j_o]$ can be defined as

$$\text{sq}\left(\frac{t}{\upsilon[j_o]}\right) \; . \tag{4.5}$$

Assuming that this square wave starts at the time instant t_o, then the formula for the shifted square wave can be defined as

$$\text{sq}\left(\frac{t - t_o}{\upsilon[j_o]}\right) \; . \tag{4.6}$$

The starting time t_o of the square wave is determined by the sum of all previous instantaneous periods

$$t_o \quad = \quad \sum_{j=-\infty}^{j_o-1} \upsilon[j] \; . \tag{4.7}$$

Inserting equation (4.7) into equation (4.6), yields the formula

$$\mathrm{sq}\left(\frac{t-\sum_{j=-\infty}^{j_o-1}\upsilon[j]}{\upsilon[j_o]}\right). \tag{4.8}$$

Since all square waves do not overlap, therefore we can sum up all square waves for all values of the instantaneous period $\upsilon[j_o]$. The output of the DTC can thus be represented as

$$\bar{m}_o(t) \quad = \quad \sum_{j_o=-\infty}^{\infty}\mathrm{sq}\left(\frac{t-\sum_{j=-\infty}^{j_o-1}\upsilon[j]}{\upsilon[j_o]}\right). \tag{4.9}$$

4.3.2. Digitally controlled oscillator (DCO)

In most of the reported literature on polar transmitters, the DCO is used as the phase modulator [Groe, 2007][Staszewski et al., 2005a][Staszewski et al., 2005c][Bashir et al., 2011][Staszewski et al., 2008][Syllaios et al., 2008][Hyunseok and Songcheol, 2014][Staszewski et al., 2005b]. In this thesis, we give an overview of using the DCO just as a benchmark for comparison with the DTC.

The DCO is an analog oscillator which takes a digital instantaneous frequency $\eta[m]$ as an input and outputs cascaded continuous-time cosine waves $\mathring{m}(t)$ with frequencies corresponding to the input instantaneous frequency.

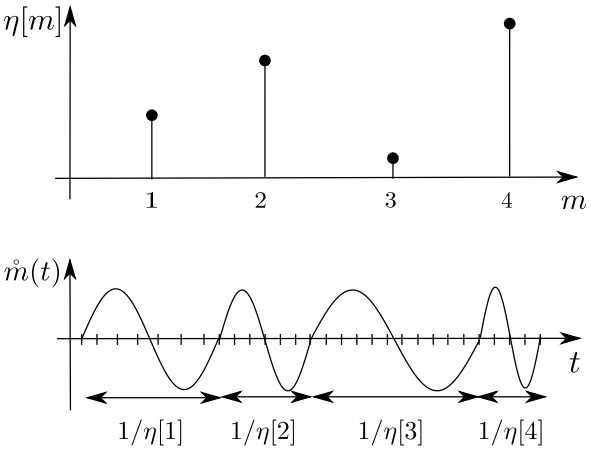

Figure 4.7: Operation of DCO

Figure 4.7 shows how the DCO operates. The upper plot shows an example of input instantaneous frequency $\eta[m]$. In the lower plot, the phase modulated signal $\mathring{m}(t)$ is shown. Note, that the DCO takes digital frequencies which lie on an equidistant frequency grid. This means that the corresponding time grid is non-equidistant due to the reciprocal relation between time and frequency.

There are two main differences between DCO and DTC. First, the DCO takes instantaneous frequencies as input rather than periods. Second, the DCO generates cosine waves rather than square waves. Although the output of the DCO is closer to the theoretical signal $m(t)$, the DTC is considered more promising than the DCO due to the following reasons:

- The DTC is composed of more digital and compact components such as delay elements and inverters, while the analog oscillator of the DCO occupies a large space and is not shrinkable.
- Computing the instantaneous period using the method described in 4.2 is simpler than the computation of instantaneous frequency. The reason is that measuring time in samples to compute the instantaneous period is easier than computing the reciprocal of time in order to obtain the instantaneous frequency.
- The DTC can be clocked using a square wave signal for all digital components in the mobile device. The output of the DTC can be computed from the clock signal itself. While in DCO, a dedicated oscillator is required.
- DTC is easier to extend for multi-modal communications. One single high frequency clock can be generated, and lower frequency clocks for different protocols can be derived from the high frequency clock.

4.3.3. PSD of the transmitted signal

In this section, the in-band PSD of the transmitted signal will be compared when using a square wave (DTC) and when using a cosine wave (DCO). Knowing the in-band PSD helps us compare the out-of-band noise to the in-band PSD to obtain a ratio similar to the SNR. For both DTC and DCO, an ideal DAC which converts $r[n]$ to $r(t)$ precisely is assumed.

Denoting the baseband signal as $\check{s}(t)$, the PSD of $\check{s}(t)$ can be represented as

$$R_{\check{s}\check{s}}(\omega) = \begin{cases} 2\sigma_s^2/f_b & \text{for } -\pi f_b < \omega < \pi f_b \,, \\ 0 & \text{otherwise.} \end{cases} \tag{4.10}$$

where $2\sigma_s^2$ is the power of the baseband signal. This PSD is a flat spectrum centered around $\omega = 0$. Modulating the baseband signal $\check{s}(t)$ to the carrier frequency ω_c is done theoretically by multiplying the baseband signal with a complex exponential so that the complex analytical signal can be represented as

$$\check{s}(t) \quad = \quad \check{s}(t) \cdot e^{j\omega_c t} \; . \tag{4.11}$$

Consequently, the PSD of $\check{s}(t)$ can be defined as

$$R_{\check{s}\check{s}}(\omega) \quad = \quad \begin{cases} 2\sigma_s^2/f_b & \text{for } \omega_c - \pi f_b < \omega < \omega_c + \pi f_b \; , \\ 0 & \text{otherwise.} \end{cases} \tag{4.12}$$

However, since we can only transmit real signals, we take the real part of the complex passband signal as $s(t) = \Re\{\check{s}(t)\}$, which is the actual passband signal. Thus, the total power of the baseband signal $2\sigma_s^2$ is split into two halves, for the real and the imaginary parts. The spectrum of the real part of the baseband signal has two identical images centered at the positive carrier frequency and the negative carrier frequency. The real passband signal has symmetric spectrum with equal spectral levels at $\omega = \omega_c$ and $\omega = -\omega_c$. Therefore the power spectral density of $s(t)$ can be denoted as

$$R_{ss}(\omega) \quad = \quad \begin{cases} \sigma_s^2/(2f_b) & \text{for} \quad \omega_c - \pi f_b < \omega < \omega + \pi f_b \; , \\ \sigma_s^2/(2f_b) & \text{for} \; -\omega_c - \pi f_b < \omega < -\omega + \pi f_b \; , \\ 0 & \text{otherwise.} \end{cases} \tag{4.13}$$

DCO

Since the DCO generates cosine waves, the power spectral density at ω_c when using a DCO should be similar to the theoretical power spectral level

$$R_{\hat{s}\hat{s}}(\omega) \quad \approx \quad R_{ss}(\omega) \; . \tag{4.14}$$

DTC

As mentioned earlier, the DTC generates square waves rather than cosine waves. By finding the Fourier expansion of the square waves in terms of its harmonics, we can relate the PSD of the DTC output to the theoretical PSD $R_{ss}(\omega)$. It is shown in Appendix B that the expansion of the phase modulated square waves, with $r(t)$ being the radius

signal, can be represented as

$$\begin{aligned}
\bar{s}_o(t) &= r(t) \cdot \mathrm{sgn}(\cos(\omega_c t + \theta(t))) \\
&= \left(\frac{4}{\pi}\right) \sum_{k=1}^{\infty} \frac{1}{2k-1} r(t) \cos\left((2k-1)(\omega_c t + \theta(t))\right) \\
&= \left(\frac{4}{\pi}\right) r(t) \cos(\omega_c t + \theta(t)) + \left(\frac{4}{\pi}\right) \sum_{k=2}^{\infty} \frac{1}{2k-1} r(t) \cos((2k-1)(\omega_c t + \theta(t))) \\
&= \left(\frac{4}{\pi}\right) s(t) + e_c(t) \ . \qquad (4.15)
\end{aligned}$$

where $e_c(t)$ is a term containing the harmonics at odd multiples of the carrier frequency. $e_c(t)$ will be revisited in chapter 5. At this point, we can state that $e_c(t)$ has no components at $\omega = \omega_c$. Consequently, we can conclude from equation (4.15) that the only component of $\bar{s}_o(t)$ at ω_c is $\left(\frac{4}{\pi}\right) s(t)$. This implies that the power spectral level at $\omega = \omega_c$ when using a DTC can be represented as

$$\begin{aligned}
R_{\bar{s}_o \bar{s}_o}(\omega_c) &= \left(\frac{4}{\pi}\right)^2 \cdot R_{ss}(\omega_c) \\
&= \left(\frac{4}{\pi}\right)^2 \cdot \frac{\sigma_s^2}{2 f_b} \ . \qquad (4.16)
\end{aligned}$$

Since $\left(\frac{4}{\pi}\right)^2 > 1$, this means that using a DTC increases the in-band power spectral level by a factor of $10 \log((4/\pi)^2) = 2.1$ dB compared to a DCO based polar transmitter.

4.4. Time Quantization

One of the main challenges of the polar transmitter is to abide to the spectral mask of the transmitted signal. Since the proposed polar transmitter architecture is mainly composed of digital circuits, there is a considerable amount of spurious noise caused by the quantization, which might violate the aforementioned spectrum mask. In section 3.4, the quantization of $r(t)$ and $\theta(t)$ was discussed from a theoretical point of view. Since the DTC does not generate the theoretical phase modulated signal $m(t)$, we have to analyze the quantization effect for the specific case of the DTC's square waves.

In this section, we analyze the quantization error spectrum when using DTC as a phase modulator. Quantization noise in the DTC arises from the fact that we have only discrete possible time delays as shown in figure 4.6. The smaller the delay time of the DTC elements ε_c is, the finer the time resolution and the closer the transmitted signal to the theoretical signal would be. Consequently, the out-of-band noise decreases. However, higher time resolution degrades the efficiency of the DTC due to the usage of many delay elements which consume more energy. The trade-off between out-of-band noise and time resolution is a critical design criterion in polar transmitters.

Simulations have shown that the main component of the out-of-band noise spectral level is caused by the time quantization of the DTC. This means that other distortions such as radius quantization and radius averaging are considered less significant than time quantization.

Up to now, the relationship between DTC time resolution and the out-of-band spectral level is based only on empirical measurements with no solid theoretical knowledge of the influencing parameters. In this section we present the work done in Ibrahim and Yang [2014a] to analyze the time quantization in polar transmitters. By deriving a theoretical formula for the spectral level of the noise caused by DTC time quantization, we can set a benchmark for comparing measurements from actual polar transmitters with their theoretical limit.

4.4.1. Error signal model

As a first step in the analysis, we need to examine the error signal which arises from the DTC time quantization. We will track the error signal in the time domain and try to formulate a stochastic model for its time domain behavior.

Theoretically, the DTC should generate $\cos(\omega_c t + \theta(t))$, but as we discussed in section

4.3.1, the DTC produces square waves. We define the theoretical output of the DTC as

$$\begin{aligned} \bar{m}_o(t) &= \text{sgn}\left(\sin(\omega_c t + \theta(t))\right) \\ &= \text{sgn}(\sin(\breve{\theta}(t))) \ . \end{aligned} \tag{4.17}$$

Here we define the phase modulated signal to be a sin rather than a cos. This is merely a 90 degrees phase shift which does not change any of the statistical or spectral properties of the transmitted signal. However, this assumption simplifies our explanation of the time quantization. $\bar{m}_o(t)$ is theoretical in the sense that the DTC can toggle at the exact time instant when the phase signal $\breve{\theta}(t)$ toggles from π to $-\pi$. In other words, $\bar{m}_o(t)$ has infinite time precision.

Figure 4.8 shows the time quantization signal $\bar{e}(t)$ which arises in the DTC. In figure 4.8a, we plot the passband phase signal $\breve{\theta}(t)$ defined in the range $-\pi \leq \breve{\theta}(t) < \pi$. We also plot the theoretical phase modulated signal $\bar{m}_o(t)$. As shown, $\bar{m}_o(t)$ toggles from A to $-A$ at the exact time instant when $\breve{\theta}(t)$ toggles from π to $-\pi$. However, since $\breve{\theta}(t)$ is sampled at discrete time instants with the sampling frequency of $f_s = 1/T_s$, the real signal $\bar{m}(t)$ is allowed to toggle only at discrete time instants of the time grid as shown in figure 4.8a. Moving the toggle slope earlier or later in time to the closest time grid results in the time quantization error $\bar{e}(t) = \bar{m}(t) - \bar{m}_o(t)$. This error is plotted in figure 4.8b.

From chapter 2 we know that the output of the DTC is multiplied by the output of the DAC. At the radius branch, the signal $r[n]$ is discrete in time and amplitude. This means that the output of the DAC $r(t)$ has quantization error as well. Taking the radius quantization error into account, then the transmitted signal can be represented as

$$\bar{s}_r(t) = [r(t) + e_r(t)][\bar{m}_o(t) + \bar{e}(t)] \tag{4.18}$$

$$= r(t)\bar{m}_o(t) + r(t)\bar{e}(t) + e_r(t)\bar{m}_o(t) + e_r(t)\bar{e}(t) \ , \tag{4.19}$$

where $r(t)$ is the analog radius signal and $e_r(t)$ is the quantization error signal. Note that the DTC error signal $\bar{e}(t)$ has an amplitude of $2A$, while the amplitude of the radius error $e_r(t)$ is much smaller than the radius signal $e_r(t) \ll r(t)$ and $e_r(t) \ll \bar{e}(t)$. Therefore, the third and fourth terms in equation (4.19) can be neglected. This assumption can be verified by previous work in literature [Ahmed, 2007] and simulations in section 5.3.2.

Based on this assumption, the transmitted signal $\bar{s}_r(t)$ can be approximated as

$$\bar{s}_r(t) = [r(t) + e_r(t)][\bar{m}_o(t) + \bar{e}(t)] \tag{4.20}$$

$$\approx r(t)\bar{m}_o(t) + r(t)\bar{e}(t) \tag{4.21}$$

$$\approx r(t)\bar{m}_o(t) + \bar{q}(t) \ . \tag{4.22}$$

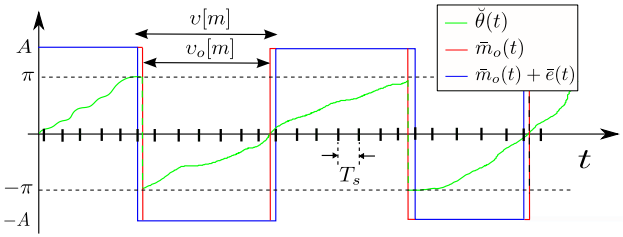

(a) DTC signal for exact instantaneous period $\upsilon_o[m]$ and quantized $\upsilon[m]$ vs passband phase $\breve{\theta}(t)$

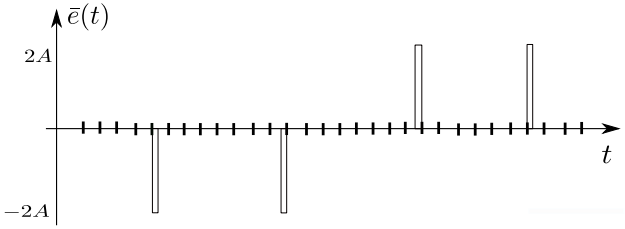

(b) DTC time quantization error $\bar{e}(t)$

Figure 4.8: Signal model of DTC quantization error

In this equation, the desired signal is $r(t)\bar{m}_o(t)$. Due to the DTC time quantization, an additive error signal $\bar{q}(t) = r(t)\bar{e}(t)$ is present as well. In the coming sections, the spectrum of $\bar{q}(t)$ will be investigated.

4.4.2. Spectrum of time quantization

In the previous section, it has been shown that the time quantization error signal $\bar{q}(t)$ is a product of two terms, $r(t)$ and $\bar{e}(t)$. In order to compute the spectrum of $\bar{q}(t)$, we need to analyze the spectrum of $r(t)$ and $\bar{e}(t)$.

Deriving the spectrum of $r(t)$ and $\bar{e}(t)$ using the Fourier transform is a challenging task since $r(t)$ and $\bar{e}(t)$ are random signals. Therefore, a statistical approach is applied, where the autocorrelation functions $r_{rr}(t)$ and $r_{\bar{e}\bar{e}}(t)$ of $r(t)$ and $\bar{e}(t)$ are sought. Then, the Fourier transform of the autocorrelation function $r_{\bar{q}\bar{q}}(t)$ is computed to get the PSD of $r(t)$.

Assuming that $r(t)$ is independent of $\bar{e}(t)$, the autocorrelation function of $\bar{q}(t)$ becomes

$$r_{\bar{q}\bar{q}}(t) \quad = \quad r_{rr}(t) r_{\bar{e}\bar{e}}(t) \ , \tag{4.23}$$

and the PSD of $\bar{q}(t)$ becomes

$$R_{\bar{q}\bar{q}}(\omega) \quad = \quad \frac{1}{2\pi} R_{rr}(\omega) * R_{\bar{e}\bar{e}}(\omega) \ . \tag{4.24}$$

Spectrum of DTC time quantization $\bar{e}(t)$

From figure 4.8b we see that $\bar{e}(t)$ is a superposition of rectangular pulses with short time durations. In this section we derive the PSD $R_{\bar{e}\bar{e}}(\omega)$ of $\bar{e}(t)$. Before proceeding with the derivation, we state some assumptions made about $\bar{e}(t)$ to simplify our spectrum derivation:

1. The amplitudes of different pulses are independent and identically distributed with equal probability of $\frac{1}{2}$ for $2A$ and $-2A$.
2. The random duration D of each pulse is uniformly distributed in $[0, \frac{T_s}{2}]$.
3. The sampling frequency f_s of $\breve{\theta}(t)$ is much larger than the carrier frequency f_c. As a result, all pulses in $\bar{e}(t)$ never overlap and $\bar{e}(t)$ has a zero mean.
4. Since each square wave has an average duration of $1/f_c$, and each square wave contributes to two error pulses, then on average there are $2f_c$ error pulses per second.

Starting with the derivation, we first compute the autocorrelation function of $\bar{e}(t)$

$$r_{\bar{e}\bar{e}}(t) \quad = \quad E(\bar{e}(t+\tau)\bar{e}(\tau)) \ . \tag{4.25}$$

Due to assumption number 1, the correlation between different pulses is zero. This means that the autocorrelation function is non-zero for only a short time lag of $|t|$ when a pulse overlaps with itself.

Considering a single rectangular pulse $\bar{e}_1(t)$ of $\bar{e}(t)$ conditioned on a fixed pulse duration D, the correlation function simplifies to the well-known triangular shape

$$\begin{aligned} r_{\bar{e}_1\bar{e}_1}(t) \quad &= \quad E(\bar{e}(t+\tau)\bar{e}(\tau)|D) = \int_{-\infty}^{\infty} \bar{e}(t+\tau)\bar{e}(\tau)\mathrm{d}\tau \\ &= \quad (2A)^2(D-|t|)\cdot \mathrm{rect}\left(\frac{t}{D}\right), \end{aligned} \tag{4.26}$$

where rect is defined as

$$\mathrm{rect}(t) \quad = \quad \begin{cases} 1 & \text{if} \quad |t| < 1 \\ 0 & \text{if} \quad |t| > 1 \end{cases} \tag{4.27}$$

Since D is a random variable, we need to average the correlation function over the distribution of D. Moreover, based on assumption 4, there are on average $2f_c$ error pulses per second due to the fact that there is one error pulse for each half a square wave. Therefore, the correlation function becomes

$$r_{\bar{e}\bar{e}}(t) \quad = \quad E_D(2f_c r_{\bar{e}_1\bar{e}_1}(t)) = E_D\left(2f_c(2A)^2(D-|t|)\mathrm{rect}\left(\frac{t}{D}\right)\right) \ , \tag{4.28}$$

where E_D is the expectation over D. The spectrum of $\bar{e}(t)$ is the Fourier transform of the correlation function, i.e. $R_{\bar{e}\bar{e}}(\omega) = \mathcal{F}\{r_{\bar{e}\bar{e}}(t)\}$. By changing the order of $\mathcal{F}\{\}$ and $E_D()$, we obtain

$$R_{\bar{e}\bar{e}}(\omega) \quad = \quad 8f_cA^2E_D[\mathcal{F}\{(D-|t|)\mathrm{rect}(\frac{t}{D})\}] \ . \tag{4.29}$$

It is well known from literature that the Fourier transform of a triangle is a sinc^2 function. Therefore we get

$$\begin{aligned} R_{\bar{e}\bar{e}}(\omega) \quad &= \quad 8f_cA^2E_D[D^2\mathrm{sinc}^2(\frac{\omega D}{2})] \\ &= \frac{16f_cA^2}{\omega^2}[1-E_D(\cos(\omega D)] \ , \end{aligned} \tag{4.30}$$

with $\mathrm{sinc}(z) = \sin(z)/z$. Since D has the probability density function of

$$p(D) \quad = \quad \begin{cases} \frac{2}{T_s} & 0 \le D \le \frac{T_s}{2} \ , \\ 0 & \text{otherwise.} \end{cases} \tag{4.31}$$

we get

$$\begin{aligned} R_{\bar{e}\bar{e}}(\omega) &= \frac{16 f_c A^2}{\omega^2}\left(1 - \int_0^{\frac{T_s}{2}} \cos(\omega D)\frac{2}{T_s}\mathrm{d}D\right) \\ &= 4A^2 T_s \frac{f_c}{f_s}\frac{1-\mathrm{sinc}(\omega T_s/2)}{(\frac{\omega T_s}{2})^2} \ . \end{aligned} \tag{4.32}$$

For large $|\omega|$, the spectrum decreases as $1/\omega^2$. In the neighborhood of $\omega = 0$, i.e. $|\omega| \ll 2\pi f_s$, we use the truncated Taylor series

$$\mathrm{sinc}(z) \approx 1 - \frac{z^2}{6} + \frac{z^4}{120} \tag{4.33}$$

to obtain

$$R_{\bar{e}\bar{e}}(\omega) \approx 4A^2 T_s \frac{f_c}{f_s}\left[\frac{1}{6} - \frac{1}{120}(\omega T_s/2)^2\right] \ . \tag{4.34}$$

The spectrum of the time quantization error $\bar{e}(t)$ looks like a parabola for small $|\omega|$ with

$$R_{\bar{e}\bar{e}}(0) = \frac{2}{3}A^2 T_s \frac{f_c}{f_s} \ . \tag{4.35}$$

In order to verify our theoretical result, a simulation has been done to compare the exact spectrum in equation (4.32) with the approximated function in equation (4.34).

Figure 4.9 shows a plot of the exact and approximated functions of $R_{\bar{e}\bar{e}}(\omega)$, as well as the value of the function at $\omega = 0$. Typical mobile communication parameters are set such as $f_c = 1\mathrm{GHz}$, $f_s = 1\mathrm{THz}$ and $A = 1$.

From figure 4.9, it can be concluded that the approximation is valid at the low frequencies. As the frequency increases, the deviation between the exact and approximated spectrum increases. However, we are mostly interested in the frequency range around the carrier frequency, which, in the case of mobile communications, is in the GHz range. Higher frequencies are attenuated by the antenna's low pass behavior. Hence, our approximation is valid for $f \approx f_c$.

Another observation that can be made from figure 4.9 is that the error spectrum decreases slowly as the frequency increases. We see that from $\omega = 0$ to $\omega = 5\mathrm{THz}$, the spectrum falls only around 2.5 dB. This means that the spectrum level is widely affected by the value of $R_{\bar{e}\bar{e}}(0)$ shown in equation (4.35), and is more or less flat in this frequency range.

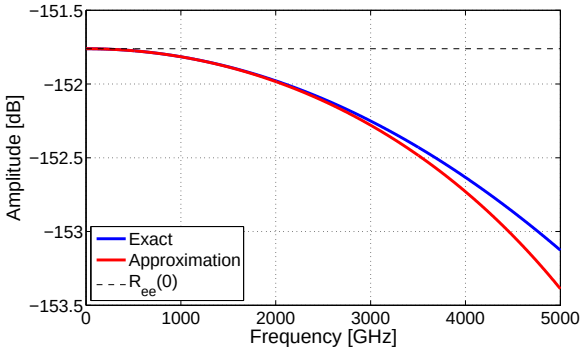

Figure 4.9: Exact and approximated spectrum of $\bar{e}(t)$ for $f_c = 1\text{GHz}$ and $f_s = 1\text{THz}$ and $A = 1$

Spectrum of time quantization spectrum

We now substitute $R_{\bar{e}\bar{e}}(\omega)$ into equation (4.24) to get the PSD $R_{\bar{q}\bar{q}}(\omega)$. This yields

$$R_{\bar{q}\bar{q}}(\omega) \quad = \quad \int_{-\infty}^{\infty} R_{rr}(\lambda) R_{\bar{e}\bar{e}}(\omega - \lambda) \frac{\mathrm{d}\lambda}{2\pi} \, . \tag{4.36}$$

We are mainly interested in the frequency range around the carrier frequency $\omega = \omega_c$. Therefore, the spectral level at the carrier frequency can be represented as

$$R_{\bar{q}\bar{q}}(\omega_c) \quad = \quad \int_{-\infty}^{\infty} R_{rr}(\lambda) R_{\bar{e}\bar{e}}(\omega_c - \lambda) \frac{\mathrm{d}\lambda}{2\pi} \, . \tag{4.37}$$

Note that $R_{\bar{e}\bar{e}}(\omega)$ is more or less flat around ω_o. As mentioned in [Ibrahim and Yang, 2014b], the bandwidth of the radius signal $r(t)$ is roughly $2f_b$, i.e. the bandwidth of the radius is much narrower than the carrier frequency $2f_b \ll \omega_c$. Thus we get

$$R_{\bar{q}\bar{q}}(\omega_c) \quad \approx \quad R_{\bar{e}\bar{e}}(\omega_c) \int_{-\infty}^{\infty} R_{rr}(\lambda) \frac{\mathrm{d}\lambda}{2\pi} \, . \tag{4.38}$$

The integral in equation (4.38) is simply the power of the baseband signal

$$\int_{-\infty}^{\infty} R_{\lambda}(\omega) \frac{\mathrm{d}\lambda}{2\pi} \quad = \quad E(r^2(t)) = \sigma_s^2 \, . \tag{4.39}$$

Combining equations (4.34), (4.38) and (4.39), the noise level at ω_c is

$$R_{\bar{q}\bar{q}}(\omega_c) \quad \approx \quad 4A^2 T_s \frac{f_c}{f_s} \left(\frac{1}{6} - \frac{1}{120} (\omega_c T_s / 2)^2 \right) \sigma_s^2 \, . \tag{4.40}$$

Carrier-to-noise ratio (CNR) for DTC

Now we know the PSD caused by the time quantization in the DTC. It would be useful to compare the in-band spectral level to the time quantization error level. We define the Carrier-to-noise ratio (CNR) to be

$$CNR = \frac{R_{\bar{s}\bar{s}}(\omega_c)}{R_{\bar{q}\bar{q}}(\omega_c)} . \tag{4.41}$$

By substituting equation (4.16) and (4.40) into equation (4.41) we get

$$CNR_{DTC}[dB] = 10\log_{10}\left(\frac{\frac{\sigma_s^2}{2f_b}A^2(\frac{4}{\pi})^2}{R_{\bar{q}\bar{q}}(\omega_c)}\right) . \tag{4.42}$$

Based on assumption 3 $f_c \ll f_s$ made in section 4.4.2 and knowing that $R_{\bar{e}\bar{e}}(\omega)$ falls slowly as shown in figure 4.9, we can assume that

$$\begin{aligned} R_{\bar{q}\bar{q}}(\omega_c) &\approx R_{\bar{e}\bar{e}}(0)\sigma_s^2 \\ &= \frac{2}{3}A^2T_s\frac{f_c}{f_s}\sigma_s^2 . \end{aligned} \tag{4.43}$$

Substituting equation (4.43) into equation (4.42), we get

$$CNR_{DTC}[dB] = 10\log_{10}\left(\frac{3}{4}\cdot\frac{(\frac{4}{\pi})^2}{\frac{f_b}{f_s}\frac{f_c}{f_s}}\right) . \tag{4.44}$$

Similarly, we can use equation (4.13) to obtain the CNR when using a DCO

$$CNR_{DCO}[dB] = 10\log_{10}\left(\frac{3}{4}\cdot\frac{1}{\frac{f_b}{f_s}\frac{f_c}{f_s}}\right) . \tag{4.45}$$

Equations (4.44) and (4.45) are the fundamental formulas which evaluate the CNR of a DTC/DCO-based polar transmitter. One can notice that the CNR depends on 3 parameters: baseband bandwidth f_b, sampling frequency f_s, and the carrier frequency f_c. As the bandwidth and the carrier frequency increase, the lower the CNR ratio becomes. The higher the sampling rate, the better the CNR ratio becomes. This is intuitive because increasing the sampling rate increases the time resolution and thus reduces the energy of the time quantization noise.

Note that doubling the bandwidth or the carrier frequency leads to a 3dB reduction in CNR. However, doubling the sampling frequency leads to a 6dB improvement in CNR. The bandwidth and carrier frequency are defined by the communication standard, and corresponding to those inputs, the hardware designer must choose a suitable sampling frequency f_s to abide to the spectral mask.

4.4.3. Verification

In this section, a verification of the out-of-band power spectral level around the carrier frequency is presented. In addition, we verify the influence of all parameters in equation (4.44). 1000 LTE uplink (SC-FDMA) symbols using 2048 FFT bins with a DTC-based polar transmitter are generated. we also verify that equation (4.44) is valid for a DCO-based polar transmitter.

Sampling frequency

First, passband signals with different sampling frequencies f_s are simulated. Figure 4.10 shows 3 transmitted signals with different sampling frequencies f_s=1THz, 5THz, and 10THz. For all transmitted signals, the bandwidth is fixed to f_b = 20MHz, which corresponds to 1334 occupied sub-carriers. The signals are all modulated at the same carrier frequency of f_c = 1GHz. The theoretical noise level based on equation (4.44) is also plotted. As shown, the simulated out-of-band noise fits perfectly into the theoretical noise level.

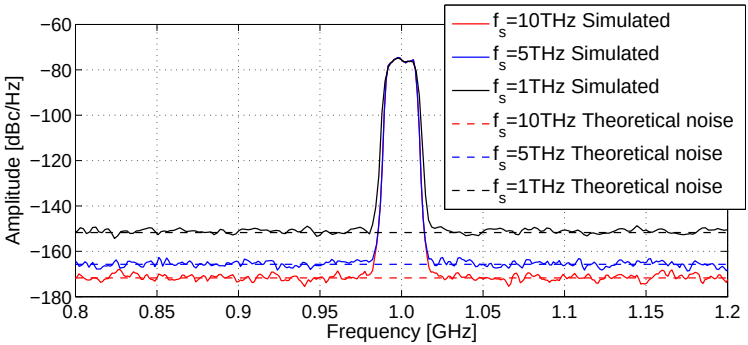

Figure 4.10: Transmitted spectrum from simulations and theoretical noise level for different sampling frequencies f_s with f_b = 20MHz and f_c = 1GHz

Bandwidth

Now, the effect of varying the baseband bandwidth f_b is investigated. The bandwidth of LTE signals is varied by changing the number of occupied sub-carriers. In this simulation, the bandwidths of f_b = 5MHz, 10MHz, and 20MHz which correspond to

334, 667, and 1334 occupied sub-carriers are used. The sampling frequency is fixed to f_s = 1THz, and the carrier frequency is f_c = 1GHz.

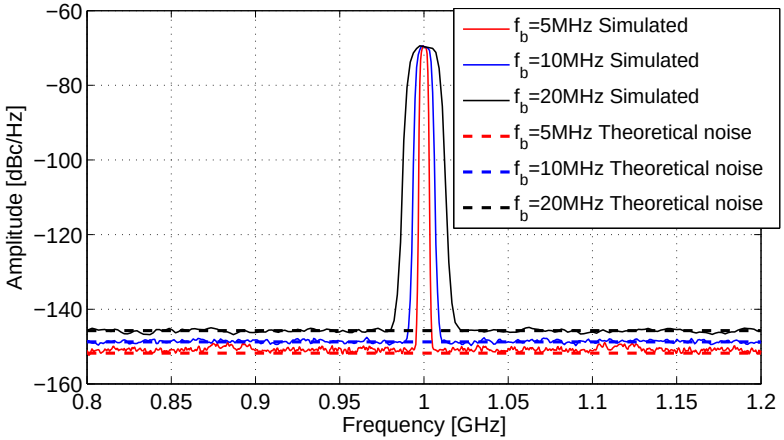

Figure 4.11: Transmitted spectrum from simulations and theoretical noise level for different bandwidths f_b with f_s = 1THz and f_c = 1GHz

Note that according to equations (4.13) and (4.16), the higher the bandwidth is, the lower the CNR will be. In order to simplify the comparison of different bandwidth signals, the amplitude A is tuned for different bandwidth signals in order to equalize the in-band power spectral level as shown in figure 4.11. Once again it can be seen that the theoretical and simulated out-of-band levels do agree.

Carrier frequency

Now, the effect of changing the carrier frequency f_c is investigated. Note that our derivation in section 4.4.2 relied on the fact that $f_c \ll f_s$. When the carrier frequency and sampling frequency become comparable in magnitude, then the exact formula for $R_{\tilde{e}\tilde{e}}(\omega)$ in equation (4.32) should be used. In our simulation we assume the realistic case that the sampling frequency is much higher than the carrier frequency.

Figure 4.12 shows the power spectral density of 2 transmitted signals at different carrier frequencies f_c = 1GHz and f_c = 1.5GHz together with the theoretical noise level. Again the simulated out-of-band noise agree with the theoretical noise levels.

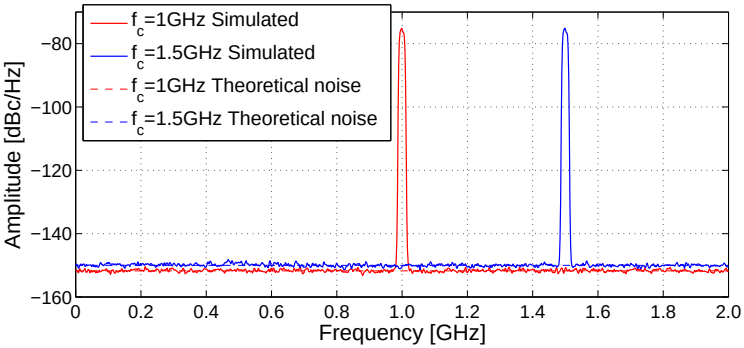

Figure 4.12: Transmitted spectrum from simulations and theoretical noise level for different carrier frequencies f_c , with f_s = 1THz and f_b = 20MHz

DCO

Finally, we investigate the difference between the generated spectra when using a DTC or DCO based polar transmitter. For having a fair comparison, the frequency grid of the DCO is set equal to the time grid of the DTC. This ensures a fair comparison of both devices. Figure 4.13 shows the spectrum of 2 transmitted signals using a DTC and a DCO.

The main difference between both signals is the harmonics. However, if we consider the frequency range around ω_c, we notice that the noise floor of the DCO is slightly higher than the DTC. This corresponds to the 2dB difference between the CNR_{DTC} and CNR_{DCO}. Note, that the amplitude of the DCO output signal is tuned, so that both transmitted signals have the same in-band power level.

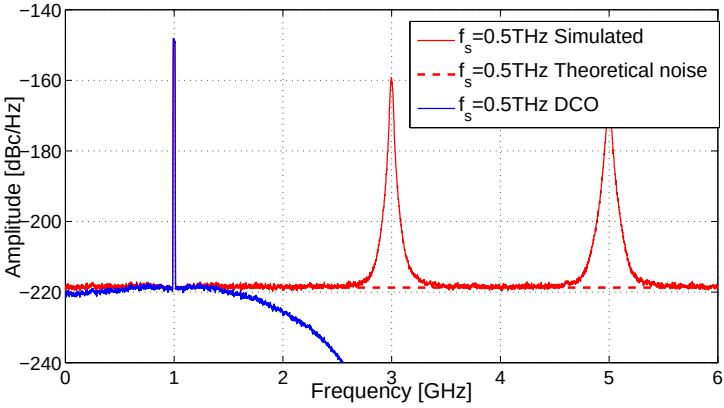

Figure 4.13: Transmitted spectrum using DCO and DTC with f_c = 1GHz, f_s = 0.5THz and f_b = 20MHz

5. Radius processing

In the previous chapter, we described how to generate a phase modulated signal from the baseband phase signal. In this chapter, the amplitude modulation in a polar transmitter is described. Amplitude modulation is simpler than phase modulation. Nevertheless, there are still some challenges for an ideal conversion of the digital radius signal $r[n]$ which is generated by the CORDIC to the theoretical analog radius signal $r(t)$.

This chapter can be divided into four parts. In the first part, an overview about the basics of the DAC and its application in polar transmitters is presented. In the second part, the relationship between the DAC and the PA is explained. In the third part, the distortions introduced by the DAC and their effect on the transmitted signal is introduced. Finally, we introduce a novel signal processing algorithm which relaxes the requirements of time resolution in the DTC by processing the digital radius signal. Note that in our subsequent explanations, we will assume the usage of a DTC in the phase branch instead of DCO.

5.1. Digital-to-Analog Converter

In digital communications, binary information is converted into an analog electromagnetic wave by a series of digital and analog processing operations. In any transmitter architecture, the interface between the digital and analog domains is done using a DAC.

DACs have several limitations. The most common limitation is the sampling rate of the input digital signal. In traditional IQ transmitters, the DAC is mostly present in baseband, where the sampling rate is low and is equal to or slightly higher than the Baud rate. However, in polar transmitters the DAC is placed closer to the RF front-end, and is therefore denoted as RF-DAC [Boos et al., 2011].

In polar transmitters, the DAC should be able to operate at sampling rates close to the carrier frequency. This implies that the DAC should be able to support sampling rates in the range of $1-5$ GHz for mobile communication standards. This is a challenging task given the current hardware capabilities. In this section, we give a mathematical model of an ideal DAC as well as a brief overview about the DAC hardware architecture which is used in the polar transmitter.

5.1.1. Mathematical model

Assume that the input digital signal to a DAC is denoted as the binary vector of

$$\bar{b} = [b_{L-1}, b_{L-2}, ..., b_1, b_0] \quad , \quad b_i \in \{0, 1\} \, , \tag{5.1}$$

where L is the number of bits representing the word-length, b_0 is the Least Significant Bit (LSB), and b_{L-1} is the most significant bit (MSB). Ideally, the DAC converts each digital word into the analog signal defined as

$$u = q_{DAC} \cdot \sum_{i=0}^{L-1} 2^i \cdot b_i \tag{5.2}$$

$$= q_{DAC} \cdot r \, , \tag{5.3}$$

where q_{DAC} is the smallest amplitude change that the DAC can generate and corresponds to the amplitude of the LSB, and r is the integer representation of the binary number $\bar{b}$. Assuming that the digital signal operates at a sampling rate of f_s, the impulse response of the DAC can be denoted as

$$h_{DAC}(t) = q_{DAC} \cdot \text{rect}(f_s \cdot t) \, , \tag{5.4}$$

where rect is defined in this chapter as

$$\text{rect}(t) = \begin{cases} 1 & \text{for} \quad 0 < t < 1 \, , \\ 0 & \text{otherwise.} \end{cases} \tag{5.5}$$

When an input sequence of binary words r_j is fed into the DAC, the output $v(t)$ can be denoted as

$$u(t) = \sum_{j=0}^{\infty} r_j \cdot q_{DAC} \cdot h_{DAC}(t - \frac{j}{f_s}) \, . \tag{5.6}$$

This is a staircase function where the output $v(t)$ is kept constant for the sampling duration of $1/f_s$.

5.1.2. Architectures

The hardware architectures of DAC can be divided into 3 main classes:

- Pulse-width-modulation DAC.
- Integrating DAC.

- Current weighting using ladder networks.

Each class is tailored to the requirements of the application. However, speed vs resolution is the basic trade-off in DACs. For RF applications with near GHz sampling rates, we obviously require high speed rather than resolution.

The suitable class of DACs for the speed requirements of the polar transmitters is the current weighting using ladder networks [Van de Plassche, 1994], which is commonly called *current steering* DAC [Rezzi et al., 1997]. Figure 5.1 shows the basic principle of current steering DAC. The DAC is composed of an array of current sources, each weighted according to the binary bit weigh, with a minimal output current I_o corresponding to the LSB. Every bit b_i of the input digital word is either 0 or 1 corresponding to low or high voltage, respectively. Each bit is connected to the base of a transistor which acts as a switch. When a bit is high, the switch between the emitter and collector is closed and the corresponding current $2^i I_0$ flows. All currents are then summed up to give the output current I_{out} which corresponds to the analog output signal.

Later, the current can be converted into voltage using a resistor. The resistor is not included in figure 5.1 as there are some approaches which use the current to directly modulate the carrier signal using switching transistors instead of using resistors [Shameli et al., 2006]. This topology is highly favorable for RF applications due to the ability of the transistor to support high switching rates of the input bit stream [Clara, 2013].

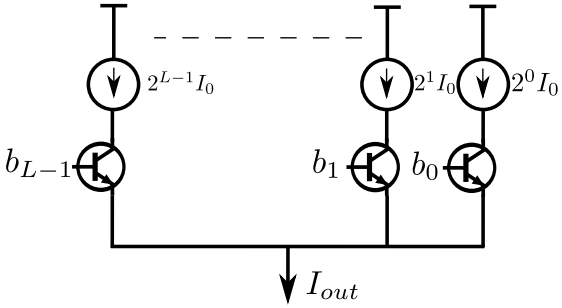

Figure 5.1: Principle of current steering DAC

5.2. Radius and power amplifiers

In the previous section, an overview about how the digital radius signal $r[n]$ is converted to an analog signal $r(t)$ was presented. In this section, we explain how the radius is used

to drive the power amplifier.

Recall that one of the prime advantages of polar transmitters is their power efficiency. This is achieved by the way amplitude modulation is done in polar transmitters.

In transmitters, a great amount of energy is consumed by the PA [Lopez et al., 2009]. Ideally, the PA should linearly scale the input signal to a larger amplitude signal. However, there is always a trade-off between linearity and efficiency of PAs. Figure 5.2 shows the typical transfer function of a PA. The PA operates either in the linear region where the PA is not power efficient, or in the saturation region where the transfer function is not linear but the PA is power efficient.

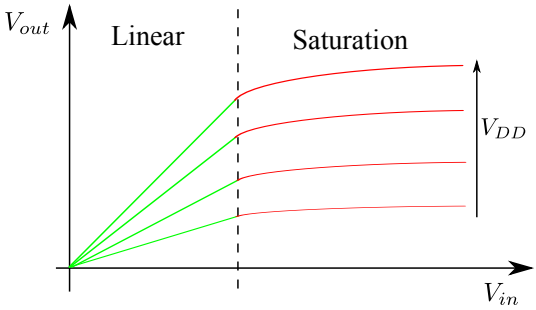

Figure 5.2: Typical PA transfer function

In IQ transmitters, $i(t)$ and $q(t)$ channels are used to modulate the carrier signal at low voltage. The low voltage modulated analog signals are then summed up and the output is amplified using a PA which must be linear in order to avoid modulation errors. Operating the PA in the linear mode makes the PA non-efficient. Several approaches exist in order to operate the PA in the saturation mode while *linearizing* the PA using predistortion [Cavers, 1990][Ding et al., 2004].

On the other hand, polar transmitters use the PA in a different way to amplify the transmitted signal. Instead of multiplying the phase modulated signal from the DTC/DCO with the analog radius produced by the DAC and then use a PA to amplify the low voltage transmit signal, the polar transmitter couples the recombination of radius and phase with the amplification in a single process at the PA.

This is done by using the radius signal $r(t)$ from the DAC to drive the supply voltage V_{DD} of the PA. Since the phase modulated signal has a constant amplitude when using a DTC, the PA can be used in the saturation region to amplify the fixed amplitude output

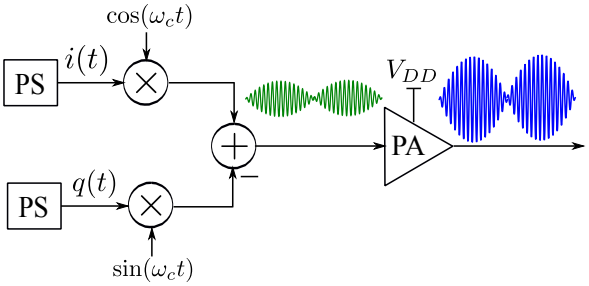

(a) PA operating in linear non-efficient mode in IQ transmitter

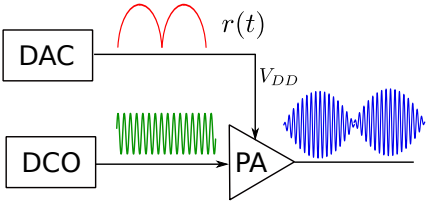

(b) PA operating in saturation efficient mode in polar transmitter

Figure 5.3: PA operation in IQ and polar transmitters

of the DTC/DCO, while continuously driving the supply voltage V_{DD} using the radius signal $r(t)$.

From figure 5.2 we see that by changing the supply voltage, the output voltage V_{out} is pulled up linearly while still operating in the efficient saturation region. This means that the PA never operates in the linear non-efficient region. Figure 5.3 compares the usage of the PA in case of IQ transmitters and polar transmitters. Note that in case of IQ transmitters, the input to the PA in figure 5.3a has a varying amplitude but with fixed supply voltage, whereas in case of polar transmitter in figure 5.3b, the input signal has a fixed amplitude but varying supply voltage.

5.3. DAC distortions

In section 5.1.1, a theoretical mathematical model of the DAC has been presented. In reality, the polar transmitter DAC introduces some distortions in the conversion of $r[n]$ to $r(t)$. In this section, an overview about the effect of some of the known DAC distortions on the spectrum of the transmitted signal will be discussed. There are several

hardware distortions which influence the ideal performance of the DAC such as glitching, settling time, and non-linearity [Van de Plassche, 1994]. However, we focus in this thesis on the imperfections which directly influence the spectrum of the transmitted signal.

5.3.1. DAC averaging

The most significant limitation of the DAC is the maximum sampling rate of the input digital signal. In audio applications the sampling rate is known to be 44.1 kHz. With the emerging HDTV applications and ultra wide band communications, there has been a need to have DACs which support high sampling rates. High sampling rates reported in literature are in the range of 100-500 MHz [Ginsburg and Chandrakasan, 2007] [Eto et al., 2000] [Zhou and Yuan, 2003]. However, the radius signal $r[n]$ operates on a sampling rate in the range of THz. This implies that down-sampling the radius signal from THz to GHz range will incur averaging of the radius signal over time, in order to accommodate the maximum sampling rates that the DAC can support.

As mentioned earlier, DACs have a trade-off between resolution and sampling rate. In this section, we assume infinite precision of the digital signal in order to isolate the effect of the sampling rate.

In order to investigate the effect of the sampling rate of the DAC, we model the DAC as a device which performs two consecutive operations:

- First, it takes a digital signal $r[n]$ operating at a high frequency f_s as an input and generates an intermediate digital radius signal $\bar{r}[m]$ operating at a sampling rate of f_l. The down-sampling operation is done by averaging every group of samples in $r[n]$ into a single sample in $\bar{r}[m]$. The averaging process is similar to decimation, but with the difference that the averaging of all samples within the decimation period is done instead of selecting a single sample.
- The low rate signal $\bar{r}[m]$ is then converted to the analog signal $\hat{r}_{avr}(t)$ using the principle explained in section 5.1.1.

It is worth noting that, ideally, the radius signal $r[n]$ would operate on a low sampling frequency f_l. Consequently, no down-sampling would be needed before feeding it to the PA. However, the radius $r[n]$ operates at a high frequency as the CORDIC in figure 2.9 needs to operate on a high frequency, so that the phase signal $\theta[n]$ is computed with high time resolution. This translates to a high precision computation of the instantaneous period. Hence, the high sampling rate of $r[n]$ is a by-product of operating the CORDIC at a high sampling rate.

The overall model of the DAC can be represented as

$$\underbrace{r[n] \rightarrow \bar{r}[m] \rightarrow \hat{r}_{avr}(t)}_{DAC} \ . \tag{5.7}$$

This is only a model of the averaging process. In reality, the radius signal is generated at a low rate from the CORDIC. There are two possible methods to operate the averaging process of the DAC: fixed rate averaging and data dependent averaging.

Fixed rate averaging

Assuming that $N = f_s/f_l$ is an integer number, then every N samples in $r[n]$ are averaged to a single value in $\bar{r}[m]$. This can be modeled as

$$\bar{r}[m] \quad = \quad \frac{1}{N} \cdot \sum_{i=0}^{N-1} r[m \cdot N + i] \ . \tag{5.8}$$

This way, the DAC is clocked with a square wave signal operating at a fixed frequency f_l. The generated analog signal $\hat{r}_{avr}(t)$ is a staircase function which has a fixed period per level of $1/f_l$ seconds. The smaller N is, the closer $\hat{r}_{avr}(t)$ would be to the theoretical signal $r(t)$.

Figure 5.4 summarizes the averaging operation of the DAC. As shown the averaged signal $\bar{r}[m]$ is later convolved with $h_{DAC}(t)$ which is a rectangular pulse with the duration of $1/f_l$ seconds.

Data dependent averaging

In this variant, the averaging rate of the DAC is not fixed, but rather dependent on the instantaneous period υ of the DTC. The instantaneous period υ is known to vary from $1/(2f_c)$ to $3/(2f_c)$ depending on the baseband phase signal. The square wave DTC signal $\bar{m}(t)$ can be used to clock the DAC so that the averaging process is coupled with the DTC's output signal. This means that each instantaneous period $f_s \cdot \upsilon[m]$ (in samples) corresponds to an averaged value $\bar{r}[m]$ which can be calculated as

$$\bar{r}[m] \quad = \quad \frac{1}{f_s \cdot \upsilon[m]} \cdot \sum_{i=0}^{f_s \cdot \upsilon[m]-1} r\left[\sum_{j=-\infty}^{m-1} \upsilon[j] + i\right] \ . \tag{5.9}$$

The averaging operation can happen at an even faster rate when several samples of the averaged signal $\bar{r}[m]$ are generated within a square pulse of the DTC. The best way to define the data-dependent averaging is by denoting an averaging phase interval θ_{av}.

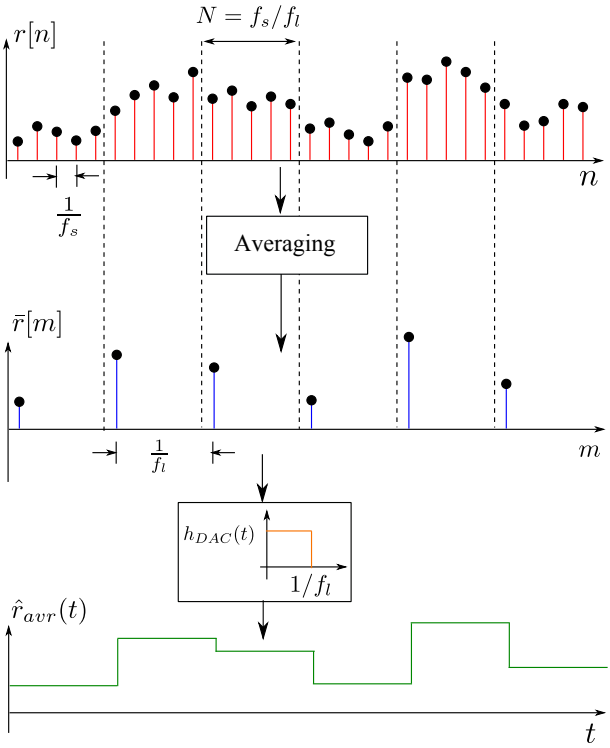

Figure 5.4: Averaging operation of the DAC using fixed rate clock

The averaging phase defines the number of samples $\bar{r}[m]$ per DTC square period. For example, in case of $\theta_{av} = 2\pi$, $\bar{r}[m]$ has a single sample for a whole square wave period $\upsilon[m]$. In case $\theta_{av} = 2\pi/2$, $\bar{r}[m]$ has two samples per period $\upsilon[m]$, and so on.

Figure 5.5 summarizes the data-dependent DAC averaging operation. Note that in this case, the DAC can mo longer be described by an LTI system since the pulse duration of the rectangular signal is time dependent.

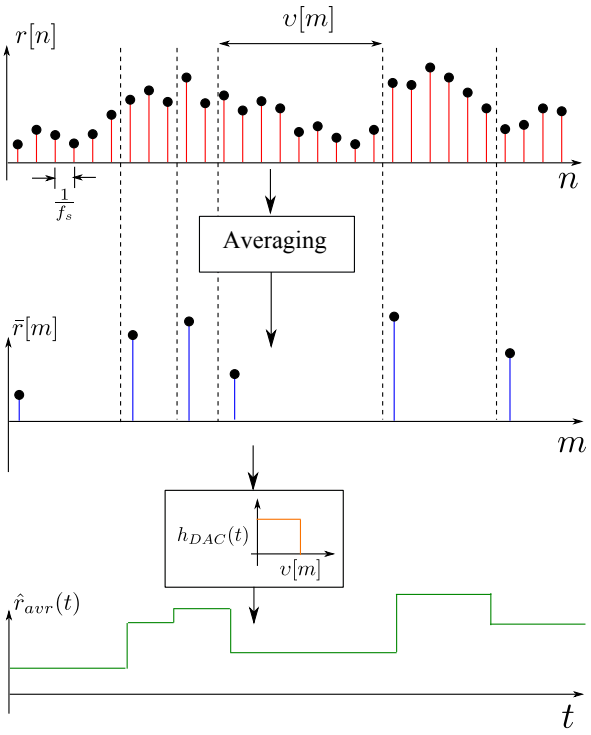

Figure 5.5: Averaging operation of the DAC using a data-dependent clock

Simulation

In this section, the effect of DAC averaging on the spectrum of the transmitted signal is investigated. A 20MHz reference signal is simulated without averaging as a reference. The sampling rate is f_s = 1THz.

For the fixed rate averaging case in figure 5.6, the averaging frequency is swept from $f_{av} = f_c/6$ to $f_{av} = f_c$, where $f_c = 1$GHz is the carrier frequency. For the data-dependent case in figure 5.7, the averaging angle is swept from $\theta_{av} = 2\pi/4$ to $\theta_{av} = 2\pi$. Figure 5.8 compares the difference between fixed-rate averaging and data-dependent averaging when $f_{av} = f_c$ and $\theta_{av} = 2\pi$.

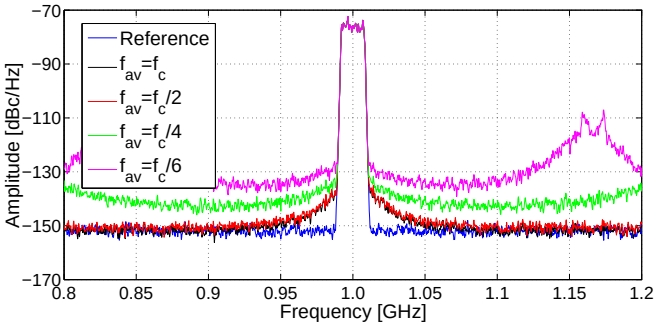

Figure 5.6: Averaging operation of the DAC using fixed rate clock with different averaging rates f_{av}

We can observe from figures 5.6, 5.7, and 5.8 that the out-of-band noise raises faster when we increase the averaging frequency f_{av} compared to reducing θ_{av}. Additionally, there is no remarkable difference between the fixed rate averaging and data-dependent averaging for more or less similar averaging rates. Based on those observations, we can say that there is no need to dedicate a fixed rate clock for the DAC since the DTC signal can be safely used as a clock signal. However, this comes on the expense that the DAC should support the maximum possible instantaneous frequency $2f_c$ which corresponds to the lowest possible instantaneous period $1/(2f_c)$.

5.3.2. Radius quantization

The DAC converts a discrete-time discrete-amplitude input signal $r[n]$ into a continuous-time continuous-amplitude signal $r(t)$. As stated in section 5.1.2, there is a trade-off between the resolution of the DAC (number of bits to represent a word in $r[n]$) and the efficiency of its power consumption. This is intuitive since for each extra bit there is an extra transistor, as shown in figure 5.1, which consumes extra current from the power source. Since power efficiency is critical in mobile communication devices, it is desirable to know the effect of truncating the word-length of the digital radius

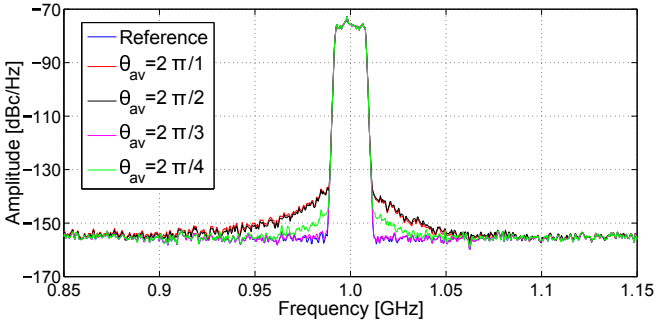

Figure 5.7: Averaging operation of the DAC using a data-dependent clock with different averaging phases θ_{av}

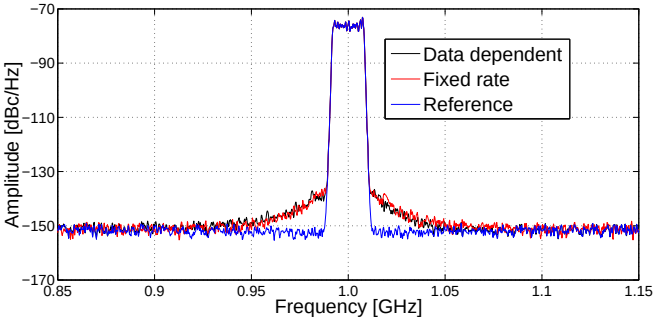

Figure 5.8: Comparison between fixed rate averaging and data-dependent averaging

signal $r[n]$ on the spectrum of the transmitted signal. In order to isolate the effect of radius quantization, we assume that the DAC does not average the input digital signal as explained earlier.

The transmitted signal including radius quantization at the DAC and time quantization at the DTC can be modeled as

$$\hat{s}(t) = [r(t) + e_r(t)] \cdot [\text{sgn}(\cos(\omega_c t + \theta(t))) + \bar{e}(t)] \tag{5.10}$$

$$= r(t)\text{sgn}(\cos(\omega_c t + \theta(t))) + r(t)\bar{e}(t) + e_r(t)\text{sgn}(\cos(\omega_c t + \theta(t))) + e_r(t)\bar{e}(t) \ , \tag{5.11}$$

where $\bar{e}(t)$ is the time quantization error explained in section 4.4. The first term in equation (5.11), $r(t)\text{sgn}(\cos(\omega_c t+\theta(t)))$, is the desired transmitted signal which has a flat spectrum around f_c and its harmonics. The second term $r(t)e_t(t)$ is the time quantization error and its spectrum was derived in section 4.4.2. In this section we evaluate the spectrum of the third and fourth terms by simulations.

Simulation

A 20MHz bandwidth signal is simulated with a sampling rate of 1THz for the DTC and the radius signal $r[n]$. The quantization effect is investigated by sweeping the word-length of the radius signal from 4 to 10 bits. Note that in this section, the effect of amplitude clipping will not be investigated, which is commonly used to enhance the efficiency of the PA [Junqing et al., 2012]. From figure 5.9, we can conclude that every bit in the radius branch corresponds to around 8 dB reduction in the out-of-band noise. Using a word-length more than 8 does not have any further improvement on the reduction of the out-of-band noise, since the time quantization component in equation (5.11) becomes dominant.

5.3.3. Pulse shape

The final investigation of the DAC distortions is the DAC pulse shape. Recall in section 5.1.1 that the DAC impulse response $h_{DAC}(t)$ can be modeled as a rectangular pulse. This results in a staircase analog signal. It is possible to add an analog integrator circuit after the DAC. This integrator changes the overall pulse shape of the DAC from a rectangular pulse to a linearly increasing pulse from one digital sample to the next.

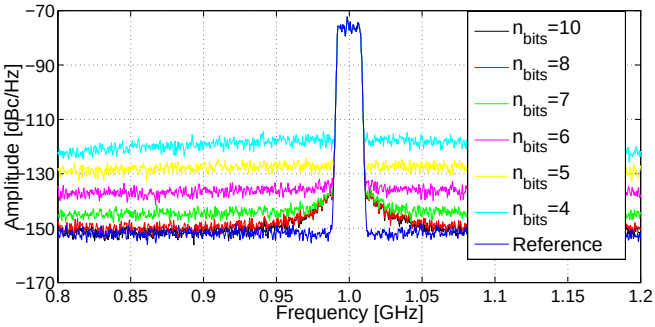

Figure 5.9: Spectrum of transmitted signal for different radius word-lengths n_{bits}

Pulse model

Consider 3 consecutive radius samples $r[1]$, $r[2]$, and $r[3]$. When using a linear pulse, the analog output during the time of the middle pulse $r[2]$ becomes a linear function of the current, past, and future samples, and can be represented as

$$r_2(t) \quad = \quad \frac{r[3]-r[1]}{2T_{pulse}}t + \frac{r[2]+r[1]}{2} \ , \tag{5.12}$$

where T_{pulse} is the time duration of $r[2]$'s pulse, which can be either fixed or data-dependent as explained in section 5.3.1, and t starts from $t = 0$ till $t = T_{pulse}$.

Simulation

Figure 5.10 compares the spectrum of the transmitted signal when using a fixed rate DAC averaging with rectangular pulses and when using linear pulses as explained in this section. As shown, linear pulses reduce the out-of-band noise which is close to the in-band region, because linear pulses are considered a higher order approximation of the exact radius signal $r[n]$.

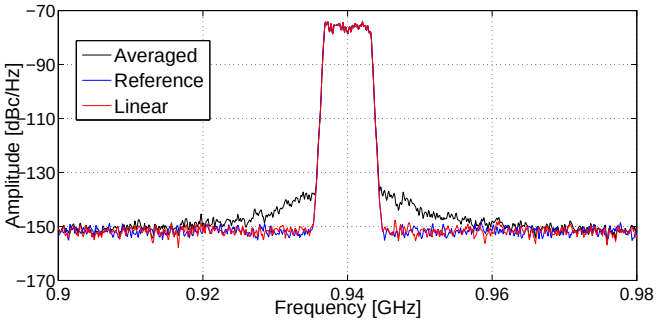

Figure 5.10: Spectrum of transmitted signal for rectangular and linear pulse shapes

5.4. DAC oversampling

As stated previously, the current challenge of using DACs in mobile communication applications is the ability to operate the DAC at GHz sampling rates. However, as semiconductor technologies are getting more and more advanced reaching down to 12 nm [Ban et al., 2008], one can safely predict that in the foreseeable future, DACs will be able to support multi-GHz sampling rates. This fact will not only help having an accurate DAC which eliminates the averaging distortion explained in section 5.3.1, but also offers the signal processing domain more degree of freedom to process the radius signal in order to improve the quality of the transmitted signal by reducing the out-of-band noise.

Mobile communications operate at different carrier frequencies. From section 4.4, we know that the higher the carrier frequency, the higher the out-of-band noise floor due to time quantization, and thus the lower the CNR. The only way to reduce the noise floor is to increase the sampling rate f_s of the DTC. This means that in order to support CNR of all carrier frequencies, we need to have a sampling rate f_s which can support the minimum CNR of the highest carrier frequency in all the communication protocols supported by the mobile device. This implies that for low carrier frequencies the CNR is *too good* because the sampling rate is too high, leading to an excessive power consumption from the DTC.

The question at this point: Is there a way to reduce the out-of-band noise without increasing the sampling rate of the DTC? In this section a novel algorithm will be presented which tackles this question. The algorithm, which is presented in Ibrahim et al. [2014] and Ibrahim and A. [2014a], can reduce the out-of-band noise while keeping the

sampling rate of the DTC fixed. The algorithm processes the digital radius signal prior to the DAC. In this approach, there is no need to average the radius as explained in section 5.3.1. However, the reduced out-of-band noise comes at the expense of operating the DAC at higher sampling rates than the carrier frequency. Ultimately, the algorithm relaxes the sampling rate requirement for a given CNR by offering a trade-off between the sampling rate of the DTC and the sampling rate of the DAC.

This section is organized as follows: First, an analysis of the out-of-band noise will be presented. Second, two variants of the algorithms will be explained. Third, a qualitative explanation of why the proposed algorithm reduces the out-of-band noise will be stated. Finally, results of the algorithm will be shown.

5.4.1. Out-of-band noise

Before explaining the proposed DAC oversampling algorithm, we first present a wrap-up of the constituents of the out-of-band noise explained up till now. Assuming we have perfect baseband filters, pulse shaping filters and CORDIC, the theoretical passband signal can be defined as

$$s(t) = r(t) \cdot A \cdot \cos(\omega_c t + \theta(t)) \,, \tag{5.13}$$

where $s(t)$ has a flat PSD $R_{ss}(\omega)$ around $\omega = \omega_c$ and no out-of-band noise. Throughout this section, it is assumed that the amplitude of the DTC output $\bar{m}(t)$ includes the term A.

However, due to non-ideal hardware implementation, a distorted signal is transmitted which can be represented as

$$\begin{aligned} \hat{s}_r(t) &= \hat{r}_r(t) \cdot A \cdot [\mathrm{sgn}(\cos(\omega_c t + \theta(t))) + \bar{e}(t)] \\ &= \hat{r}_r(t)\bar{m}_o(t) + A \cdot \hat{r}_r(t)\bar{e}(t) \,, \end{aligned} \tag{5.14}$$

where $\bar{e}(t)$ is the time quantization error explained in section 4.4, and $\hat{r}_r(t)$ is the radius signal distorted by DAC.

Comparing equations (5.14) and (5.13), we can see that there are differences between the theoretical and distorted signal. Figure 5.11 highlights the difference between the actual and theoretical transmitted signals in the time domain.

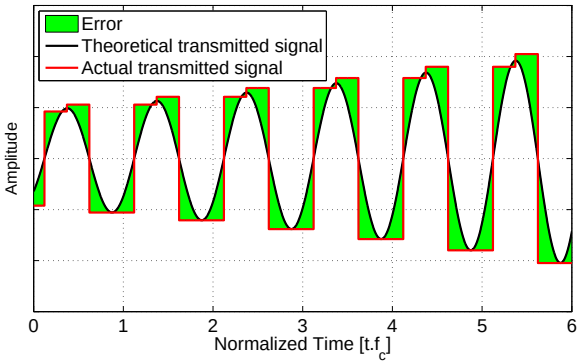

Figure 5.11: Theoretical transmitted signal vs actual transmitted signal using DTC

Cos-approximation error

The DTC generates square waves with variable periods instead of continuous-time phase modulated cosine waves. This introduces the so called cos-approximation error

$$e_c(t) = A \cdot \text{sgn}(\cos(\omega_c t + \theta(t))) - \frac{4}{\pi} \cdot A \cdot \cos(\omega_c t + \theta(t)) \; . \tag{5.15}$$

In appendix B, it has been shown that

$$\begin{aligned} \bar{m}_o(t) &= A \cdot \text{sgn}(\cos(\omega_c t + \theta(t))) \\ &= A \cdot \frac{4}{\pi} \sum_{k=1}^{\infty} \frac{1}{2k-1} \cos\left((2k-1)(\omega_c t + \theta(t))\right) \; . \end{aligned} \tag{5.16}$$

Consequently,

$$e_c(t) = A \cdot \frac{4}{\pi} \sum_{k=2}^{\infty} \frac{1}{2k-1} \cos\left((2k-1)(\omega_c t + \theta(t))\right) \; . \tag{5.17}$$

Now, the distorted transmitted signal can be represented as

$$\begin{aligned} \hat{s}_r(t) &= \frac{4}{\pi} \cdot A \cdot \hat{r}_r(t) \cdot \cos(\omega_c t + \theta(t)) + \hat{r}_r(t) e_c(t) + A \cdot \hat{r}_r(t) \bar{e}(t) \\ &= \frac{4}{\pi} s(t) + \frac{4A}{\pi} \sum_{k=2}^{\infty} \frac{1}{2k-1} \hat{r}_r(t) \cos\left((2k-1)(\omega_c t + \theta(t))\right) + A \hat{r}_r(t) \bar{e}(t) \end{aligned} \tag{5.18}$$

Equation (5.18) shows that the transmitted signal contains the theoretical signal $s(t)$ with flat spectrum centered around ω_c and no out-of-band noise. In addition, the second term in equation (5.18) contains damped versions of the signal centered around the odd harmonics of the carrier $(2k-1)\omega_c$ starting with $k = 2$. Simulations will show later that these versions around odd harmonics are not only damped according to the factor $\frac{1}{2k-1}$, but are also smeared in spectrum. The reason for this is that the same radius signal $\hat{r}_r(t)$ is coupled with a faster phase signal $(2k-1)\theta(t)$ which results in a broader spectrum around the harmonics $(2k-1)\omega_c$ compared to the original signal $s(t)$.

Time quantization error

The second distortion introduced is the time quantization, which is previously explained in section 4.4. From equation (5.18), we can see that the time quantization error in the transmitted signal can be denoted as

$$\hat{q}(t) \quad = \quad \hat{r}_r(t)\bar{e}(t) \; . \tag{5.19}$$

Assuming that the DAC distortions are not high, then we can use the results from section 4.4 which assume $\hat{r}_r(t) \approx r(t)$. From section 4.4, we know that the spectrum of $\hat{q}(t)$ is flat around the carrier frequency with PSD

$$R_{\hat{q}\hat{q}}(\omega_c) \quad \approx \quad 4A^2 \frac{f_c}{f_s^2}\left(\frac{1}{6} - \frac{1}{120}(\frac{\omega_c}{2f_s})^2\right)\sigma_s^2 \; . \tag{5.20}$$

Verification

In the previous sections, it was shown that the out-of-band noise has two constituents:

- A cos-approximation error, which is expected to be composed of smeared and damped versions of the theoretical spectrum of $s(t)$ centered around the odd harmonics of the carrier frequency.
- A time quantization error which has a flat spectrum.

In this section, we verify those two out-of-band components by simulating a transmitted signal $\hat{s}_r(t)$ which incorporates cos-approximation error and time quantization. A comparison of the spectrum of the transmitted signal with the spectrum of the cos-approximation error $\hat{r}_r(t)e_c(t)$ in equation (5.18) will be presented, as well as the spectrum of the time quantization error $\hat{r}_r(t)\bar{e}(t)$ in equation (5.19).

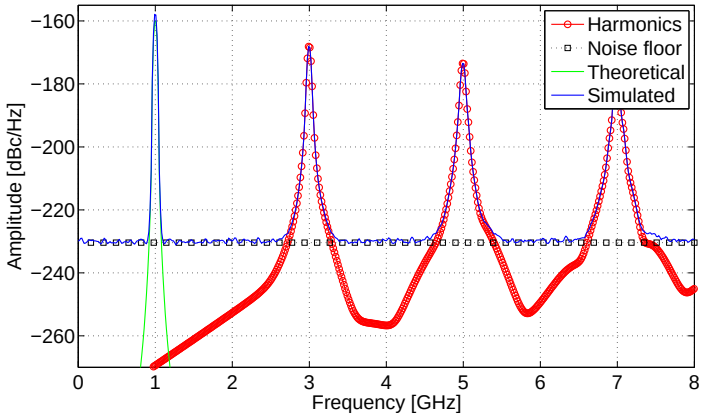

Figure 5.12: Averaging operation of the DAC using fixed rate clock

Figure 5.12 shows that the spectrum of $\hat{s}_r(t)$ has smeared damped versions of $s(t)$ around the odd harmonics of the carrier. This agrees with the theoretical spectrum of the harmonics mentioned in section 5.4.1. Similarly, the spectrum of the time quantization error agrees with the spectrum of the noise floor of the transmitted signal $\hat{s}_r(t)$.

5.4.2. Algorithm

In the previous section, we identified the main components of the out-of-band noise. Now an explanation of how can the proposed algorithm reduce the out-of-band noise by modifying the operation of the DAC will be discussed.

Recall that the polar transmitter should transmit the following theoretical signal

$$s(t) \quad = \quad \underbrace{r(t)}_{DAC} \cdot \underbrace{\cos(\omega_c t + \theta(t))}_{DTC} \; . \tag{5.21}$$

As indicated, the DAC is responsible of generating the amplitude part of the signal $r(t)$, and the DTC is responsible of generating the phase modulated signal $\cos(\omega_c t + \theta(t))$. In practice, both devices introduce distortions. The DAC averages and quantizes the radius signal, and the DTC generates square waves with discrete sampling instants. Considering the DTC, we can say that part of the phase information is lost when the theoretical continuous-time signal $\cos(\omega_c t + \theta(t))$ is replaced with a square wave

$\text{sgn}(\cos(\omega_c t + \theta(t)))$. This happens due to the use of square waves instead of cosine waves at the DTC. We define the phase information as the information in the signal $|\cos(\omega_c t + \theta(t))|$. Although the signal $|\cos(\omega_c t + \theta(t))|$ is a variable amplitude signal, however, the reason the amplitude is varying is due to the phase information $\omega_c t + \theta(t)$, hence we refer to this signal as the phase information. The proposed algorithm tries to restore the lost phase information due to the usage of square waves.

In this method, the phase information is repartitioned by moving part of the phase information from the DTC to the DAC. This way, the assignment of the transmitted signal becomes

$$\begin{aligned} s(t) &= \underbrace{r(t)|\cos(\omega_c t + \theta(t))|}_{DAC} \cdot \underbrace{\text{sgn}(\cos(\omega_c t + \theta(t)))}_{DTC} \\ &= r_p(t) \cdot \bar{m}(t) \ . \end{aligned} \tag{5.22}$$

Theoretically, equations (5.22) and (5.21) are identical. However in practice, shifting a portion of the phase information contained in the term $|\cos(\omega_c t + \theta(t))|$ to the DAC, offers us a higher degree of freedom and eliminates the distortion introduced by the DTC.

Recall from section 5.3.1 that the DAC can generate a single amplitude during the instantaneous period of the transmitted signal. However, within the instantaneous period, the term $|\cos(\omega_c t + \theta(t))|$ changes continuously from 0 to 1. This means that the DAC should be able to operate at sampling rates higher than f_c in order to generate the phase information contained in the term $|\cos(\omega_c t + \theta(t))|$. Figure 5.13 shows the basic principle of the oversampling algorithm.

When the DAC operates at the higher sampling rates, it will generate a staircase wave function within each instantaneous period. When comparing the staircase wave function to the theoretical function $|\cos(\omega_c t + \theta(t))|$, we can see that the difference between both functions resembles a quantization error, which will be denoted as $e_p(t)$. At this point, the output of the DAC and DTC can be represented as

$$\begin{aligned} &\text{DAC:} \quad \hat{r}_p(t) = r_p(t) + e_p(t) \ . \\ &\text{DTC:} \quad \bar{m}(t) = \bar{m}_o(t) + \bar{e}(t) \ , \end{aligned} \tag{5.23}$$

where $e_p(t)$ is the error made at the DAC output for quantizing the signal $r(t)|\cos(\omega_c t + \theta(t))|$ and $\bar{e}(t)$ is the time quantization error at the DTC output due to discrete sampling instants. Using those notations, the transmitted signal for an oversampled DAC becomes

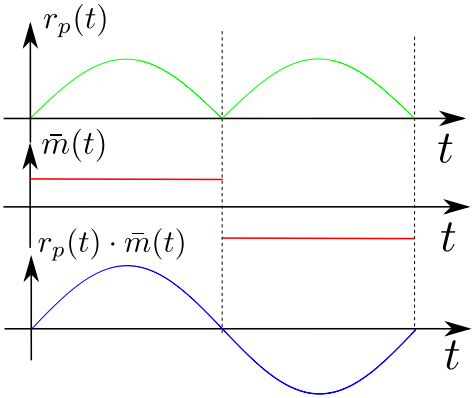

Figure 5.13: Oversampling principle

$$\begin{aligned} \ddot{s}(t) &= \hat{r}_p(t)\bar{m}(t) \\ &= r_p(t)\bar{m}_o(t) + r_p(t)\bar{e}(t) + e_p(t)\bar{m}_o(t) + e_p(t)\bar{e}(t) \ . \end{aligned} \tag{5.24}$$

As mentioned, the DAC quantizes the theoretical signal $r_p(t)$. There are two methods to do this quantization operation: Amplitude quantization and phase quantization. The difference between both methods can be described using figure 5.14. As the name suggests, in amplitude quantization a quantization grid is set based on the amplitude value of $r_p(t)$, whereas in phase quantization, the quantization grid is based on the phase of $r_p(t)$.

Before going into the details of the difference between both quantization methods, recall that the DAC can be clocked either by a fixed rate clock or a data-dependent clock (section 5.3.1). In this algorithm, the DAC must be clocked using a data-dependent clock in order to couple the oversampled radius signal to the square wave output of the DTC. The *data* used to generate the clock is based on the RF phase defined as

$$\begin{aligned} \breve{\theta}_m(t) &= \text{mod}\ (\omega_c t + \theta(t), \pi) \\ &= \text{mod}\ (\breve{\theta}(t), \pi) \ , \end{aligned} \tag{5.25}$$

where mod is the modulus operator. This modification preserves the condition that $|\sin(\breve{\theta}(t))| = \sin(\breve{\theta}_m(t))$. For each quantization method, we explain how the clock signal

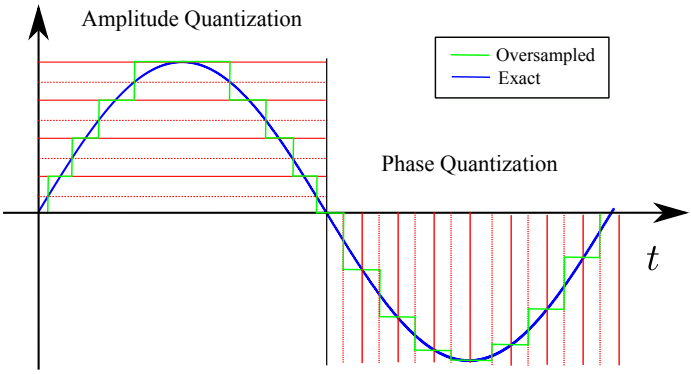

Figure 5.14: Phase vs amplitude quantization

is extracted from $\breve{\theta}_m$. We will use the sine wave instead of the cosine wave as the square wave (based on sine wave) toggles its amplitude when $\breve{\theta}_m$ toggles from π to 0. This simplifies clocking of the DTC and DAC using $\breve{\theta}_m$.

In the subsequent description of the algorithm, the continuous-time index (t) will be used instead of discrete time index $[n]$. It is assumed that the continuous-time signal is a stepwise defined function of the digital signal, where each step has a duration of $1/f_s$. Of course, the algorithm operates on digital signals, but the produced signal is analog. Therefore, it is more convenient to use the continuous-time notation.

Amplitude quantization

In this method, the DAC output can be represented as

$$\hat{r}_{qa}(t) \quad = \quad \hat{r}_r(t) Q\left(|\sin(\omega_c t + \theta(t))|\right) \ , \tag{5.26}$$

where the quantization error of $Q(\cdot)$ is

$$e_{qa}(t) \quad = \quad Q\left(|\sin(\omega_c t + \theta(t))|\right) - |\sin(\omega_c t + \theta(t))| \ . \tag{5.27}$$

Using amplitude quantization, the quantization error $e_{qa}(t)$ has a maximum amplitude of $q_a/2$, where q_a is the step size of the quantization grid. The quantization operation in equation (5.27) can be shifted inside the sine operator so that we obtain

$$Q(|\sin(\omega_c t + \theta(t))|) \rightarrow \sin(Q_a(\breve{\theta}(t))) \ . \tag{5.28}$$

The quantization grid of $Q_a(\cdot)$ and the clock data $\breve{\theta}(t)$ are explained below.

1. **Quantization grid:** An equidistant grid is set to quantize the absolute value of the sine wave. The quantization levels of the sine wave can be defined as

$$\bar{l}_s = \{0, q_a, 2q_a, \ldots, 1-2q_a, 1-q_a, 1\} , \tag{5.29}$$

where $q_a = 1/(L_a - 1)$ is the step size, and L_a is the number of levels in $\bar{l}_s$. Those equidistant quantization levels of amplitude can be translated into non-equidistant quantization levels of the quantization operator $Q_a(\cdot)$ in phase as

$$\bar{l}_a = \sin^{-1}(\bar{l}_s) . \tag{5.30}$$

The $\sin^{-1}$ operator is a non-unique mapping function. Since the input $\bar{l}_s$ is all positive, then for each input, $\bar{l}_a$ has two values from 0 to π. We will chose the value of $\bar{l}_a$ which lies in the range of $[\frac{\pi}{2}, \pi]$.

2. **Clock data:** From equation (5.25) we know that $\breve{\theta}_m$ lies in the range $[0, \pi]$. Therefore, in order to map it into the range $[\frac{\pi}{2}, \pi]$, we do the following conversion

$$\breve{\theta}(t) = |\breve{\theta}_m(t) - \frac{\pi}{2}| + \frac{\pi}{2} \in [\frac{\pi}{2}, \pi] . \tag{5.31}$$

This conversion ensures that $\sin(\breve{\theta}(t)) = \sin(\breve{\theta}_m(t))$. Additionally, this transformation simplifies the hardware design, as the range of $\breve{\theta}(t)$ is smaller than $\breve{\theta}_m$. Having a smaller range with fixed number of bits makes the step size smaller and thus the quantization resolution is enhanced by 1 bit.

The modified phase $\breve{\theta}(t)$ is then quantized using $Q_a(\cdot)$ to produce the data which drives the DAC clock which is defined as

$$\breve{d}_a(t) = Q_a(\breve{\theta}(t)) . \tag{5.32}$$

The way $\breve{d}_a(t)$ generates a clock signal will be explained later.

Phase quantization

In this method, the DAC output can be represented as

$$\hat{r}_{qp}(t) = \hat{r}_r(t)|\sin(Q_p(\omega_c t + \theta(t)))| , \tag{5.33}$$

where the quantization error of $Q_p(\cdot)$ is defined as

$$e_{qp}(t) = |\sin(Q_p(\omega_c t + \theta(t)))| - |\sin(\omega_c t + \theta(t))| . \tag{5.34}$$

In phase quantization, the quantization grid and clock data are defined as follows.

1. **Quantization grid:** We use the same phase signal $\check{\theta}(t)$ as in equation (5.31). However, unlike amplitude quantization, an equidistant grid is set to quantize the phase signal. The quantization levels can be defined as

$$\bar{l}_p \quad = \quad \{\pi/2, \pi/2 + q_p, \pi/2 + 2q_p, \ldots, \pi - 2q_p, \pi - q_p, \pi\} \; , \tag{5.35}$$

where $q_p = \pi/(2(L_p - 1))$ is the step size of the quantizer $Q_p(\cdot)$, and L_p is the number of levels in $\bar{l}_p$. This equidistant quantization grid in phase corresponds to a non-equidistant amplitude quantization grid

$$\bar{l}_k \quad = \quad \sin(\bar{l}_p) \; . \tag{5.36}$$

2. **Clock data:** The modified phase signal $\check{\theta}$ is used to generate the clock data defined as

$$\check{d}_p(t) \quad = \quad Q_p(\check{\theta}(t)) \; . \tag{5.37}$$

The difference to the amplitude quantization in equation (5.32) is that the quantizer $Q_p(\cdot)$ has equidistant quantization levels whereas $Q_a(\cdot)$ has non-equidistant quantization levels.

Block diagram

In this section, we explain how to implement both methods. Figure 5.15 shows how do amplitude quantization and phase quantization generate a data-dependent clock from $\check{\theta}$.

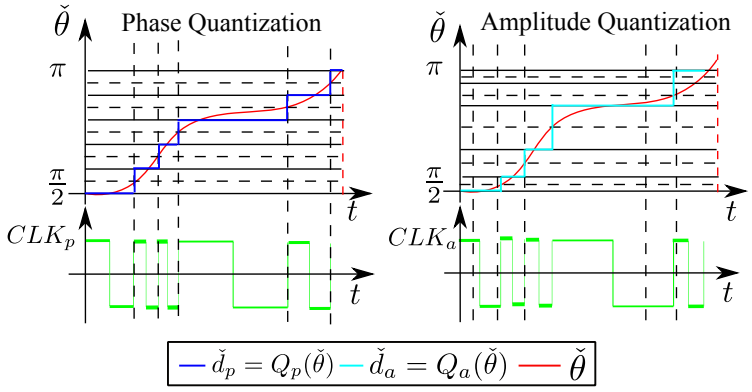

Figure 5.15: Data dependent clock

Figure 5.16 shows a possible block diagram for both methods. The difference lies in the quantizer, which is equidistant in case of phase quantization $Q_p(\cdot)$ and non-equidistant in case of amplitude quantization $Q_a(\cdot)$. In addition, the DAC is preloaded with the quantized levels of $\bar{l}_s$ and $\bar{l}_k$ for the amplitude and phase quantization, respectively. The preloaded levels are multiplied with the averaged radius to produce $\hat{r}_p(t)$. The "DD-CLK" is the data-dependent clock generation block which is responsible of generating the clock signal $CLK_{a/p}$ from the quantized data $Q_{a/p}(\breve{\theta})$ as shown in Figure 5.15.

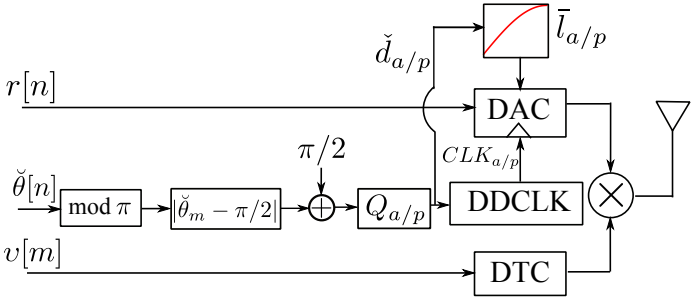

Figure 5.16: A polar transmitter with DAC oversampling

5.4.3. Reduction of out-of-band noise

In this section, we present a qualitative explanation of how the proposed methods can influence the out-of-band noise of the transmitted signal. Figure 5.17 shows an example of the amplitude quantization error $e_{qa}(t)$, the phase quantization error $e_{qp}(t)$, the cosine-approximation error $e_c(t)$ without DAC oversampling, and the exact signal $\cos(\omega_c t + \theta(t))$. It is clear that the overall noise energy is reduced when oversampling the DAC.

Harmonics

From figure 5.12, we see that the cos-approximation error is the main component of the out-of-band noise at the harmonics. Figure 5.17 shows that, when the DAC is oversampled, part of the phase information $|\cos(\omega_c t + \theta(t))|$ is moved to the DAC and therefore the cos-approximation error is reduced. Consequently the spectral level at the harmonics is reduced.

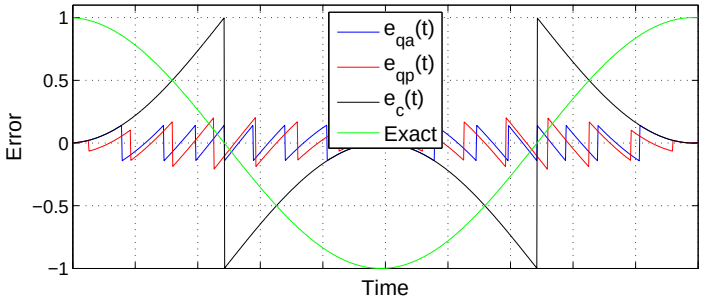

Figure 5.17: Amplitude error vs phase error

Noise floor

Previously, it was explained that the noise floor in the transmitted signal is caused by the discrete time grid of the DTC. The time quantization error signal $\bar{e}(t)$ is composed of rectangular pulses as explained in section 4.4.1. When the DAC is oversampled, we also obtain rectangular pulses at the instants when the DAC toggles from one level to another in $\bar{l}_s$ or $\bar{l}_k$. There are two main differences between the oversampled and non-oversampled cases. First, the rectangular pulses in the oversampled case occur more often during a single cycle than the non-oversampled case. Second, the amplitudes of the error pulses in the oversampled case are smaller than the non-oversampled case. Figure 5.18 shows the difference of time quantization for the cases when the DAC is oversampled and when it is not oversampled.

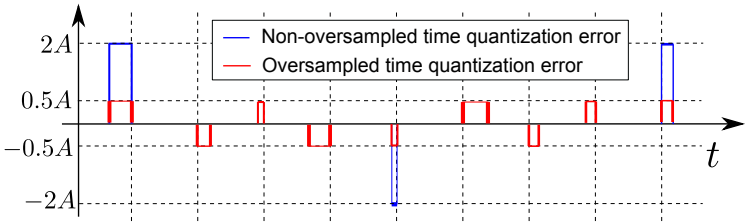

Figure 5.18: Time quantization error for oversampled and non-oversampled DAC

Considering equation (5.20), if we fix the sampling rate f_s, we see that the noise floor is proportional to the rate of error pulses which is proportional to the carrier frequency. However, the noise floor is proportional to the square of the amplitude A^2 of the pulses.

This implies, that reducing the amplitude of the error pulses is more effective than reducing the rate of pulses. In figure 5.18, the oversampling factor is $N_{OS} = 4$. By oversampling the DAC, we increase the rate of the error pulses by the oversampling factor N_{OS} (from 2 error pulses per period to 8 error pulses per period) but we also reduce the amplitudes of the error pulses by N_{OS} (from an amplitude of $2A$ to $0.5A$). Therefore, the net effect of oversampling the DAC is the reduction of the noise floor by an approximate factor of N_{OS}/N_{OS}^2.

5.4.4. Results

In this section, the effect of the DAC oversampling method on the out-of-band noise spectrum using simulations is investigated. The oversampling rate N_{OS} is defined as the number of steps within a period of the transmitted signal. The quantizer in figure 5.16 is responsible of generating different levels within a quarter of a wave cycle $\breve{\theta} \in [\pi/2, \pi]$, which are L_a levels in case of amplitude quantization and L_p levels in case of phase quantization. Consequently, the oversampling rate can be defined as

$$N_{OS} = 4 \cdot L_{a,p} \ . \tag{5.38}$$

b_{os} is defined as the number of bits used to set the quantization levels of the quantizer in figure 5.16, i.e $L_{a,p} = 2^{b_{os}}$. Therefore, the oversampling rate can also be written as

$$N_{OS} = 2^{b_{os}+2} \ . \tag{5.39}$$

- **Amplitude quantization vs phase quantization**

  The spectrum of the transmitted signal will be simulated using different number of bits b_{os} for amplitude and phase quantization. In both cases, a baseband signal is generated with bandwidth of $f_b = 20\text{MHz}$, a carrier frequency of $f_c = 1\text{GHz}$, and a sampling rate of $f_s = 1\text{THz}$. As b_{os} increases, we get closer to the theoretical signal and therefore the out-of-band noise is reduced. Figure 5.19 shows the spectrum when using amplitude quantization. As expected, the out-of-band noise is reduced as we increase b_{os}. However, we notice that even though the spectral level of the harmonics are damped, their presence is still significant and might violate the spectral mask.

  Figure 5.20 shows the spectrum for the phase quantization case. From figure 5.20 we can state the following facts. First, the harmonics are shifted to higher frequency components starting from $6f_c$ for $b_{os} = 2$. Harmonics at such high frequencies can be disregarded as the antenna of the transmitter acts as a low

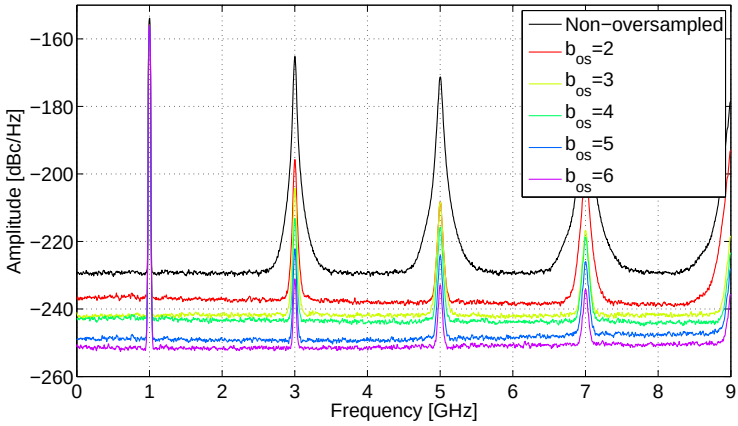

Figure 5.19: Spectrum when using amplitude quantization

pass filter which has a cut-off frequency less than $6f_c$. Second, when comparing the noise floor of the phase quantization case with amplitude quantization, we notice that the phase quantization has a slightly lower floor for $b_{os} = 6$. It is also observable that the noise floor in figure 5.20 tends to rise as the frequency increases. However, for our application we are not interested in high frequency components as the antenna will filter out those components.

- **Attenuation vs number of bits**

It was previously explained that in order to reduce the noise floor, the sampling rate f_s should be increased. However, when fixing the sampling rate f_s and increasing the oversampling bits b_{os}, we can reduce the noise floor as shown in figure 5.19 and 5.20. In this section, we investigate the trade-off between the oversampling rate of the DAC and the sampling frequency of DTC with respect to the attenuation of the noise floor. The attenuation of the noise floor is defined as the difference in dB between the in-band spectral level at f_c and the average of the spectrum starting from $f_c + f_b/2$ till $2f_c$. In all cases, phase quantization is considered instead of amplitude quantization.

Figure 5.21 shows the out-of-band noise attenuation for different number of bits with different sampling rates f_s. Figure 5.22 shows the results when the sampling rate is fixed at $f_s = 1$THz and the baseband signal bandwidth f_b changes. As shown, the higher the bandwidth is, the less the attenuation would be.

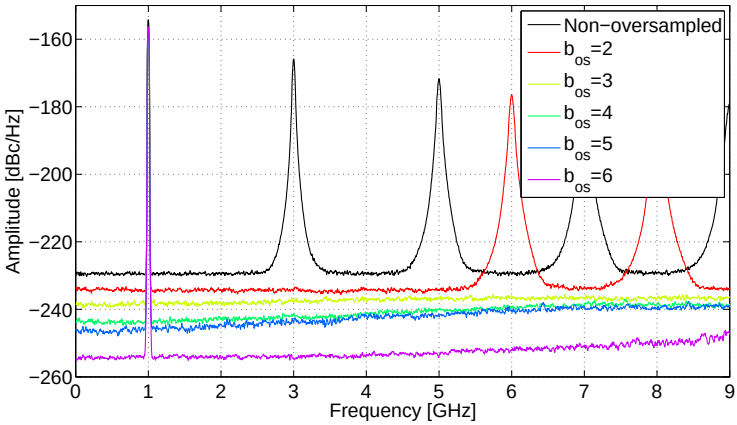

Figure 5.20: Spectrum when using phase quantization

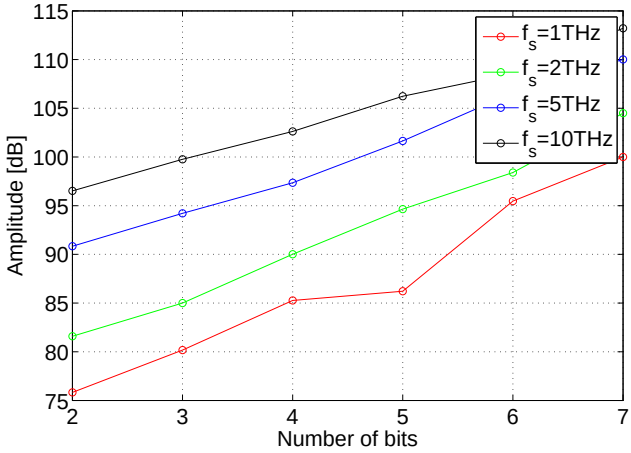

Figure 5.21: Out-of-band noise attenuation vs oversampling of DAC for different sampling frequencies of DAC

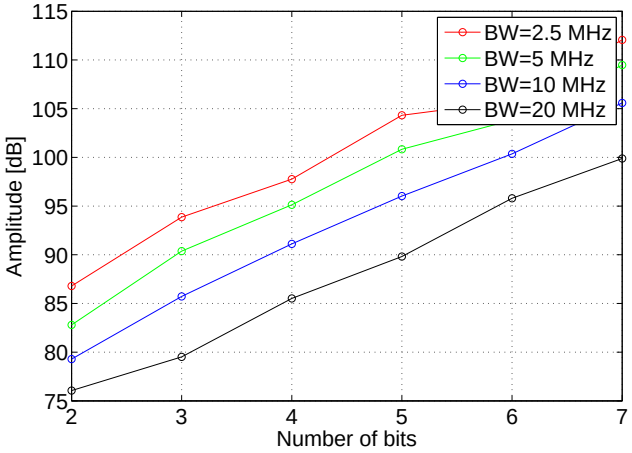

Figure 5.22: Out-of-band noise attenuation vs oversampling of DAC for different base-band bandwidths

Oversampling rate vs normalized sampling rate

We know from the previous chapter that increasing the sampling rate will reduce the out-of-band noise. In this chapter, we showed that increasing the oversampling rate also reduces the out-of-band noise. Now, we try to investigate the trade-off between those two aspects. For a fixed required out-of-band noise attenuation, we can have different combinations of DAC oversampling N_{OS} and sampling rate f_s.

We investigate the required sampling rate to achieve CNR = 78 and 92 dB. Those attenuations are chosen as they correspond to the sampling rates of f_s = 1 and 5 THz, respectively (according to equation (4.44)). In figure 5.23, the oversampling rate N_{OS} vs the normalized sampling rate is shown. The normalized sampling rate is defined as the ratio between the sampling rate when applying DAC oversampling and the sampling rate without applying DAC oversampling which will both yield the same out-of-band noise attenuation. It can be seen from figure 5.23 that increasing the oversampling rate reduces the normalized sampling rate which makes the DTC more efficient.

Oversampling rate vs effective sampling rate

In this section, the effect of the oversampling rate on the effective frequency f_{eff} will be investigated. The effective frequency is the sampling rate for the non-oversampled

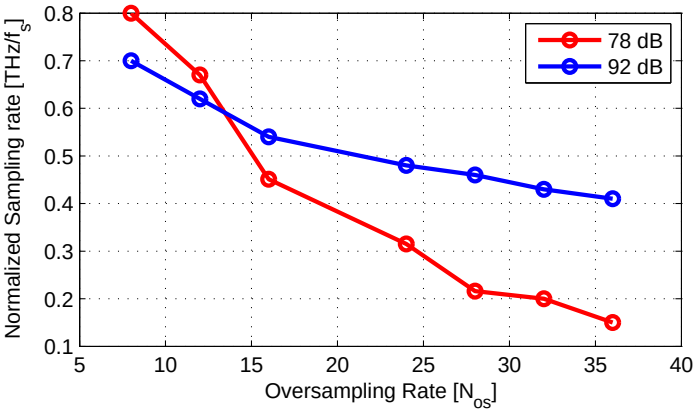

Figure 5.23: N_{OS} vs normalized sampling rate f_s for 78 dB and 92 dB attenuation

signal which will give the same CNR ratio as the oversampled case.

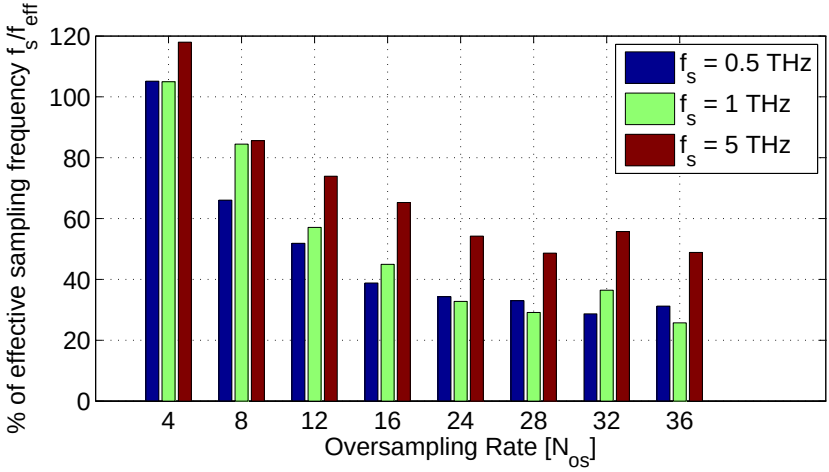

Figure 5.24: Efficiency of oversampling N_{OS} for different sampling rates $f_s = 0.5, 1, 5$ THz

Figure 5.24 shows the oversampling rate versus the percentage of the effective sampling frequency for 3 different sampling rates f_s = 0.5,1 and 5 THz. In order to

$f_s/1THz$ \ N_{OS}	4	8	12	16	24	28	32	36
0.5	0.476	0.757	0.965	1.288	1.458	1.517	1.745	1.601
1	0.952	1.184	1.751	2.224	3.052	3.432	2.745	3.887
5	4.239	5.842	6.766	7.658	9.223	10.278	8.970	10.233

Table 5.1.: Efficiency of oversampling N_{OS} for different sampling rates $f_s = 0.5, 1, 5$ THz.

understand the graph, consider the case of $N_{OS} = 16$ and $f_s = 0.5$THz. The percentage of sampling frequency is around 40%, this means that the sampling rate $f_s = 0.5$THz with oversampling $N_{OS} = 16$ corresponds to the effective sampling rate $f_{eff} = 0.5/0.4$ THz $= 1.25$THz without DAC oversampling. One can see that an oversampling rate $N_{OS} = 4$ leads to an increased percentage which means that oversampling is not actually effective. The larger the oversampling rate, the less the percentage. However, it is observed that the larger the sampling rates (5THz), the less effective the oversampling becomes.

Table 5.1 shows more concrete numbers of the effective sampling rate. For example, an oversampling rate $N_{OS} = 28$ with $f_s = 1$THz corresponds to an effective sampling rate of $f_{eff} = 3.43$THz.

6. Feedforward noise shaping

The polar transmitter analyzed in this thesis has the advantage of being intensely *digital*. The signals incorporated in the polar transmitter are thus discrete in time and amplitude. The quantization of the amplitude introduces quantization noise. This noise tends to have a flat spectrum. Hence, if the quantization noise becomes larger than a certain threshold, it might violate the spectral mask.

For long time, feedback noise shaping circuits have been used in order to *shape* the quantization noise spectrum by moving the noise frequency components from critical regions to other frequency bands. As much as those circuits tend to be cheap and easy to implement, they also suffer from instability, high out-of-band noise and difficulty to adapt to different spectrum shaping requirements.

In this chapter, we introduce a novel approach for shaping the quantization noise, by adding small corrections to the quantized signal in order to have frequency notches in the noise shaped signal. The proposed approach provides a feedforward adaptable architecture which can control the notch width, notch depth, and can have multiple notches while keeping the out-of-band noise level low compared to feedback structures. It is worth noting that the approach presented in this chapter is not restricted to polar transmitters, but is also applicable for traditional IQ transmitters. The concept of the approach was presented in Ibrahim and A. [2014b].

This chapter is organized as follows. First a brief overview about the basics of noise shaping will be presented. Then, we introduce the basic principle of feedforward noise shaping. Second, an extended version of the feedforward noise shaping approach will then be presented. Afterwards, the application of the proposed noise shaping approach in transmitters will be explained. Finally, a comparison of the results with the state-of-the-art feedback noise shaping algorithm will be demonstrated.

6.1. Quantization noise shaping basics

6.1.1. Quantization basics

Quantization refers to the mapping of a signal from a high-precision domain to a low-precision domain. The quantization operation can also be modeled as adding an error signal $\check{e}[n]$ to the high precision signal $x[n]$ to get the low precision signal $x_q[n]$

$$x_q[n] \quad = \quad \mathbf{Q}(x[n]) = x[n] + \check{e}[n] \ , \tag{6.1}$$

where $\mathbf{Q}(\cdot)$ is the quantization operation.

The quantization error $\check{e}[n]$ is assumed to have the following properties:

1. $\check{e}[n]$ is a random signal which is uniformly distributed in $[-0.5q_o, 0.5q_o)$, where q_o is the Least Significant Bit (LSB).
2. $\check{e}[n]$ has zero mean $\mathbf{E}(\check{e}[n]) = 0$ and variance $\mathbf{Var}(\check{e}[n]) = \sigma_{\check{e}}^2 = q_o^2/12$.
3. The spectrum of $\check{e}[n]$ is white with $R_{\check{e}\check{e}}(\omega) = \sigma_{\check{e}}^2$.

6.1.2. Feedback noise shaping

Since decades, delta-sigma noise shaping circuits have been used. The quantization noise $\check{e}[n]$ is extracted from the quantizer, filtered using $H_{FB}(\omega)$, and then added to $x[n]$ as shown in figure 6.1.

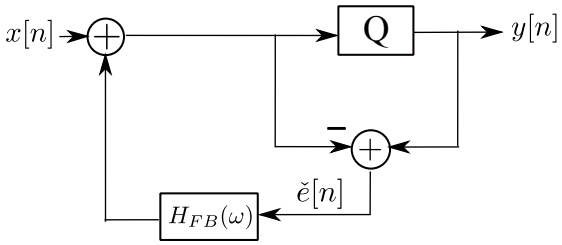

Figure 6.1: Traditional feedback noise shaping

The noise shaping filter $H_{FB}(\omega)$ does not have a zero-order term and has at least one delay element. The output of the feedback noise shaping circuit can be denoted as

$$y[n] \quad = \quad x[n] + (1 + h_{FB}[n]) * \check{e}[n] \ . \tag{6.2}$$

The Fourier Transform of $y[n]$ can be represented as

$$Y(\omega) \quad = \quad X(\omega) + (1 + H_{FB}(\omega))\check{E}(\omega) \ . \tag{6.3}$$

The filtered quantization error can be denoted as

$$\tilde{e}_{FB}[n] \quad = \quad (1 + h_{FB}[n]) * \check{e}[n] \ . \tag{6.4}$$

By tuning the filter coefficients of $H_{FB}(\omega)$, the spectrum of the quantization error can be shaped. The PSD of the filtered noise can be represented as

$$R_{\tilde{e}_{FB}\tilde{e}_{FB}}(\omega) \quad = \quad |1 + H_{FB}(\omega)|^2 R_{\check{e}\check{e}}(\omega) = \sigma_{\check{e}}^2 |1 + H_{FB}(\omega)|^2 \ . \tag{6.5}$$

The total noise power of $\tilde{e}_{FB}[n]$ is

$$\sigma_{\tilde{e}_{FB}}^2 = \mathbf{E}(\tilde{e}_{FB}[n]^2) = \int_{-\pi}^{\pi} R_{\tilde{e}_{FB}\tilde{e}_{FB}}(\omega) \frac{\mathrm{d}\omega}{2\pi} = \sigma_{\check{e}}^2 \int_{-\pi}^{\pi} |1 + H_{FB}(\omega)|^2 \frac{\mathrm{d}\omega}{2\pi} \ . \tag{6.6}$$

FIR notch feedback filter

Assume we would like to have a notch in the spectrum of the shaped signal at a frequency ω_o. The filter $H_{FB}(\omega)$ can be tuned in order to have a second order FIR notch filter so that

$$1 + H_{FB}(\omega) \quad = \quad 1 - 2\cos(\omega_o)e^{-j\omega} + e^{-j2\omega} \tag{6.7}$$

$$\quad = \quad e^{-j\omega} 2(\cos(\omega) - \cos(\omega_o)) \ . \tag{6.8}$$

The total noise power becomes

$$\sigma_{\tilde{e}_{FB}}^2 \quad = \quad \sigma_{\check{e}}^2 \int_{-\pi}^{\pi} |1 + H_{FB}(\omega)|^2 \frac{\mathrm{d}\omega}{2\pi} \tag{6.9}$$

$$\quad = \quad 4\sigma_{\check{e}}^2 \int_{-\pi}^{\pi} (\cos(\omega)^2 + \cos(\omega_o)^2 - 2\cos(\omega)\cos(\omega_o)) \frac{\mathrm{d}\omega}{2\pi} \tag{6.10}$$

$$\quad = \quad (2 + 4\cos(\omega_o)^2)\sigma_{\check{e}}^2 \geq 2\sigma_{\check{e}}^2 \ . \tag{6.11}$$

This means that a second order notch filter more than doubles the total noise power in order to have a notch at a frequency ω_o.

Theoretically, it is possible to use an IIR notch filter in the feedback loop

$$1 + H_{FB}(\omega) \quad = \quad \frac{1 - 2\cos(\omega_o)e^{-j\omega} + e^{-j2\omega}}{1 - 2r_{notch}\cos(\omega_o)e^{-j\omega} + r_{notch}^2 e^{-j2\omega}} \ , \tag{6.12}$$

where r_{notch} is a factor to control the notch width. However, placing IIR filters in the feedback is rarely done because it is relatively unstable compared to FIR filters, specially when considering the RF sampling rates in this thesis.

In spite that feedback noise shaping filters have been used for decades, they possess some disadvantages which can be listed as follows:

- The spectral level of the error spectrum $|1 + H_{FB}(\omega)|^2\sigma_e^2$ outside the notch frequency is high which might violate the spectral mask.
- The feedback structure might be unstable due to limit cycles [Gersho and Gray, 1992].
- The coefficients of the filter $H_{FB}(\omega)$ as well as the filter output are quantized as well. This introduces additional noise into the shaped signal. In our proposed approach in section 6.2, we also have quantization distortion. However, our approach is more robust to quantization noise.

6.2. Feedforward approach

6.2.1. Basic idea

The principle of feedforward noise shaping is adding a small correction signal $c[n]$ to the quantized signal $x_q[n] = x[n] + \check{e}[n]$ as shown in figure 6.2. The criterion of choosing the correction signal $c[n]$ is based on a frequency monitoring block. This block monitors the Fourier transform of the corrected quantization error at a given notch frequency ω_o at a given time instant n. The correction signal $c[n]$ is chosen such that it cancels the frequency component at ω_o.

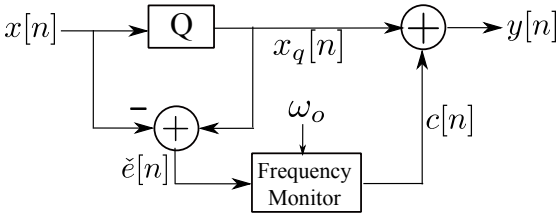

Figure 6.2: Principle of feedforward noise shaping

The quantized signal after noise shaping is

$$y[n] = x_q[n] + c[n] = x[n] + \check{e}[n] + c[n] \; . \tag{6.13}$$

The correction signal $c[n]$ is only allowed to be an integer multiple of the Least Significant Bit (LSB) of the low precision word-length

$$c[n] \quad = \quad i \cdot q_o, \quad i \in \{.., -2, -1, 0, 1, 2, ..\} \; , \tag{6.14}$$

where q_o corresponds to the LSB. In the simplest case, $c[n]$ can only be 0 or $\pm q_o$.

The shaped quantization error is

$$\tilde{e}[n] \quad = \quad \check{e}[n] + c[n] \; . \tag{6.15}$$

The choice of the correction signal $c[n]$ is such to minimize the amplitude of the Fourier transform

$$\tilde{E}(\omega_o) \quad = \quad \sum_n \tilde{e}[n] e^{-j\omega_o n} = \sum_n (\check{e}[n] + c[n]) e^{-j\omega_o n} \tag{6.16}$$

of $\tilde{e}[n]$ at ω_o. At the same time, the correction signal $c[n]$ should have the lowest possible energy in order to minimize the out-of-band noise after the noise shaping.

6.2.2. Correction signal

The frequency monitoring block in figure 6.2 should be able to update the frequency component $\tilde{E}(\omega_o)$ on a sample-by-sample basis. In order to do this, we calculate the Discrete-Time Fourier Transform (DTFT) in equation (6.16) at time n in a recursive way:

$$\tilde{E}_n(\omega_o) \quad = \quad \tilde{E}_{n-1}(\omega_o) + (\check{e}[n] + c[n])e^{-j\omega_o n} \ . \tag{6.17}$$

Given ω_o, $\tilde{E}_{n-1}(\omega_o)$, and $\check{e}[n]$, the exact value of $c[n]$ to force $\tilde{E}_n(\omega_o) = 0$ is

$$c[n] \quad = \quad -\tilde{E}_{n-1}(\omega_o)e^{j\omega_o n} - \check{e}[n] \ . \tag{6.18}$$

However, the choice of the correction signal is subject to the following restrictions:

1. Equation (6.18) might yield a complex value for $c[n]$. However, $c[n]$ is limited to real values.
2. $c[n]$ is subject to equation (6.14). This means, the correction value is itself quantized and can have only discrete possible values. This quantization yields a non-zero residual DTFT $\tilde{E}_n(\omega_o)$ in equation (6.17) which has to be considered during the correction at the next time instant $n + 1$.

Consequently, the correction signal becomes

$$c[n] \quad = \quad \mathbf{Q}\left(\Re\{-\tilde{E}_{n-1}(\omega_o)e^{j\omega_o n} - \check{e}[n]\}\right) \ , \tag{6.19}$$

where $\Re\{\cdot\}$ denotes the real part of a complex number and $\mathbf{Q}(\cdot)$ denotes the quantization operation due to the limitation of equation (6.14). Figure 6.3 visualizes the process of calculating the correction value in the complex plane.

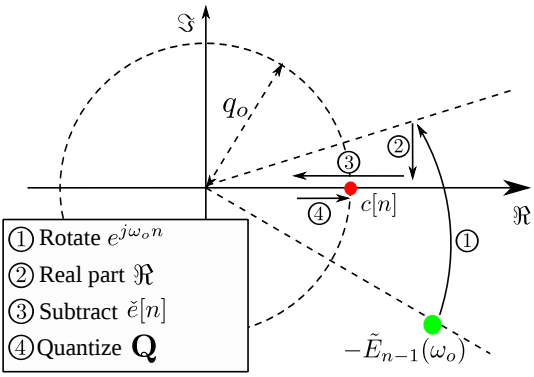

Figure 6.3: Computing the correction $c[n]$ in the complex plane

6.2.3. Basic algorithm

The basic algorithm of the feedforward noise shaping can be summarized as below:

Input: $\check{e}[n] = \mathbf{Q}(x[n]) - x[n], n = 0, 1, ..$
Output: $c[n] = i \cdot q_o$ with $i \in \{0, \pm 1, \pm 2, ..\}$
$y[n] = \mathbf{Q}(x[n]) + c[n]$
Parameter: ω_o
Initialization: $\tilde{E}_{-1}(\omega_o) = 0$
for $n = 0, 1, 2, ..$ **do**
$z = \Re(-\tilde{E}_{n-1}(\omega_o)e^{j\omega_o n} - \check{e}[n])$
$c[n] = \mathbf{Q}(z)$
$\tilde{E}_n(\omega_o) = \tilde{E}_{n-1}(\omega_o) + (\check{e}[n] + c[n])e^{-j\omega_o n}$
end

Algorithm 1: Basic feedforward noise shaping algorithm

6.2.4. Single notch circuit

In figure 6.4 a possible circuit implementation of the feedforward noise shaping approach is shown.

The **F** block in figure 6.4 updates the frequency bin on a sample per sample basis. A possible implementation of **F** is shown in figure 6.5. The **C** block shown is a complex number combiner which takes 2 numbers corresponding to real and imaginary parts and outputs the complex number. The $\cos(\omega_o n)$ and $\sin(\omega_o n)$ are discrete-time oscillators

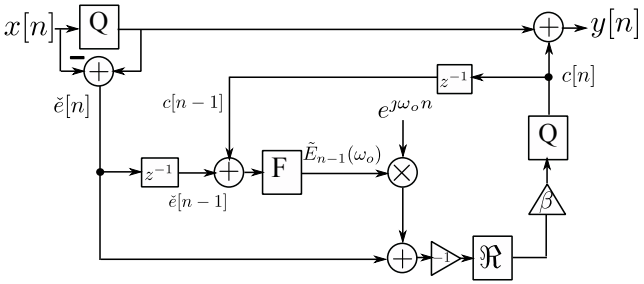

Figure 6.4: Circuit for single notch feedforward noise shaping

with frequency f_o and sampling frequency f_s. The factors β and λ will be explained later.

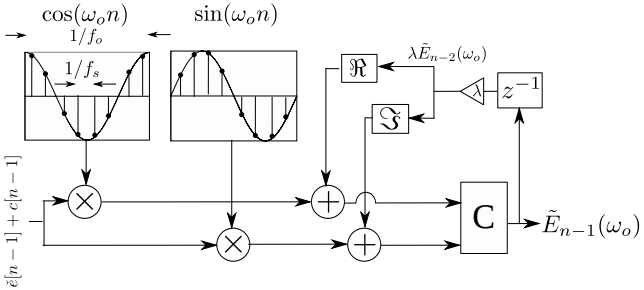

Figure 6.5: Circuit for updating the Fourier transform

6.3. An extended feedforward noise shaping algorithm

In the previous section, the basic algorithm for feedforward noise shaping was presented. In this section, we extend the algorithm to a more general one which has better control over the spectrum of the noise shaped signal.

6.3.1. Out-of-band noise reduction

One of the important criteria in evaluating the noise shaping algorithm is the level of the out-of-band noise. In order to minimize the out-of-band noise, we limit the maximum amplitude of the correction signal $c[n]$ to one LSB q_o. This means, the output of $\mathbf{Q}$ in equation (6.19) is either 0 or $\pm q_o$.

6.3.2. Notch width

Since the received downlink signal can have different bandwidths (for example WLAN has a larger bandwidth than Bluetooth), it would be useful to have an easy method to control the width of the notch. In the traditional feedback noise shaping, the width of the notch is fixed, and the only way to change the width of the notch is by changing the filter length and coefficients.

In the proposed approach, the width of the notch can be controlled by changing the frequency of corrections, i.e. how often $c[n] \neq 0$. We will see later in simulations that the more often the corrections, the larger the notch width. We can control the frequency of corrections by scaling the exact correction value in equation (6.19) by a notch width factor $0 < \beta \leq 1$. The correction signal then becomes

$$c[n] \quad = \quad \mathbf{Q}(\beta \cdot \Re(-\tilde{E}_{n-1}(\omega_o)e^{j\omega_o n} - \check{e}[n])) \; . \tag{6.20}$$

The smaller β becomes, the smaller the value inside $\mathbf{Q}(\cdot)$ and the larger the probability to get $c[n] = 0$. This implies less often the corrections. Tuning β to control the notch width is much easier than calculating new filter coefficients as in feedback noise shapers. Using this approach, the out-of-band noise level falls when the notch width is reduced.

6.3.3. Multiple notches

The downlink in a communication link might operate on multiple frequencies. For example, a transceiver might be receiving a voice call, WLAN , Bluetooth, GPS at

different frequencies. This implies that our noise shaping algorithm should be able to have multiple notches at different frequencies. We extend our basic noise shaping algorithm for one notch to multiple notches ω_i by tracking the Fourier transform of the shaped noise $\tilde{e}[n] = \check{e}[n] + c[n]$ at these frequencies

$$\tilde{E}_n(\omega_i) \quad = \quad \tilde{E}_{n-1}(\omega_i) + (\check{e}[n] + c[n])e^{-\jmath\omega_i n} \ . \tag{6.21}$$

In order to eliminate $\tilde{E}_n(\omega_i)$, $c[n]$ has to satisfy

$$c[n] \quad = \quad -\tilde{E}_{n-1}(\omega_i)e^{\jmath\omega_i n} - \check{e}[n] \tag{6.22}$$

for all notch frequencies ω_i, which is generally difficult to achieve. Thus we propose to choose $c[n] \in \{0, \pm q_o\}$ such to shape the largest frequency component amplitude $|E_n(\omega_{i_o})|$ with

$$\begin{aligned} i_o \quad &= \quad \arg\max_i(\beta_i|\Re(-\tilde{E}_{n-1}(\omega_i)e^{\jmath\omega_i n} - \check{e}[n])|), \quad 0 < \beta_i \leq 1 \ , \\ c[n] \quad &= \quad \mathbf{Q}(\beta_{i_o}\Re(-\tilde{E}_{n-1}(\omega_{i_o})e^{\jmath\omega_{i_o}} - \check{e}[n])) \ . \end{aligned} \tag{6.23}$$

The notch width factors β_i can be identical or different for different ω_i. This enables an individual control of the notch width and therefore, different notch widths.

6.3.4. Notch depth

The SNR of the downlink is known to vary in time and space for any communication link. Sometimes, the downlink at ω_o has a low SNR. Then, we need to cancel the frequency bin $E(\omega_o)$ as much as possible, which in turn introduces much out-of-band noise. In other situations, the SNR is high and the notch does not need to be so deep, which results in a smaller out-of-band noise. Controlling the depth of the notch is thus a useful option in communication applications.

In the proposed approach, we can control the notch depth by simply tuning a second scaling factor $0 \leq \lambda_i \leq 1$, which corresponds to the notch frequency ω_i. The factors λ_i are used in the recursive calculation of the frequency components

$$\tilde{E}_n(\omega_i) \quad = \quad \lambda_i\tilde{E}_{n-1}(\omega_i) + (\check{e}[n] + c[n])e^{-\jmath\omega_i n} \ . \tag{6.24}$$

By choosing $0 < \lambda_i < 1$, the correction value $c[n]$ cancels only a portion of the frequency component at ω_i. Therefore, a residual frequency component $(1 - \lambda_i)E_{n-1}(\omega_i)$ remains. Thus the choice of λ_i controls the notch depth at ω_i.

Since each notch frequency ω_i has its own notch depth factor λ_i, different notches can have different depths. This is particularly useful when one of the receiving signals has

a better SNR than the other. For example, WLAN signals tend to have higher SNR than GPS signals. Therefore, a lower notch depth factor can be assigned to the WLAN frequency $\lambda_{WLAN} < \lambda_{GPS}$.

6.3.5. Extended algorithm

Below the extended feedforward noise shaping algorithm is summarized for multiple notches with an improved control of the spectrum of the noise shaped signal. ω_i are the notch frequencies. β_i are the notch width factors, and λ_i are the notch depth factors. The operator $\mathbf{Q}(\cdot)$ denotes the quantization to yield an output either 0 or $\pm q_o$.

Input: $\check{e}[n] = \mathbf{Q}(x[n]) - x[n], n = 0, 1, ..$
Output: $c[n] = i \cdot q_o$ with $i \in \{0, \pm 1\}$
$y[n] = \mathbf{Q}(x[n]) + c[n]$
Parameters: $\omega_i, \beta_i, \lambda_i$
Initialization: $\tilde{E}_{-1}(\omega_i) = 0 \quad \forall \omega_i$ **for** $n = 0, 1, 2, ..$ **do**
$z_i = \beta_i \cdot \Re(-\tilde{E}_{n-1} \cdot e^{j\omega_i n} - \check{e}[n]) \quad \forall \omega_i$
$i_o = \arg\max |z_i|$
$c[n] = \mathbf{Q}(z_{i_0})$
$\tilde{E}_n(\omega_i) = \lambda_i \tilde{E}_{n-1}(\omega_i) + (\check{e}[n] + c[n]) e^{-j\omega_i n} \quad \forall \omega_i$
end

Algorithm 2: Extended noise shaping feedforward algorithm

6.3.6. Extended circuit

Figure 6.6 shows a proposed circuit which includes the extended algorithm's features described previously. The blocks $\mathbf{B}_{\omega_o}$ and $\mathbf{B}_{\omega_1}$ are the single notch circuits shown in figure 6.4. The *COMP* block denotes a comparator which chooses which frequency to cancel according to its amplitude.

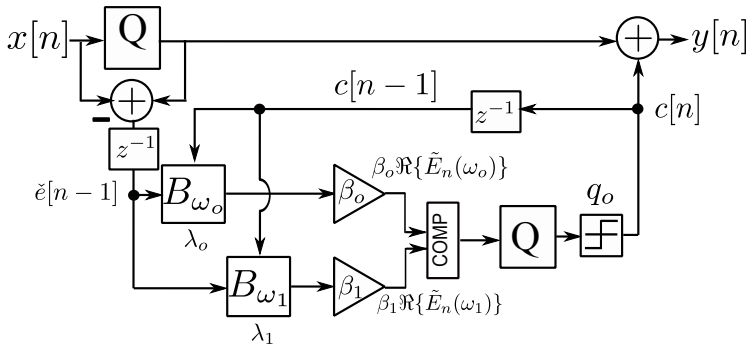

Figure 6.6: Extended feedforward noise shaping circuit comprising all feedforward noise shaping options

6.4. Results

In this section, the results of the feedforward noise shaping approach are presented. Any noise shaping approach used for word-length reduction will increase the total noise energy of the shaped signal $y[n]$. In order to compare different noise shaping algorithms, we need to define a certain metric in order to evaluate the performance of each algorithm. In the following section, we define the Signal-to-Quantization-Noise-Ratio (SQNR) to evaluate the noise shaping algorithms of different approaches.

6.4.1. Signal-to-Quantization-Noise Ratio γ

Recall that the high-precision signal is denoted as $x[n]$ and the noise-shaped low-precision signal is denoted as $y[n]$. The SQNR is defined as

$$\gamma[dB] \quad = \quad 10\log_{10}\left(\frac{\sum_{n=0}^{k-1}(y[n])^2}{\sum_{n=0}^{k-1}(y[n]-x[n])^2}\right). \tag{6.25}$$

The SQNR is defined as

γ_o : SQNR without noise shaping, i.e. $y[n] = \mathbf{Q}(x[n])$.

γ_b : SQNR of feedback noise shaping, see figure 6.1.

γ_f : SQNR of feedforward noise shaping, see figure 6.2.

6.4.2. Comparison benchmark

For the sake of comparison, the second order feedback notch filter FIR(2) is shown as a benchmark, which can be represented as

$$1 + \tilde{H}_{FB}(\omega) \quad = \quad 1 - 2\cos(\omega_o)e^{-j\omega} + e^{-j2\omega} \ . \tag{6.26}$$

The FIR(2) has the advantage of having the lowest possible total noise energy as indicated in equation (6.11). For higher order FIR filters, the SQNR will fall significantly. This can be explained by considering the number of extra terms present in the filter's transfer function. For example, FIR(2) has 2 filtering terms $-2\cos(\omega_o)$ and 1. The larger the filter order, the more filtering terms in the transfer function, hence, the larger the total quantization noise will be. Consequently, FIR(2) has the largest SQNR.

6.4.3. Simulations

In this section, the simulation results which evaluate the feedforward noise shaping approach are shown. 1000 complex 64-QAM baseband symbols are generated. The symbols are filtered using a raised cosine pulse shaping filter with the roll-off factor of 0.1. We assume a normalized sampling rate of $f_s = 1$ and a baseband bandwidth of 0.08 with an oversampling factor of 32 which yields $32,000$ samples. We consider the case when we truncate the word-length from $n_h = 10$ or $n_h = 7$ bits to $n_l = 5$ bits.

Single notch

In figure 6.7, the PSD of the high precision signal $x[n]$, the quantized signal $\mathbf{Q}(x[n])$, the feedback noise-shaped signal, and the feedforward noise-shaped signal are plotted, with $n_h = 10$ and $n_l = 5$ bits. The notch frequency is $f_o = 0.15$Hz. Figure 6.7 shows that for high frequency components, the PSD of the feedforward approach has around 4dB lower spectral level. The SQNR for no noise shaping, feedback noise shaping, and feedforward noise shaping are $\gamma_o = 22.55$, $\gamma_b = 16.59$, and $\gamma_f = 18.36$, respectively.

In figure 6.8, we plot the PSD as in figure 6.7 except for having $n_l = 7$ bits instead of 10 bits. This yields $\gamma_f = 19.19$dB and $\gamma_b = 17.44dB$. As shown, the spectrum of the noise-shaped signal using feedback noise shaping does not have a deep notch as the feedforward noise-shaped signal.

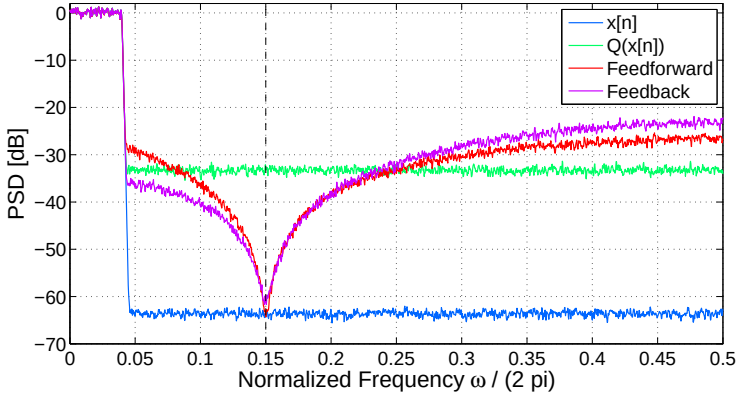

Figure 6.7: PSD of original signal, quantized signal with $n_h = 10$, $n_l = 5$, and shaped quantization noise with $f_o = 0.15$

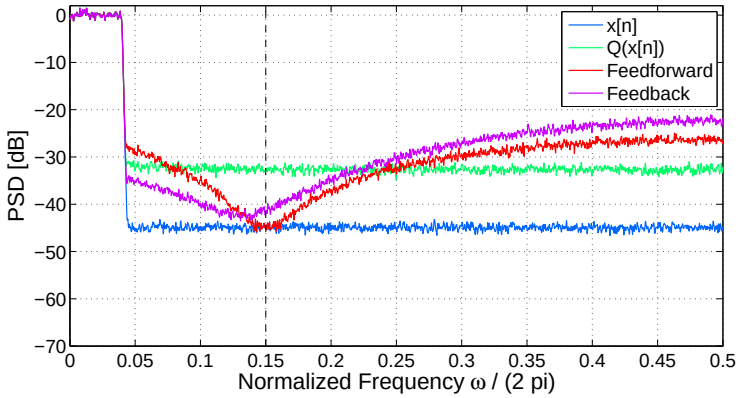

Figure 6.8: PSD of original signal, quantized signal with $n_h = 7$, $n_l = 5$, and shaped quantization noise with $f_o = 0.15$

SQNR vs notch frequency

In the previous simulation, we compared the performance of feedback and feedforward noise shaping for $f_o = 0.15$Hz. In order to have a fair comparison, we simulate the SQNR for all notch frequencies $f_o = [0 : 0.5]$ for $n_h = 10$ and $n_l = 5$. Figure 6.9 shows the SQNR versus all notch frequencies for feedback and feedforward noise shaping.

It can be concluded that the feedforward noise shaping approach maintains a more or less fixed SQNR for all notch frequencies, whereas the feedback noise shaping approach has variable SQNR, for which all SQNR values are always lower than the feedback approach except for $f_o = 0.25$. The shape of the feedback curve is directly related to equation (6.11).

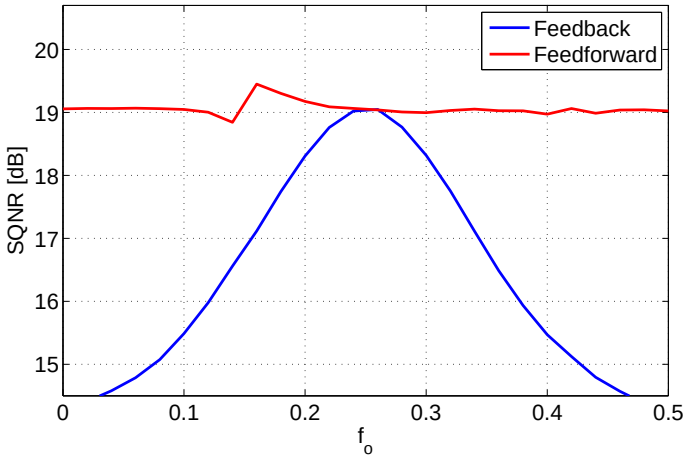

Figure 6.9: SQNR vs notch frequency f_o for feedback and feedforward noise shaping when quantizing from $n_h = 10$ bits to $n_l = 5$ bits

Double notch

In figure 6.10, the result for having 2 notches at $f_o = 0.1$ and $f_1 = 0.15$ is shown for the case of quantizing from $n_h = 10$ to $n_l = 5$. The simulation yields $\gamma_f = 15.55$dB and $\gamma_b = 8.21$dB. It can be seen that the feedforward noise-shaped signal has a narrower bandwidth of attenuation. This property is desirable in communication applications since the spectral mask tends to have narrow width notches rather than wide notches.

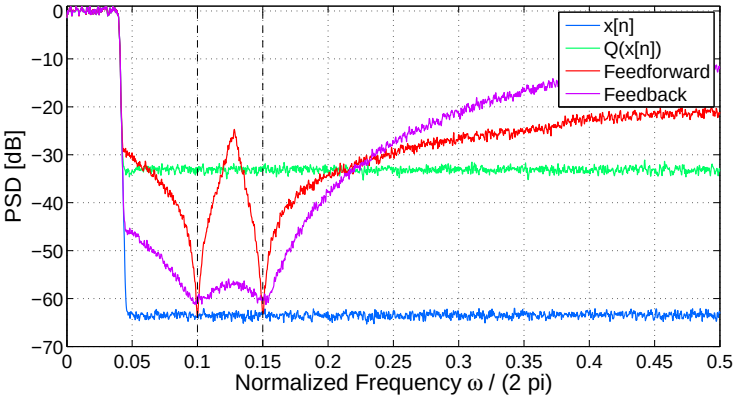

Figure 6.10: PSD of original signal, quantized signal with $n_h = 10$, $n_l = 5$, and shaped quantization noise with 2 notches $f_o = 0.1$ and $f_1 = 0.15$

Figure 6.11 shows the case of quantizing from $n_h = 7$ to $n_l = 5$. This simulation yields $\gamma_f = 15.265$dB and $\gamma_b = 8.21$dB.

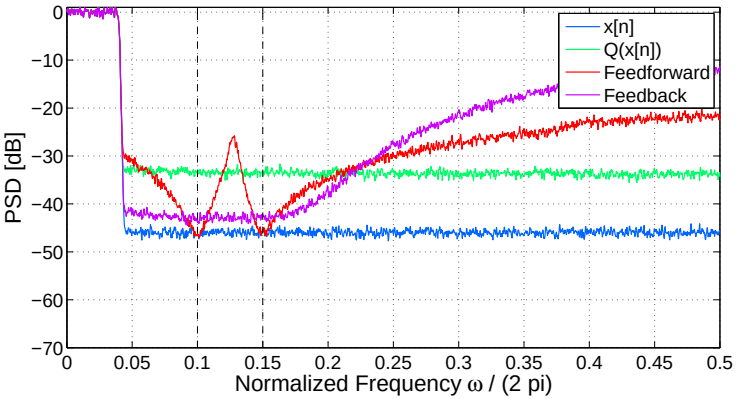

Figure 6.11: PSD of original signal, quantized signal with $n_h = 7$, $n_l = 5$, and shaped quantization noise with 2 notches $f_o = 0.1$ and $f_1 = 0.15$

Weighted double notch

As mentioned earlier, it is sometimes desirable to have different widths for each of the multiple notches. Figure 6.12 shows this case with $\beta_o = 0.8$ and $\beta_1 = 0.2$. As shown in figure 6.12 the notch at f_1 is narrower than at f_o. The SQNR are $\gamma_f = 15.947$dB and $\gamma_b = 8.21$dB. Note that since we have a narrower width for f_1, we get a lower out-of-band noise compared to the non-weighted spectrum in figure 6.10.

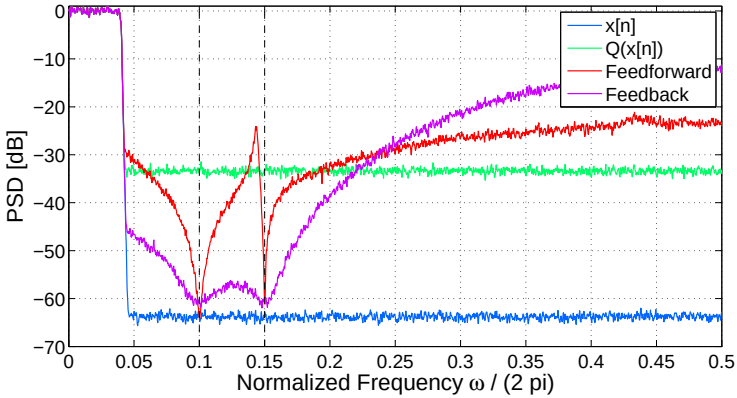

Figure 6.12: PSD of original signal, quantized signal with $n_h = 10$, $n_l = 5$, and shaped quantization noise with 2 notches $f_o = 0.1$ and $f_1 = 0.15$ with $\beta_o = 0.8$ and $\beta_1 = 0.2$

Notch depth

Now we simulate the effect of the notch depth control factor λ. Figure 6.13 shows the PSD for different λ values. The simulation yields $\gamma_{\lambda=1} = 19.29$, $\gamma_{\lambda=0.95} = 19.88$, $\gamma_{\lambda=0.87} = 20.71$, and $\gamma_{\lambda=0.77} = 22.75$. Figure 6.13 also shows that as the depth control factor λ decreases, the out-of-band noise spectral level also decreases.

Notch width

Finally, we investigate the effect of varying the notch width parameter β. Figure 6.14 shows the PSD of the feedforward approach for different values of β. The simulation

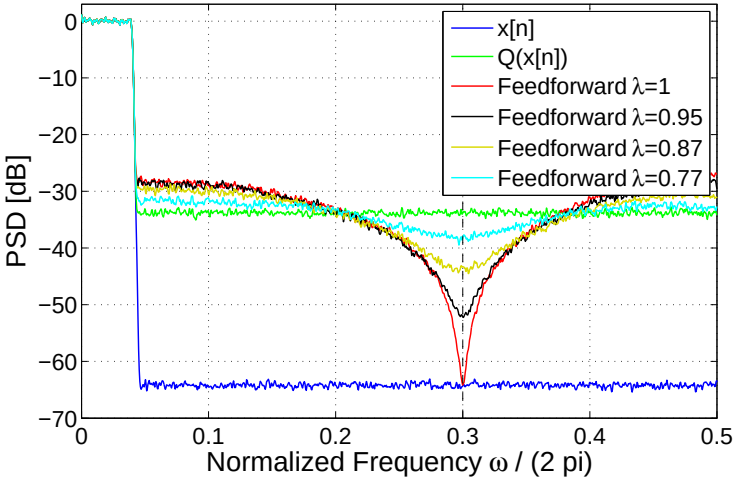

Figure 6.13: PSD of original signal, quantized signal with $n_h = 10$, $n_l = 5$, and shaped quantization noise with $f_o = 0.3$ with notch depth factor $\lambda = 0.77, 0.87, 0.95, 1$

yields $\gamma_{\beta=1} = 19.93$, $\gamma_{\beta=0.6} = 21.53$, and $\gamma_{\beta=0.4} = 22.16$. Similar to λ, as β decreases the out-of-band noise also decreases.

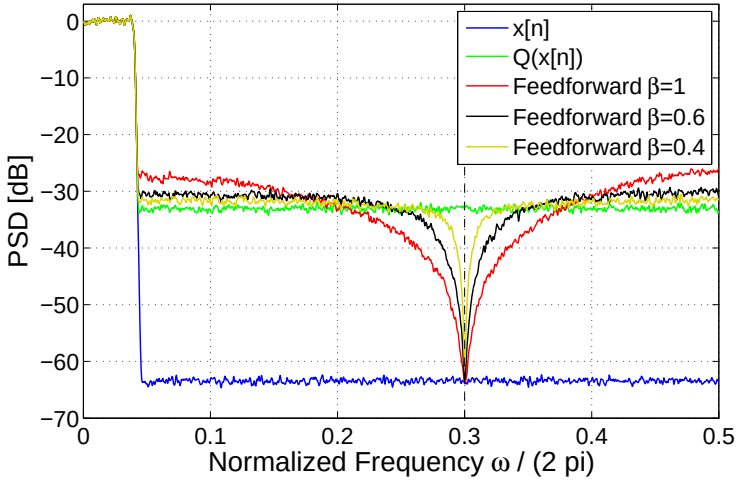

Figure 6.14: PSD of original signal, quantized signal with $n_h = 10$, $n_l = 5$, and shaped quantization noise with $f_o = 0.3$ with notch width factor $\beta = 0.4, 0.6, 1$

6.5. Noise shaping in communications

So far, we discussed the principle of shaping the quantization noise for a general purpose quantization application. The noise shaping principle can be used in several applications such as audio compression [Herre, 1999], as well as image processing [Antonini et al., 1992]. However, in this section the feasibility of the feedforward approach in digital communications is investigated.

First, an overview is presented on the restrictions imposed on the spectrum of the transmitted signal by the spectral emission mask. Then, the applicability of the feedforward algorithm for both the IQ transmitter and the polar transmitter is investigated.

6.5.1. Spectral mask

Spectrum emission mask (SEM), shortly referred to as the spectral mask, is a set of restrictions enforced by the standardization of communication protocols in order to regulate the spectral level of the out-of-band emissions. Figure 6.15 shows the spectral mask for different transmit bandwidth signals according to the standardization in [3GPP, 2014] fo different LTE bandwidth signals.

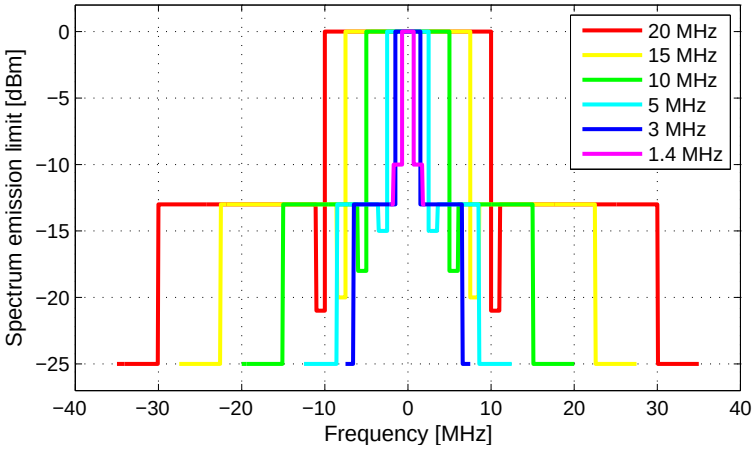

Figure 6.15: LTE spectral mask

The mask shown in figure 6.15 acts as a hard limit, which no transmitter should violate. However, usually designers of transmitters tend to have even stricter limitations on the transmission level for marketing purposes. Transmitters with high CNR have better estimation and correction of the downlink channel, as well as better voice quality, and generally improved throughput. The stricter requirements of designers usually include several notches as shown in figure 6.16.

From figure 6.16, one can see that the mask has some notches at certain frequencies which correspond to downlink protocols. From section 4.4, we know that the out-of-band noise level is related to the time resolution of the DTC. Therefore, the time resolution should be enhanced in order to satisfy the deepest notch of −81 dBm shown in figure 6.16. However, we can take advantage of the notch structure of the spectral mask by *shaping* the out-of-band noise and still use the more efficient low resolution DTC. In this case we can choose to have a coarse time/frequency resolution which satisfies the −66 dBm floor in figure 6.16, while having notches at the frequencies around $f = 100$ and $f = 400$ MHz. This way we use an efficient DTC, while still complying to the spectral mask.

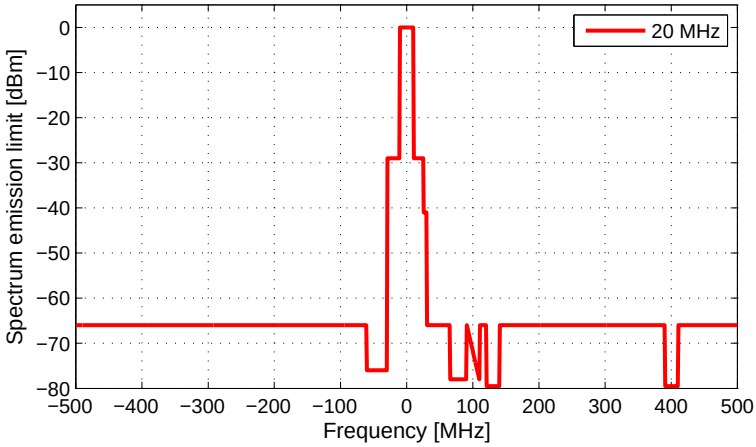

Figure 6.16: Strict spectral mask imposed by hardware designers

6.5.2. Noise shaping in transmitters

The feedforward noise shaper can be used in the IQ or polar transmitter. In the IQ transmitter, the noise shaping algorithm is applied on the Cartesian coordinates $i(t)$ and $q(t)$. Whereas, in the polar transmitter, the noise shaping algorithm is applied to the polar signals $r(t)$ and $\theta(t)$. In this section, the difference between the spectral shape of the notch in the IQ and polar transmitter cases is investigated. We assume that the noise-shaped complex signal using an IQ transmitter is denoted as

$$s_{IQ}^{\lambda,\beta} = \tilde{i}_{\beta}^{\lambda} + j\tilde{q}_{\beta}^{\lambda}, \tag{6.27}$$

while the noise-shaped signal using a polar transmitter is denoted as

$$s_{RP}^{\lambda,\beta} = \tilde{r}_{\beta}^{\lambda} \cdot e^{j\tilde{\theta}_{\beta}^{\lambda}}, \tag{6.28}$$

where the scripts λ and β denote the notch depth parameter and the notch width, respectively. Both complex signals are assumed to have limited bandwidth and quantization noise with flat spectrum.

IQ vs polar noise shaping

The first investigation considers the spectrum of $s_{IQ}^{\lambda,\beta}$ and $s_{RP}^{\lambda,\beta}$ for different values of λ and β. Figure 6.17 shows the resulting spectrum for $\lambda = \{0.9, 0.95, 1.0\}$ and $\beta = \{0.6, 0.8, 1.0\}$ with a normalized signal bandwidth of 0.05 and a notch at $\omega_o = 0.528$.

It can be seen that the notch in $s_{IQ}^{\lambda\beta}$ is always deeper than in $s_{RP}^{\lambda\beta}$. This was previously explained in section 3.4.2. Since the recombination of the noise-shaped polar signals $\tilde{r}_{\beta}^{\lambda}$ and θ_{β}^{λ} is non-linear, then the resultant notch is not as deep as in the Cartesian case.

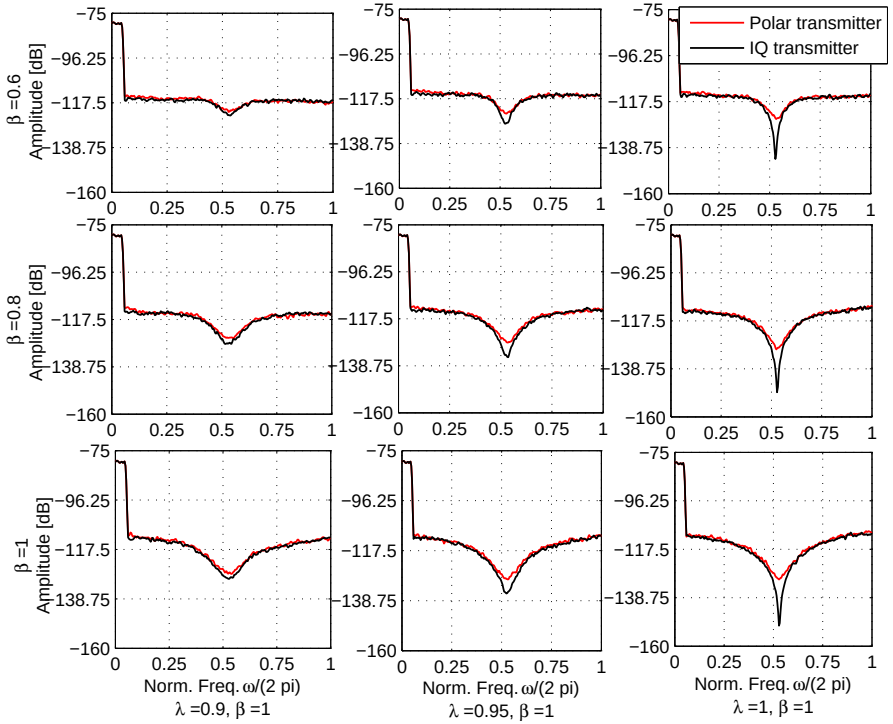

Figure 6.17: Feedforward noise shaping for Cartesian vs polar signals with changing λ and β

A similar investigation is done but with a signal with wider bandwidth. This time the bandwidth is set to 0.2 instead of 0.05 while keeping the notch at the same position. Figure 6.18 shows the resulting spectra.

It can be concluded that the discrepancy between the IQ and polar signals notch becomes larger for a signal with wider bandwidth. This is due to the fact that the notch width and depth, in the polar case, are dependent on the bandwidth of the baseband

signal as explained in 3.4.2.

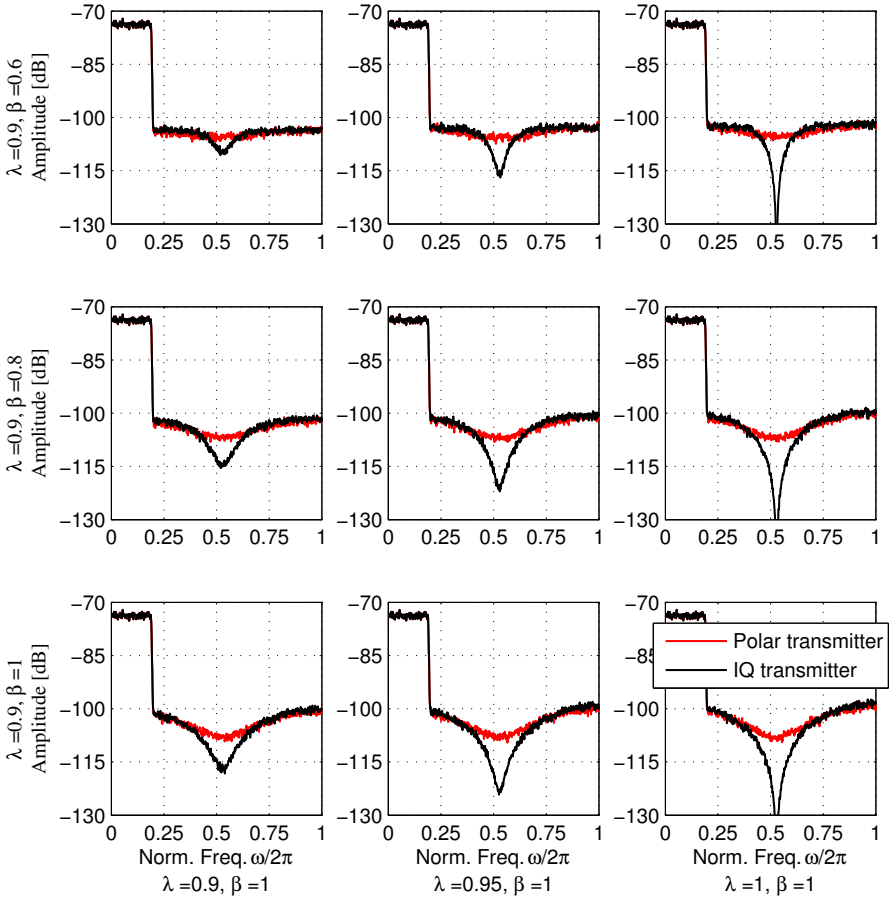

Figure 6.18: Feedforward noise shaping for Cartesian vs polar signals with changing λ and β for a signal with wide bandwidth

Noise shaping of polar signals

The next investigation considers the effect of shaping $\tilde{r}_\beta^\lambda$ and $\tilde{\theta}_\beta^\lambda$ using different parameters λ and β. We would like to know which polar signal has more impact on the notch

in $s_{RP}^{\lambda\beta}$. For this purpose, the spectrum of the polar signal $s_{RP}^{\lambda\beta}$ is simulated with different λ and β for the radius and the phase.

Figure 6.19 shows the effect of varying λ and β for r and θ. From figure 6.19, we arrive at an important conclusion that shaping the phase signal has a stronger influence on the shape of the notch in $s_{RP}^{\lambda\beta}$. This is confirmed by the fact that as the parameters λ and β approach 1 for θ, the notch becomes deeper. However, increasing λ and β for r exhibits a weaker influence on the notch depth.

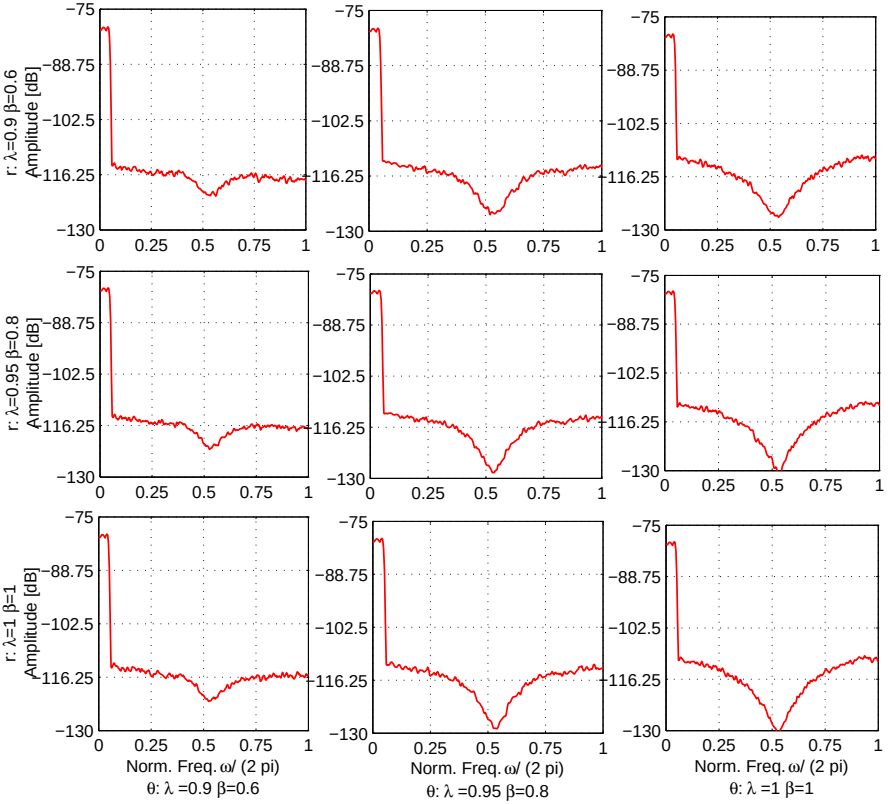

Figure 6.19: Effect of varying λ and β on spectrum of polar feedforward noise shaping

Similar to the previous section, the effect of having a signal with wider bandwidth is investigated. The results are shown in figure 6.20. The bandwidth is increased to 0.2.

It is shown that the difference between shaping the radius and phase is not as large as in case of the narrow band signal shown in figure 6.19.

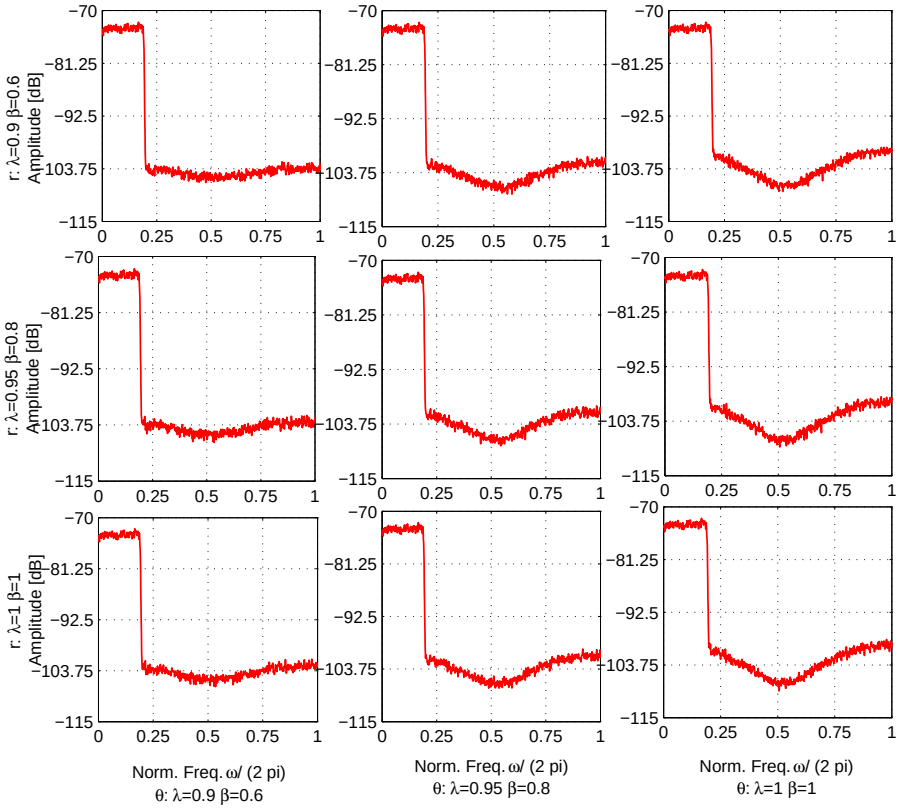

Figure 6.20: Effect of varying λ and β on spectrum of polar feedforward noise shaping for a signal with wide bandwidth

6.6. Discussion

In this chapter, we presented a novel noise shaping algorithm based on coarse corrections, which proved its superiority over traditional feedback noise shaping circuits. In section 6.5, we compared the proposed algorithm for the IQ and polar transmitters. It

has been shown that the resultant notch in the polar case is wider and less deep than in the IQ case. While this can be useful for some situations when the notches in the spectral mask are not so deep, but are rather closely packed next to each other, it is still desirable to have an algorithm which will have a deep narrow notch for the polar transmitter case. For this purpose, a novel algorithm has been developed and will be discussed in chapter 7.

7. Polar Predistortion

The excess out-of-band noise is one of the most significant limitations of the polar transmitter. The out-of-band noise has been analyzed theoretically in section 5.4.1. An approach to reduce the out-of-band noise has been discussed in section 5.4. As mentioned in section 5.4, the oversampling approach requires the DAC to operate at high sampling rates which might be difficult to achieve given the current DAC capabilities. In chapter 6, a feedforward noise shaping approach has been introduced for general purpose noise shaping. However, this approach is not well-suited for the actual polar transmitter architecture explained in chapters 4 and 5. In this chapter, we introduce an algorithm which is tailored for the polar transmitter architecture considered in this thesis.

This chapter is divided into three parts. First, we explain the reason for having digital predistortion in polar transmitters rather than traditional analog filtering. In the second part, a new adaptive filtering algorithm is introduced which uses the polar predistortion principle. Finally, a novel *error dependent* algorithm is presented for predistorting the radius and instantaneous period in order to obtain notches in the out-of-band noise of the transmitted signal, which was presented in Ibrahim and A. [2015].

7.1. Digital versus analog filtering

The analog transmitted signal $s(t) = r(t) \cdot \cos(\omega_c t + \theta(t))$ should abide to the spectral mask explained in section 6.5.1. The simplest and most obvious way to filter $s(t)$ is to use an analog filter $h_a(t)$ as shown in figure 7.1a such that the transmitted signal becomes

$$s_a(t) \quad = \quad s(t) * h_a(t) \ . \tag{7.1}$$

The analog filter $h_a(t)$ ensures that $s_a(t)$ contains no out-of-band components which might violate the spectral mask. Although analog filter design techniques are pretty well established in literature, their usage would contradict the most important advantage of polar transmitters, which is being digital and compact. Accordingly, signal

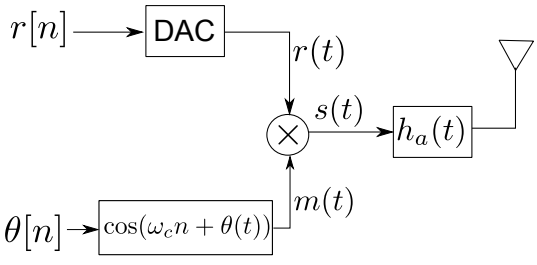

(a) Analog filtering

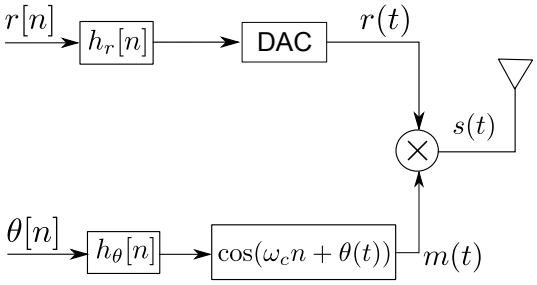

(b) Digital predistortion

Figure 7.1: Analog filtering versus digital predistortion

processing algorithms should be applied at the digital domain to mimic the effect of an analog filter $h_a(t)$.

Figure 7.1b shows the general principle of polar predistortion which is considered in this chapter. As shown, the digital filters h_r and h_θ should be implemented in order to filter the transmitted signal. In this chapter, two methods to design the filters h_r and h_θ are presented.

7.2. Adaptive polar predistortion

Consider the complex baseband digital signal

$$\check{s}[n] \quad = \quad i[n] + \jmath q[n] = r[n] \cdot e^{\jmath\theta[n]} \ . \tag{7.2}$$

In order to filter $\check{s}[n]$, we need to filter its Cartesian or polar components. By filtering the Cartesian components using an FIR filter, we get

$$s_f[n] \quad = \quad h_i * i[n] + \jmath h_q * q[n] \ . \tag{7.3}$$

Generally speaking, $i[n]$ and $q[n]$ are considered independent. Therefore, the filters h_i and h_q can be identical $h_i = h_q = h$. Thus, equation 7.3 simplifies to

$$s_f[n] = (i[n] + \jmath q[n]) * h[n] \tag{7.4}$$

Equation (7.3) can be represented in its polar form as

$$s_f[n] = (r[n]e^{\jmath\theta[n]}) * h[n] \tag{7.5}$$

$$= \sum_{i=0}^{N} r[n-i]e^{\jmath\theta[n-i]} \cdot h[i] \ , \tag{7.6}$$

where $h[i]$ are the filter coefficients of the filer h, and N is the filter order.

When applying any arbitrary filter h_r and h_θ to the polar coordinates, we get

$$s_p[n] = h_r[n] * r[n] \cdot e^{\jmath h_\theta[n] * \theta[n]} \ . \tag{7.7}$$

We would like to tune the filters h_r and h_θ in order to match the filtered output $s_p[n]$ to $s_f[n]$. Since $r[n]$ and $\theta[n]$ are coupled, then the tuning of h_r and h_θ is not a trivial task. In this section, we explain how to adaptively and jointly tune the filter coefficients of h_r and h_θ in order to get a filtered signal $s_p[n]$ which is similar to the reference signal $s_f[n]$.

7.2.1. Analysis

In this section, we analyze the effect of filtering $r[n]$ and $\theta[n]$ using the FIR filters h_r and h_θ, respectively[1].

Applying the filter h_r to the radius signal as in figure 7.1b yields

$$r_f[n] = \sum_{i=0}^{N} r[n-i] \cdot h_r[i] \ , \tag{7.8}$$

where $h_r[i]$ are the coefficients of the filter h_r. Similarly, the filtered phase signal is defined as

$$\theta_f[n] = \sum_{i=0}^{N} \theta[n-i] \cdot h_\theta[i] \ , \tag{7.9}$$

where $h_\theta[i]$ are the coefficients of the filter h_θ. Combining $r_f[n]$ and $e^{\jmath\theta_f[n]}$ we get the complex signal $s_p[n]$

$$s_p[n] = \left(\sum_{i=0}^{N} r[n-i]h_r[i] \right) \cdot e^{\jmath \sum_{i=0}^{N} \theta[n-i]h_\theta[i]} \ . \tag{7.10}$$

[1] FIR filters are used since they are more stable than IIR at RF sampling rates.

We would like to match equation (7.10) to equation (7.6), so that by adjusting the filter coefficients $h_r[n]$ and $h_\theta[n]$, we obtain $s_f[n] = s_p[n]$.

Comparing the expansion of the radius summation in equation (7.10) to the expansion of the summation in equation (7.6) for a certain time sample n we get

$$\begin{aligned} s_p[n] &= r[n]h_r[0]e^{J\sum_{i=0}^{N}\theta[n-i]h_\theta[i]} + r[n-1]h_r[1]e^{J\sum_{i=0}^{N}\theta[n-i]h_\theta[i]} + \dots \\ &+ r[n-N]h_r[N]e^{J\sum_{i=0}^{N}\theta[n-i]h_\theta[i]}, \\ s_f[n] &= r[n]h[0]e^{J\theta[n]} + r[n-1]h[1]e^{J\theta[n-1]} + \dots \\ &+ r[n-N]h[N]e^{J\theta[n-N]}. \end{aligned} \tag{7.11}$$

As a first step, we consider tuning $h_\theta[i]$. By comparing the phase terms in $s_p[n]$ to those of $s_f[n]$ in equation (7.11), we see that each term of the summation in $s_p[n]$ is a weighted sum $\sum_{i=0}^{N}\theta[n-i]\cdot h_\theta[i]$, whereas in $s_f[n]$, each term of the summation has a single term $\theta[n-i]$. Accordingly, we set the filter coefficients $h_\theta[i]$ as

$$h_\theta[i] = 1 \quad \text{for} \quad 0 \le i < N. \tag{7.12}$$

Applying those filter coefficients in equation (7.12) to equation (7.11) yields

$$s_p[n] = r[n]h_r[0]e^{J\sum_{i=0}^{N}\theta[n-i]} + r[n-1]h_r[1]e^{J\sum_{i=0}^{N}\theta[n-i]} + \dots + r[n-N]h_r[N]e^{J\sum_{i=0}^{N}\theta[n-i]}.$$

The second step is to tune the radius filter coefficients $h_r[i]$ to complete the matching process. We can set the radius filter coefficients as

$$h_r[n,i] = h[i]e^{J[\theta[n-i]-\sum_{j=0}^{N}\theta[n-j]]}. \tag{7.13}$$

Equation 7.13 shows that the filter h_r is actually an adaptive filter, which changes its coefficients according to the phase signal θ unlike the phase filter h_θ which is an FIR filter with fixed coefficients.
By substituting equation (7.13) into equation (7.11) we get

$$\begin{aligned} s_p[n] &= r[n]h[0]e^{J\theta[n]-J\sum_{i=0}^{N}\theta[n]}e^{J\sum_{i=0}^{N}\theta[n-i]} + r[n-1]h[1]e^{J\theta[n-1]-J\sum_{i=0}^{N}\theta[n-1]}e^{J\sum_{i=0}^{N}\theta[n-i]} + \dots \\ &\quad + r[n-N]h[N]e^{J\theta[n-N]-J\sum_{i=0}^{i=N}\theta[n-i]}e^{J\sum_{i=0}^{i=N}\theta[n-i]} \\ &= s_f[n]\cdot \end{aligned} \tag{7.14}$$

This is done by adaptively tuning the coefficients $h_r[n,i]$, according to equation (7.13) and fixing $h_\theta[i] = 1$.

7.2.2. Block diagram

Figure 7.2 shows a block diagram of the adaptive predistortion algorithm explained in the last section. The block diagram is tailored for a second order FIR filter with $N = 2$. As shown, there is a *CONTROL* unit which takes the phase signals $\theta[n]$, $\theta[n-1]$, and $\theta[n-2]$ as an input. The control unit tunes the radius filter coefficients $h_r[i]$ according to equation (7.13).

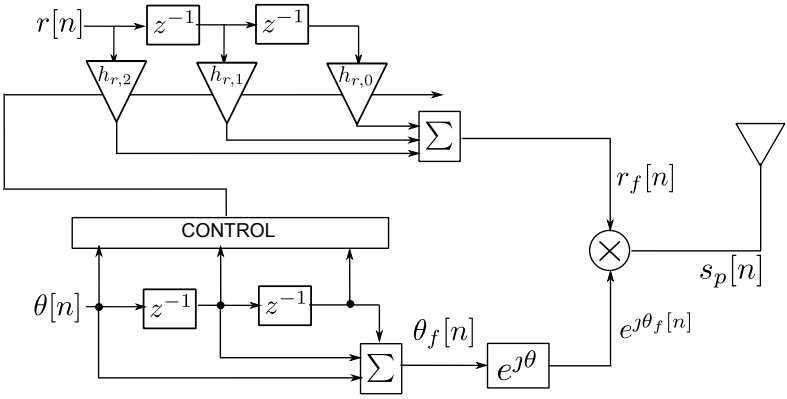

Figure 7.2: Block diagram for theoretical predistortion algorithm

Efficient computation of h_r

In equation (7.13), the coefficients $h_r[i]$ are complex and are a non-linear function of the phase signal $\theta[n]$. We would like to simplify this non-linear function by using a Taylor series approximation. Consider the real part of the exponential in equation (7.13)

$$Re\{h_r[n,i]\} = h[i]\cos(\theta[n-i] - \sum_{j=0}^{N} \theta[n-j]) \tag{7.15}$$

$$= h[i]\cos(\psi_i[n]) \ . \tag{7.16}$$

The cos function is difficult to implement at RF sampling rates. Therefore, we need to find a series expansion of the term $\cos(\psi_i[n])$. Figure 7.3 shows the Taylor approximation of a cosine wave with different approximation orders centered around $\psi = \pi$.

An expansion order of 9 is challenging to achieve at RF sampling rates. In order to simplify the computation process, we take advantage of the symmetry of the cosine

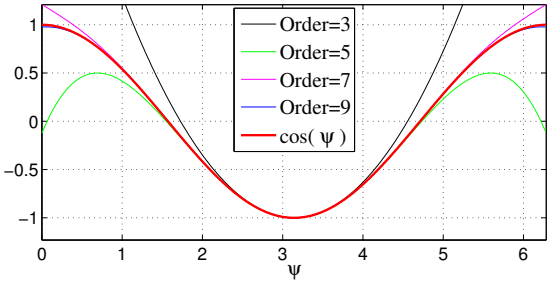

Figure 7.3: Taylor approximation of cos(ψ)

curve. The part of the cosine curve in the range $0 \leq \psi < \pi/2$ has all the unique information of the sinusoidal wave. The range $\pi/2 \leq \psi < \pi$ is a mirror of the range $0 \leq \psi < \pi/2$ made along the x and y axis, the range $\pi \leq \psi < 1.5\pi$ is a mirror along the x-axis and the range $1.5\pi \leq \psi < 2\pi$ is a mirror along the y-axis. Therefore, we can obtain a series expansion of the cosine function only at the range $0 \leq \psi < \pi/2$ as it contains all the unique information. Then we can map the range $\pi/2 \leq \psi < \pi$ to $0 \leq \psi < \pi/2$ in order to find their cosine values. Figure 7.4 shows the Taylor series expansion for the range $0 \leq \psi < \pi/2$. As shown, with an approximation order of 4, we get a quite good approximation of the cosine function.

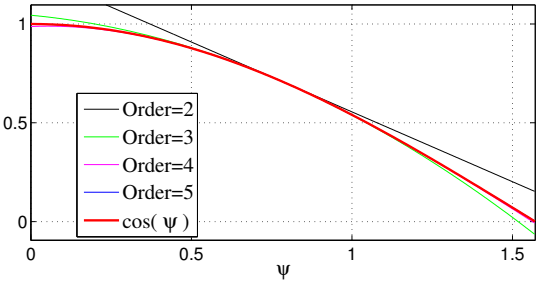

Figure 7.4: Taylor approximation of cos(ψ) for the range $0 \leq \psi < \pi/2$

Now, we need to define the mapping function of the phase values which are outside the range $0 \leq \psi < \pi/2$. Figure 7.5 shows the mapping of the original signal ψ to the phase mapped ψ_m. The mapped phase ψ_m is then input to the Taylor polynomial shown

in figure 7.4. The output of the Taylor polynomial is then multiplied by the sign factor shown in figure 7.5 as color code.

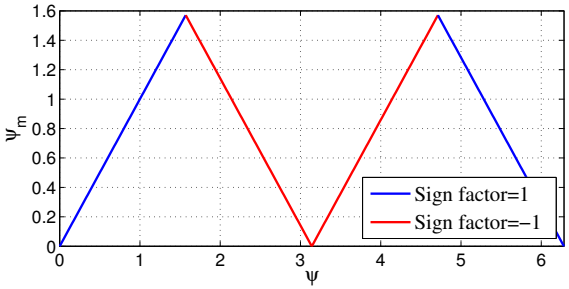

Figure 7.5: Mapping of ψ to ψ_m and the output factor

Figure 7.6 summarizes the simplified signal processing operations to compute h_r. The tuning process takes as an input the phase signals $\theta[n-i]$ and $\sum_{i=0}^{N}\theta[n-i]$. Then we obtain the phase ψ which is then mapped into the $0 \leq \psi < \pi/2$ range using a mapper. The mapper outputs the sign factor, and ψ_m which is then fed into the Taylor approximation block. The output is finally multiplied by the sign factor and h_q to obtain h_r. Note that the Taylor approximation block contains also an approximation of the sine wave, in order to achieve a Taylor approximation of the term $exp(j[\theta[n-1]-\sum_{i=0}^{i=N}\theta[n-i]])$.

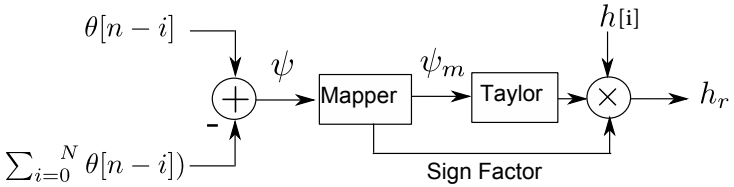

Figure 7.6: Calculation of the filter coefficient $h_r[n,i]$

7.2.3. Results

In this section, the results of the adaptive polar predistortion algorithm are presented. Two aspects of the approach will be investigated. First, the fidelity of the spectrum of

the resulting signal s_p compared to the reference spectrum of s_f. The second aspect is the effect of the approximation factor of the Taylor series expansion on the spectrum.

Notch spectrum

In this section, a baseband signal is simulated. Additionally, we investigate the spectrum of the predistorted signal. For this part, an accurate calculation of the filter coeffi-

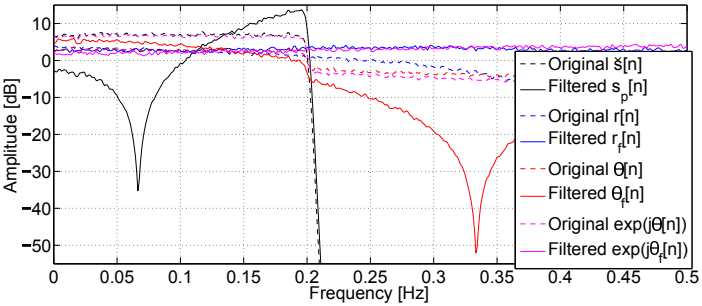

Figure 7.7: Spectrum of non filtered signal and filtered signal using a second order notch filter with $f_o = 0.06647$

Figure 7.7 shows the spectrum of the original signal $\check{s}[n]$ and the reference filtered signal $s_p[n]$. The predistortion is based on a second order notch filter with a normalized notch frequency $f_o = 0.06647$. We also plot the spectrum of the signals $r[n]$, $r_f[n]$, $\theta[n]$, $\theta_f[n]$, $e^{j\theta[n]}$, and $e^{j\theta_f[n]}$.

As shown, we do obtain a notch at the predistorted signal $s_p[n]$ at the frequency $f_o = 0.06647$. It is also clear that the filtered phase signal θ_f has a notch at 0.33 Hz. This is intuitive because the coefficients of the phase filter are $h_\theta[0] = h_\theta[1] = h_\theta[2] = 1$ which are the coefficients of a second order notch filter with $f_o = 1/3$. What is also interesting to note, is that the spectrum of $r_f[n]$ and $e^{j\theta_f[n]}$ become wider than their non-filtered counterparts. However, when $r_f[n]$ and $e^{j\theta_f[n]}$ are multiplied in the time domain which is a convolution in the frequency domain, the resultant signal $s_p[n]$ has a narrower spectrum signal with a notch.

Approximation order

In this section, the effect of the Taylor approximation order on the spectrum of s_p is investigated. Figure 7.8 shows the spectrum of the transmitted signal with different approximation orders. In this simulation, the cosine wave is expanded for the complete range $0 < \psi < 2\pi$ according to figure 7.3. We can see that an expansion order of 11 or higher is needed in order to have a notch shape similar to the reference.

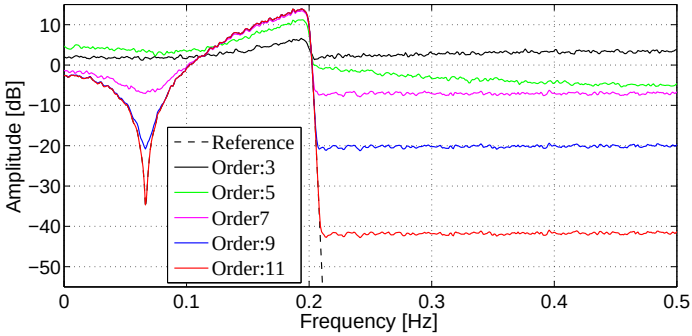

Figure 7.8: Spectrum of filtered signal for different expansion orders for a complete cosine wave approximation

Now, we simulate the approach of mapping the angle ψ to ψ_m according to figure 7.6. Figure 7.9 shows the resulting spectrum. We can see that an expansion order of 4 is already satisfactory in order to obtain a similar notch as in the reference. Compared to the full cosine approximation, we get an improvement of $11 - 4 = 7$ orders of approximations.

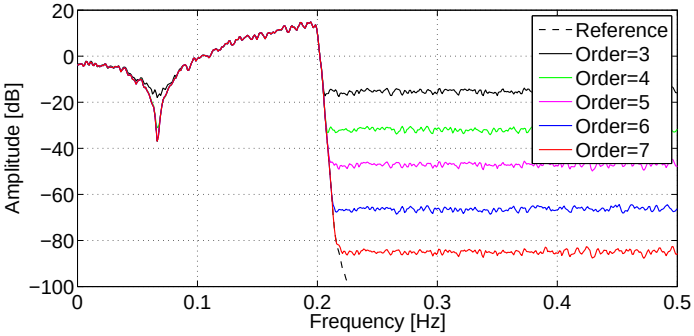

Figure 7.9: Spectrum of filtered signal for different expansion orders for a mapped phase $0 < \psi_m < \pi/2$

7.3. Error dependent polar predistortion

In the previous section, we presented an algorithm for filtering the polar signals by adaptively tuning the coefficients which filter the radius $r[n]$ and phase $\theta[n]$. However, the architecture which was described in chapter 5 does not have an ideal digital-to-analog conversion for radius $r[n] \xrightarrow{DAC} r(t)$. Similarly in chapter 4, we showed that the phase modulation process $\theta[n] \xrightarrow{DTC} \cos(\omega_c t + \theta(t))$ is not ideal as well. Therefore, we need to have an approach which is tailored for the current architecture of the polar transmitter.

In this section, we present an algorithm which filters only the time quantization noise which we described in section 4.4. First, a model of the actual error signal which needs to be filtered is presented. Afterwards, an explanation of the algorithm which adaptively filters this error will be presented. Finally, the results of the algorithm will be shown.

7.3.1. Error signal

In section 4.4, we presented an analysis of the time quantization error in order to estimate the spectral level of the out-of-band noise. In this section, the same time domain model of the error will be used. Figure 7.10 shows 3 signals: the error $\bar{e}(t)$ caused by the DTC time quantization, $\bar{r}(t)$ is the output of the DAC based on the data-dependent averaging technique described in chapter 5, and their product $\bar{\bar{q}}(t) = \bar{e}(t) \cdot \bar{r}(t)$. The time quantization error $\bar{\bar{q}}(t)$ considered in this chapter contains all the DAC and DTC distortions discussed so far. It has been shown in section 4.4 that the time quantization is the

main component of the out-of-band noise. Hence, in this approach we introduce some distortions to $\bar{\bar{q}}(t)$ in a way such that the filtered spectrum of $\bar{\bar{q}}(t)$ will have a shaped spectrum.

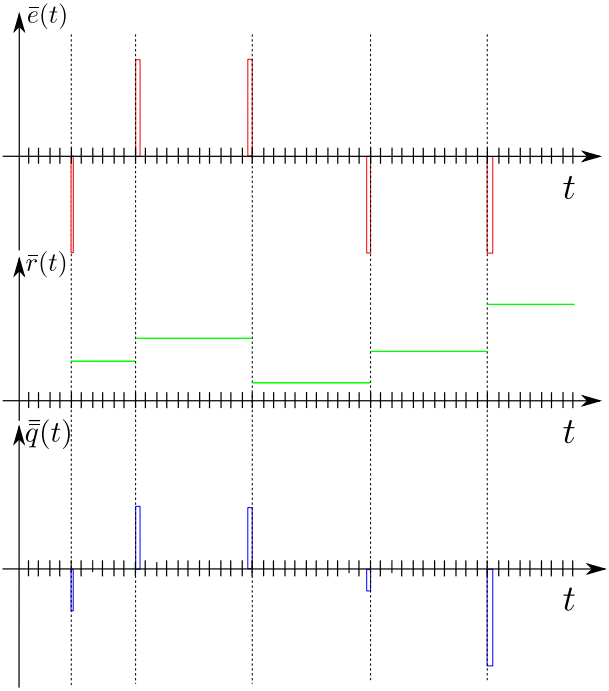

Figure 7.10: DTC time quantization error $\bar{e}(t)$, radius signal $\bar{r}(t)$, and their product $\bar{\bar{q}}(t) = \bar{e}(t) \cdot \bar{r}(t)$

7.3.2. Algorithm

Before explaining the algorithm, we need to clarify which signals we can actually modify in order to filter $\bar{\bar{q}}(t)$. We can only process the digital signals which are fed into the DAC and DTC:

1. $r[n]$: The radius signal can be distorted by adding a small distortion value ϵ_r. We need to keep in mind that the DAC will average $r[n]$ over the instantaneous period as explained in section 5.3.1.

2. $\upsilon[m]$: The DTC takes as an input the instantaneous period. So we can change $\upsilon[m]$ by adding a distortion value $\pm i/f_s$, where i is a positive integer and f_s is the sampling frequency of the DTC.

The proposed algorithm modifies the signals mentioned above in an effort to shape the out-of-band noise. We need to note that the predistortion error introduced should be as small as possible so that we do not distort the in-band signal.

Radius distortion

Distorting the radius signal can be done by adding or subtracting a small value ϵ_r. Figure 7.11 shows the effect of distorting the radius signal. As shown, changing the radius can only change the amplitude of the error signal $\bar{\bar{q}}(t)$ but not the sign.

Instantaneous period distortion

The instantaneous period $\upsilon[m]$ which is fed to the DTC is actually a quantized signal of a higher precision signal $\upsilon_o[m]$. Distorting the instantaneous period can be done during this quantization operation. Instead of shifting the DTC toggle to the closest time grid instant, the toggle is shifted to the second closest time instant. Figure 7.13 shows the effect of increasing the instantaneous period by $1/f_s$ for a single toggle. This distortion results in flipping the sign of the error $\bar{e}(t)$. However, the error energy increases as the error pulse width increases. The effect of instantaneous period distortion is shown in figure 7.12.

Possible predistortion combinations

As stated, distorting the radius changes the amplitude of the error pulses in $\bar{\bar{q}}(t)$ while distorting the instantaneous period changes the sign of the error pulses in $\bar{\bar{q}}(t)$. Using those two possibilities we can introduce distortions which can shape the spectrum of $\bar{\bar{q}}(t)$.

$\bar{\bar{q}}(t)$ is formed of a train of error pulses. For each error pulse there are several possible combinations of predistortion. Of course, when distorting $r[n]$ and $\upsilon[m]$, the overall noise energy is increased, but we are specifically interested in the noise frequency component at the notch frequency $\bar{\bar{Q}}(\omega_o)$. For each distortion we do at each error pulse, $\bar{\bar{Q}}(\omega_o)$ changes to become $\tilde{\bar{Q}}(\omega_o)$. The distortions should be applied in order to minimize $|\tilde{\bar{Q}}(\omega_o)|$ as much as possible.

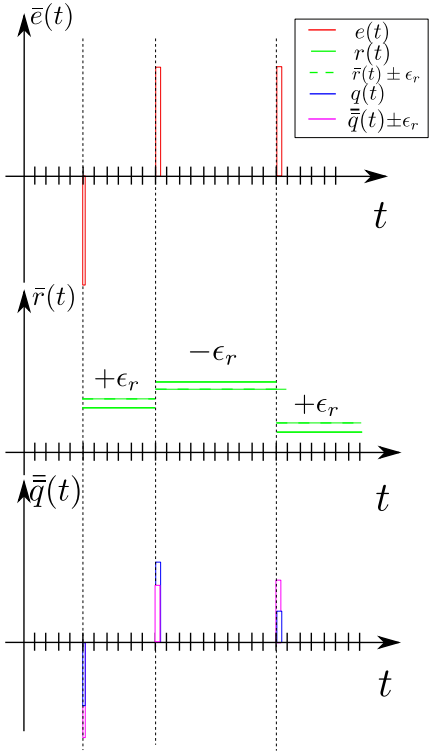

Figure 7.11: Effect of distorting the radius signal using ϵ_r

Index	Radius distortion	Instant. period distortion	Resultant freq. bin
P1	0	0	$\tilde{\bar{Q}}_1(\omega_o)$
P2	$+\epsilon_r$	0	$\tilde{\bar{Q}}_2(\omega_o)$
P3	$-\epsilon_r$	0	$\tilde{\bar{Q}}_3(\omega_o)$
P4	0	Υ	$\tilde{\bar{Q}}_4(\omega_o)$
P5	$+\epsilon_r$	Υ	$\tilde{\bar{Q}}_5(\omega_o)$
P6	$-\epsilon_r$	Υ	$\tilde{\bar{Q}}_6(\omega_o)$

Table 7.1.: Possible distortions per error pulse and the resultant error bin

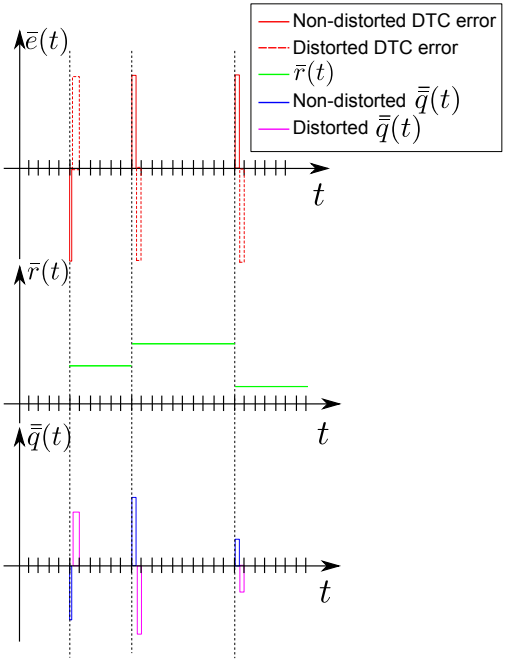

Figure 7.12: Effect of changing the DTC toggle to the second closest time grid on $\bar{\bar{q}}(t)$

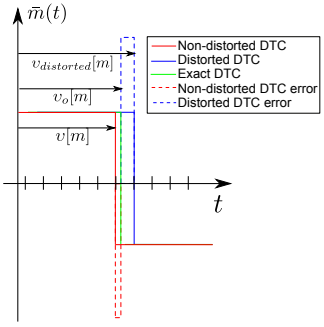

Figure 7.13: Exact output of DTC $\upsilon_o[m]$, quantized output of DTC $\upsilon[m]$, and distorted output of DTC $\upsilon_{distorted}[m]$

Table 7.1 shows the possible distortions done per error pulse. Υ in the table denotes toggle, which means that the instantaneous period is changed by $\pm 1/f_s$. From table 7.1, we can see that we have 6 distortion possibilities per error pulse. Those possibilities might increase by having multiple factors of ϵ_r as $\pm 2\epsilon_r, \pm 3\epsilon_r, \ldots$, but for simplicity, only $\pm\epsilon_r$ is considered.

The possibility P1 corresponds to not doing any distortion which keeps the frequency bin unchanged. Our target is to chose the suitable distortion which will minimize the noise energy. This can be described as

$$i_{opt} = \arg\min_i \{|\tilde{\tilde{\mathrm{Q}}}_i(\omega_o)|\} \quad \text{, where} \quad i \in \{1, 2, \ldots 6\} \; . \tag{7.17}$$

In this equation, i_{opt} defines the optimal index of the predistortion type, $|\tilde{\tilde{\mathrm{Q}}}_i(\omega_o)|$ corresponds to the resultant amplitude of the frequency component when applying the predistortion with index i, and Pi_{opt} is defined as the optimal distortion to do out of P1, P2, P3, P4, P5, and P6.

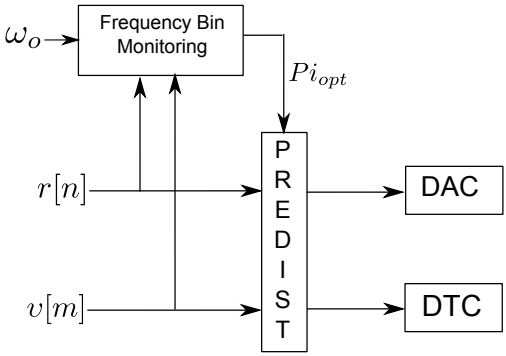

Figure 7.14: Predistortion block diagram

Figure 7.14 shows an abstract block diagram of the predistortion algorithm. The *frequency bin monitoring* block is tuned to a certain notch frequency ω_o which updates the frequency bin $\tilde{\tilde{\mathrm{Q}}}_i(\omega_o)$. This block is responsible of checking all the possible distortions described in table 7.1 and find the optimal correction Pi_{opt}. The predistortion block then performs the corresponding distortion on the radius and instantaneous period.

7.3.3. Frequency bin monitoring

In this section, it will be explained how the *frequency bin monitoring* block can accurately estimate the frequency bin component $\tilde{\bar{Q}}_i(\omega_o)$. Basically, we need to find the Fourier transform of the error signal $\tilde{\bar{q}}(t)$ at ω_o. Recall the Fourier transform equation

$$\tilde{\bar{Q}}(\omega_o) = \int_{-\infty}^{\infty} \tilde{\bar{q}}(t) e^{-j\omega_o t} \mathrm{d}t \ . \tag{7.18}$$

We know that the signal $\tilde{\bar{q}}(t)$ is a train of rectangular error pulses $\bar{e}(t)$ which are scaled by the radius $\bar{r}(t)$. Equation (7.18) integrates the signal $\tilde{\bar{q}}(t)$ when multiplied by the complex sinusoidal $e^{-j\omega_o t}$. Decomposing the frequency component $\tilde{\bar{Q}}(\omega_o)$ into real and imaginary parts we obtain

$$\Re(\tilde{\bar{Q}}(\omega_o)) = \int_{-\infty}^{\infty} \tilde{\bar{q}}(t) \cos(\omega_o t) \mathrm{d}t \ , \tag{7.19}$$

$$\Im(\tilde{\bar{Q}}(\omega_o)) = -\int_{-\infty}^{\infty} \tilde{\bar{q}}(t) \sin(\omega_o t) \mathrm{d}t \ . \tag{7.20}$$

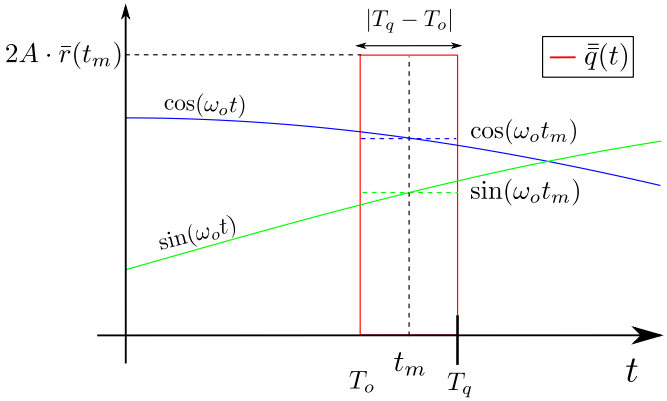

Figure 7.15: Error pulse of $\bar{\bar{q}}(t)$ and relevant signals to update the Fourier transform

Now consider the time instant t_m at a certain error pulse as shown in figure 7.15. We need to calculate the area of the square pulse based on equation (7.18) for the current pulse as

$$\int_{t=T_o}^{T_q} \tilde{\bar{q}}(t) e^{-j\omega_o t} \mathrm{d}t \ . \tag{7.21}$$

The area of the pulse after being multiplied with $e^{-j\omega_o t}$ is integrated with all previous pulses in order to obtain the frequency bin $\tilde{\tilde{\mathrm{Q}}}(\omega_o)$. In order to calculate the area of the pulse, we need to compute the amplitude and duration of the pulse. Those values can be calculated as follows:

Amplitude

We can assume the sinusoids $\cos(\omega_o t)$ and $-\sin(\omega_o t)$ to be constant for the time duration of the pulse $\check{d} = |T_q - T_o|$. This is a valid assumption since the maximum possible pulse width is $\max(|\check{d}|) = 1/(2f_s)$. Assuming that the time resolution is $T_s = 1000/f_c$, then the maximum duration is $\max(\check{d}) = 1/(2000f_c)$. The notch frequency is usually close to the carrier frequency such that $f_o \approx f_c$. This means that the maximum duration of the pulse is $1/2000$ of the period of the sinusoids $\cos(\omega_o t)$ and $-\sin(\omega_o t)$, which validates our approximation that the term $e^{-j\omega_o t}$ is constant within a rectangular pulse. This approximation yields

$$\int_{t=T_o}^{T_q} \tilde{\tilde{\mathrm{q}}}(t) e^{-j\omega_o t} \mathrm{d}t \quad \approx \quad e^{-j\omega_o t_m} \int_{t=T_o}^{T_q} \tilde{\tilde{\mathrm{q}}}(t) \mathrm{d}t \ , \tag{7.22}$$

where $t_m = (T_q + T_o)/2$. The amplitude of the m-th rectangular error pulse is thus

$$\check{A}_m \quad = \quad 2A \cdot r(t_m) \cdot e^{-j\omega_o t_m} \ , \tag{7.23}$$

where A is the amplitude of the square pulses of the DTC, and $r(t_m)$ is the radius value at the time instant of the rectangular error pulse.

Duration

The duration of the pulse can be simply calculated by finding the absolute difference between the exact toggling instant T_o and the quantized toggling instant T_q

$$\check{d} \quad = \quad |T_q - T_o| \ . \tag{7.24}$$

Note that the time precision when calculating the exact toggling time T_o is usually high (16 bits). However, in order to have an efficient DTC with a coarse time grid, the high precision toggling instant T_o is quantized to T_q (10 bits), which means that the accuracy of computing the time quantization duration has word-length of $16 - 10 = 6$ bits which is quite satisfactory, and thus the error pulse width can be well estimated.

Using the previous approximations, the Fourier transform after the pulse at instant t_m can be represented as a recursive summation as follows

$$\tilde{\tilde{\mathrm{Q}}}_{t_m}(\omega_o) \quad = \quad \tilde{\tilde{\mathrm{Q}}}_{t_{m-1}}(\omega_o) + 2A \cdot r(t_m) |T_{q,m} - T_{o,m}| \left(\cos(\omega_o t_m) - j \sin(\omega_o t_m)\right) \tag{7.25}$$

where $\tilde{\tilde{Q}}_{t_{m-1}}(\omega_o)$ is the Fourier transform for all previous pulses before t_m, and the terms $T_{o,m}$ and $T_{q,m}$ are the exact and quantized toggling instants of the m-th error pulse, respectively.

Ideally, we would like the current frequency bin component $\tilde{\tilde{Q}}_{t_m}(\omega_o)$ to be eliminated in order to have a notch at ω_o. Therefore, we would like our predistortion algorithm to possibly modify the toggling instant from $T_{q,m}$ to $T_{p,m}$ and add or subtract a correction value $\epsilon_{r,m}$ to the radius in order to satisfy the following equation

$$\tilde{\tilde{Q}}_{t_{m-1}}(\omega_o) \pm 2A \cdot (r(t_m) + \chi\epsilon_{r,m})|T_{p,m} - T_{o,m}| \left(\cos(\omega_o t_m) - j\sin(\omega_o t_m)\right) = 0 \ , \qquad (7.26)$$

where $\epsilon_{r,m}$ is the small radius correction, χ is either -1, 0, or 1 in order to reflect the different predistortion types in the radius signal, and $T_{p,m}$ is the distorted toggling instant. Note that moving the toggling instant to $T_{p,m}$ could flip the sign of the error pulse as indicated using the $\pm$ sign in equation (7.26).

Theoretically, equation (7.26) has 2 degrees of freedom and can be solved by tuning $\epsilon_{r,m}$ and $T_{p,m}$. However, the choice of $\epsilon_{r,m}$ and $T_{p,m}$ is limited to the following restrictions.

1. $\epsilon_{r,m}$ can only take small values in order not to distort the in-band signal $\epsilon_{r,m} \ll r(t)$.
2. The distorted radius $r(t_m) \pm \epsilon_{r,m}$ can only take positive values $(r(t_m) \pm \epsilon_{r,m}) > 0$ as the DAC expects only positive signals.
3. The distorted toggling instant $T_{p,m}$ can only occur at discrete time instants, this implies that the distorted duration $\check{d}_d = |T_{p,m} - T_{o,m}|$ can only have quantized values.
4. The durations of the predistorted toggling instants should not be large in order not to violate the approximation that the Fourier sinusoid $e^{-j\omega_o t}$ is more or less flat during the pulse as in equation (7.22).

In order to choose the optimal distortion index i_{opt}, the amplitude of each error bin $|\tilde{\tilde{Q}}_i(\omega_o)|$ is computed, and the predistortion index corresponding to the lowest amplitude signal is chosen. At a first glance, this might seem as an inefficient algorithm for signal processing at RF sampling rates. However, as we will show in the next section, not all predistortion types will be checked.

7.3.4. Results

The results of the error dependent predistortion algorithm will be illustrated in this section. The effect of the radius distortion factor ϵ_r will be investigated. It is also

interesting to know how often each of the corrections in table 7.1 occur. Additionally, we would like to know the effect of the choice of the notch frequency ω_o on the notch shape. The metric for evaluating the predistortion algorithm is the depth of the notch at ω_o, as well as the increase in the spectral level of the frequencies away from ω_o. To the best knowledge of the author, there are no available algorithms in literature to obtain notches in the transmitted signal from a polar transmitter architecture which uses a DTC. Therefore, the results in this section are presented without a benchmark for comparison unlike the results of the feedforward noise shaping presented in section 6.4 which were compared to feedback noise shapers.

Effect of ϵ_r

The choice of ϵ_r has an important effect on the performance of the predistortion algorithm. A large ϵ_r means that an overcorrection might occur and consequently the in-band signal gets distorted. On the other hand, a small ϵ_r introduces smaller amplitude distortion, but it might not be enough to cancel the frequency bin. In order to investigate this effect, the predistortion results are simulated for different values of ϵ_r.

Figures 7.16 and 7.17 show the spectrum of the transmitted signal for different values of ϵ_r ranging from 10^{-12} to 10^{-2} with a notch frequency $\omega_o = 2\pi \cdot 1.5$ GHz. The mean value of the radius being distorted is $\mu_r = 9.98 \cdot 10^{-6}$. Figure 7.17 limits the frequency range to $0.2GHz < f < 1.8GHz$ so that the notch is clearer, whereas figure 7.16 shows a wider frequency range. In all cases, the out-of-band noise has a maximum of 5dB above the non distorted spectrum floor. We can see that the notch has a depth of around 20dB from $\epsilon_r = 10^{-12}$ to $\epsilon_r = 10^{-6}$ corresponding to figures 7.17a to 7.17d. However, for $\epsilon_r = 10^{-4}$ in figure 7.17e, the notch depth becomes less than 20dB. For $\epsilon_r = 10^{-2}$, the notch depth is 20dB once again. In order to understand the reason behind the different notch depths, we need to know which predistortion type is done for each value of $\epsilon_r = 10^{-4}$.

Histogram of the predistortion type

Now, we investigate how often each of the corrections in table 7.1 occur. Figure 7.18 shows the histogram of the type of corrections for different values of ϵ_r. For the lowest value of $\epsilon_r = 10^{-12}$, we can see that the most occurring correction is P3. Compared to P6, P3 occurs more often. This is due to the fact that distorting the radius produces less overall distortion when compared with the toggle which increases the error pulse width and hence increases the overall noise.

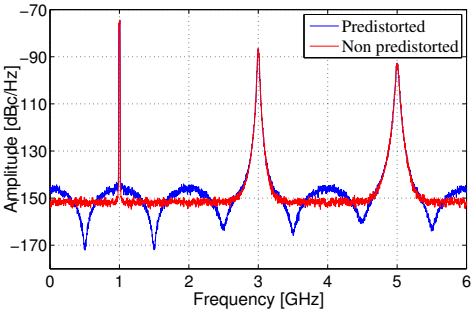

(a) $\epsilon_r = 10^{-12}$

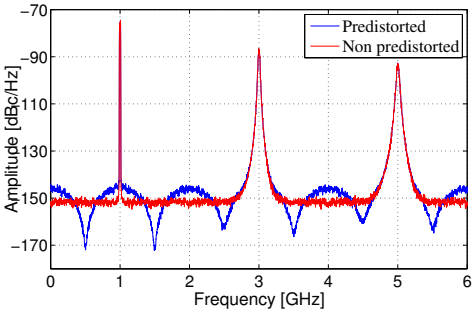

(b) $\epsilon_r = 10^{-10}$

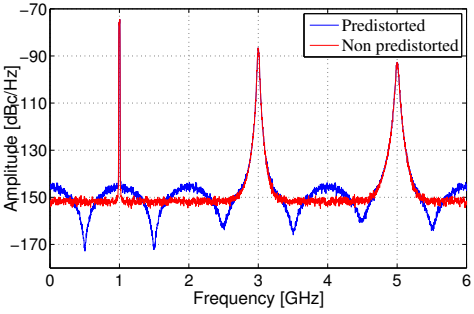

(c) $\epsilon_r = 10^{-8}$

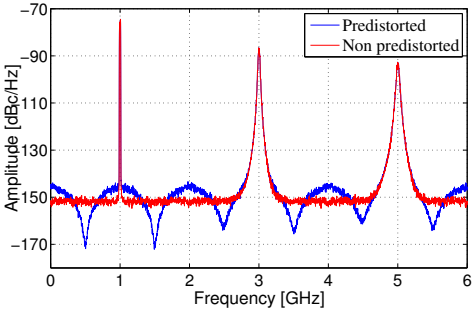

(d) $\epsilon_r = 10^{-6}$

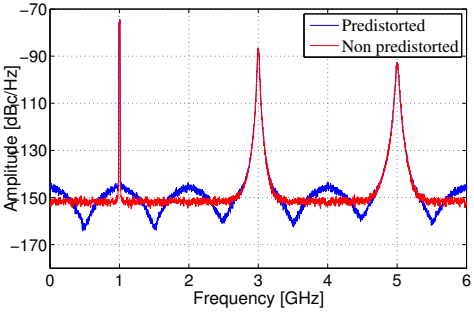

(e) $\epsilon_r = 10^{-4}$

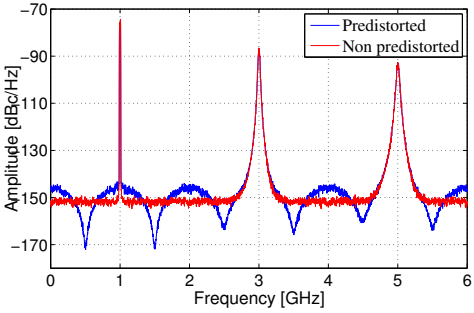

(f) $\epsilon_r = 10^{-2}$

Figure 7.16: Spectrum of the transmitted signal for different ϵ_r with average radius $\mu_r = 9.98 \cdot 10^{-6}$ for the frequency range $0GHz < f < 6GHz$

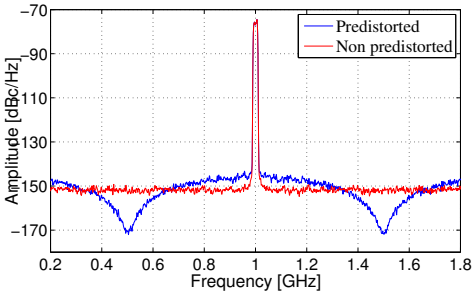

(a) $\epsilon_r = 10^{-12}$

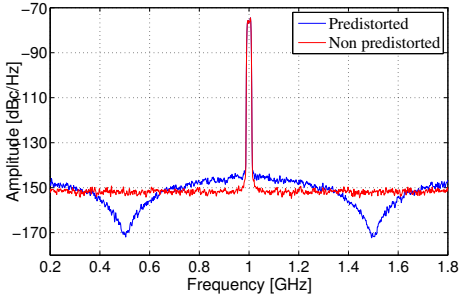

(b) $\epsilon_r = 10^{-10}$

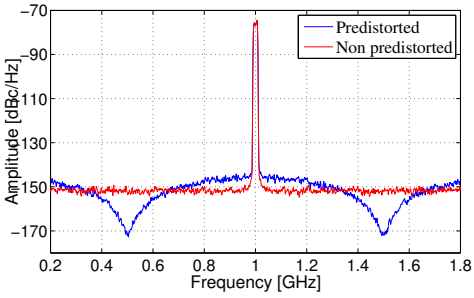

(c) $\epsilon_r = 10^{-8}$

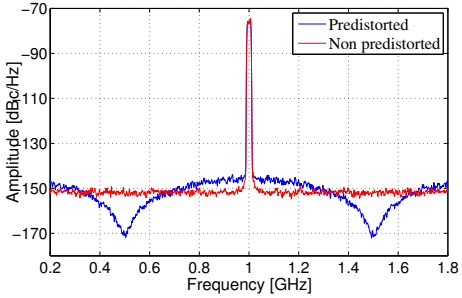

(d) $\epsilon_r = 10^{-6}$

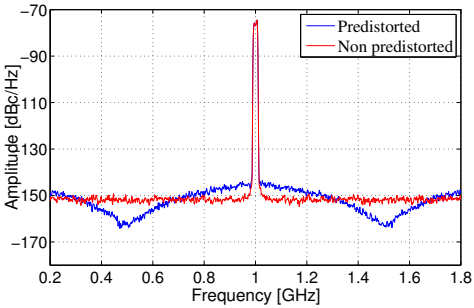

(e) $\epsilon_r = 10^{-4}$

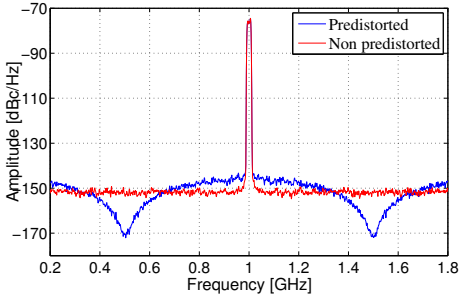

(f) $\epsilon_r = 10^{-2}$

Figure 7.17: Spectrum of the transmitted signal for different ϵ_r with average radius $\mu_r = 9.98 \cdot 10^{-6}$ for the frequency range $0.2GHz < f < 1.8GHz$

The P1 distortion is nearly never used because there will always be a frequency bin to cancel. As ϵ_r increases, the occurrence of P1 also increases. However, P2 and P3 become less probable as ϵ_r increases and are replaced with P1. At $\epsilon_r = 10^{-2}$, P2, P3, P5 and P6 do not occur, because the ϵ_r is too large compared to μ_r.

The fact that we no longer need ϵ_r corrections is actually quite useful. Since in figure 7.17f we see that we already have a deep notch, then there is no need to consider the ϵ_r correction for the radius signal at all. Now, we can limit our distortion to P4 at the frequency bin monitoring block in figure 7.14. This greatly simplifies our block diagram to the one depicted in figure 7.19. Now the radius goes unchanged into the DAC and we save a considerable amount of processing by avoiding checking all possible distortions.

Effect of notch frequency ω_o

Finally, we would like to investigate if the choice of the notch frequency changes the depth of the notch attenuation. In all cases we limit our corrections to P1 and P4. Figures 7.20 and 7.21 show the spectrum of the transmitted signal for f_o ranging from 1 to 1.5 GHz, again for different frequency ranges. We can see that for $f_o = 1$ GHz we do not have a deep attenuation. This is intuitive as our notch is at the in-band frequency which means that the quantization noise is superimposed with the in-band signal. As we proceed further, the notch preserves a 20 dB attenuation. Considering figure 6.16, we see that having a notch depth of 10 dB is already sufficient for spectral mask requirements. It is important to mention that the predistortion algorithm presented in this section tries to filter the quantization noise. The quantization noise is only one component of the out-of-band noise. Other components are the baseband interpolation filters as well as hardware imperfections. Hence, in order to have notches deeper than 20 dB, other imperfections in the modulator chain should be enhanced.

7.4. Discussion

This chapter introduced two algorithms for noise shaping in polar transmitters. The adaptive polar predistortion presented in section 7.2 is basically intended for complex baseband signals. Possible applications of this algorithm is to filter undesired noise components at the receiver side, or for audio applications. Whereas, the error dependent algorithm presented in section 7.3 is intended for a real passband transmit signal which is modulated using the specific polar transmitter architecture discussed in this thesis. Hence, the comparison of both algorithms is not applicable. Generally speaking, having multiple notches in the transmitted signal using the error depend algorithm

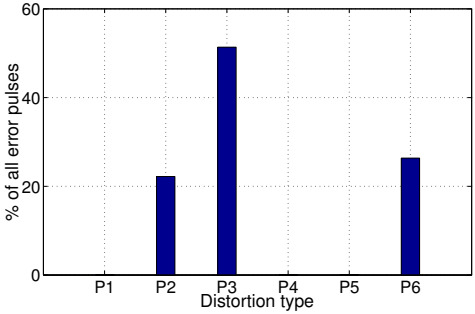

(a) $\epsilon_r = 10^{-12}$

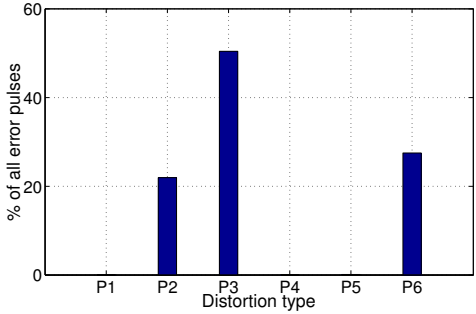

(b) $\epsilon_r = 10^{-10}$

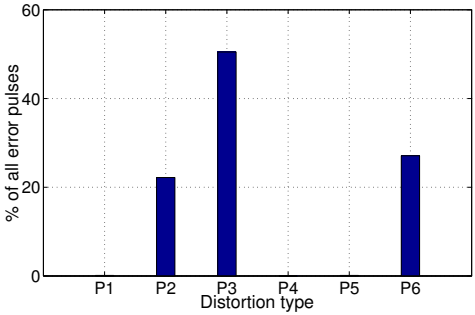

(c) $\epsilon_r = 10^{-8}$

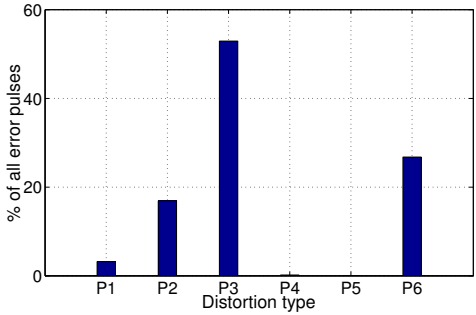

(d) $\epsilon_r = 10^{-6}$

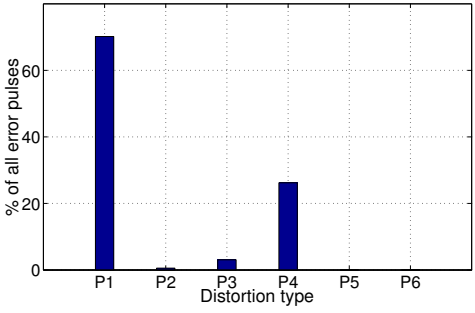

(e) $\epsilon_r = 10^{-4}$

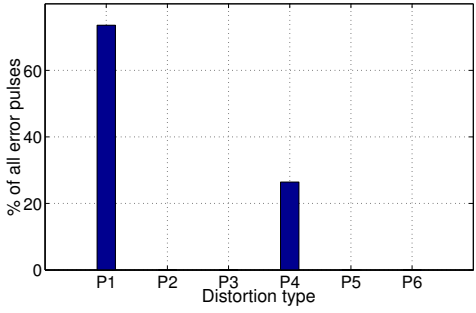

(f) $\epsilon_r = 10^{-2}$

Figure 7.18: Histogram of corrections for different ϵ_r with average radius $\mu_r = 9.98 \cdot 10^{-6}$

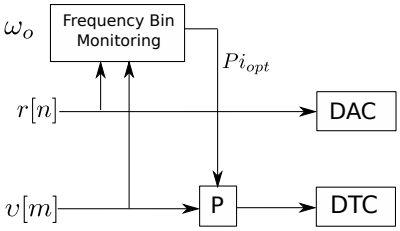

Figure 7.19: Simplified predistortion block diagram with only instantaneous period distortion

can be applied using the same concept explained in section 6.3.3. However, this functionality is not discussed in this chapter due to the increased complexity. For each extra notch, the algorithm needs to consider all possible predistortion types for all notches. Practically speaking, the notch achieved by the error dependent algorithm has a notch width which is wide enough to comply with the spectral mask shown in figure 6.16.

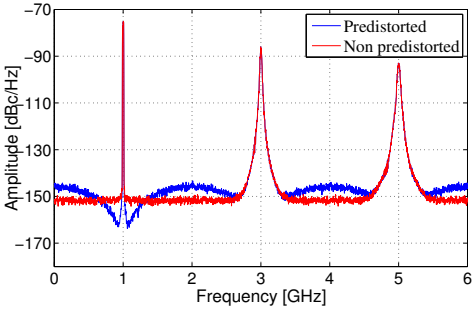

(a) $f_o = 1 \cdot 10^9$

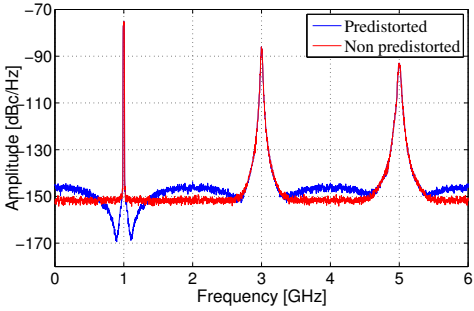

(b) $f_o = 1.1 \cdot 10^9$

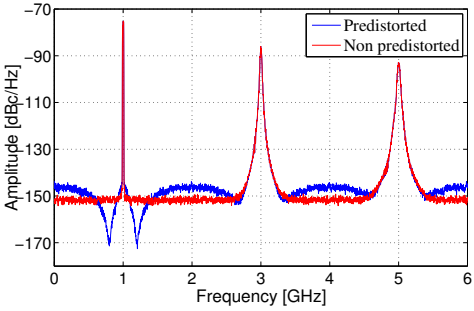

(c) $f_o = 1.2 \cdot 10^9$

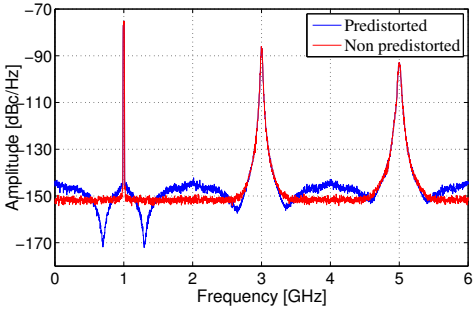

(d) $f_o = 1.3 \cdot 10^9$

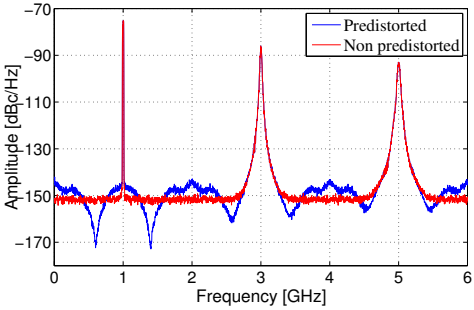

(e) $f_o = 1.4 \cdot 10^9$

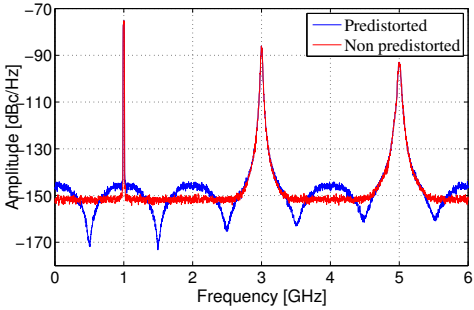

(f) $f_o = 1.5 \cdot 10^9$

Figure 7.20: Spectrum of the transmitted signal for different notch frequencies f_o for the frequency range $0GHz < f < 6GHz$

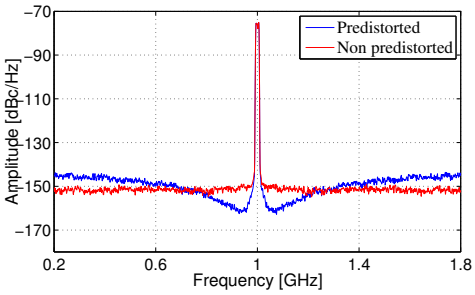

(a) $f_o = 1 \cdot 10^9$

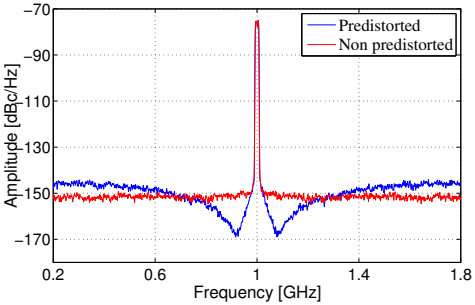

(b) $f_o = 1.1 \cdot 10^9$

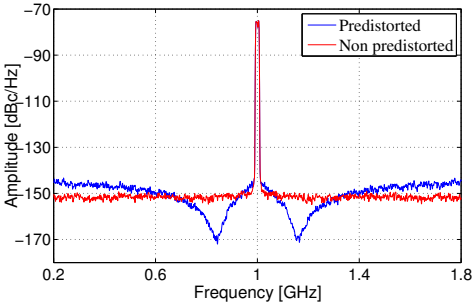

(c) $f_o = 1.2 \cdot 10^9$

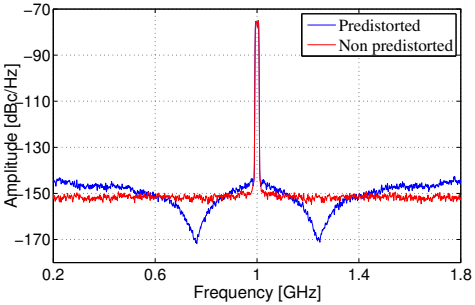

(d) $f_o = 1.3 \cdot 10^9$

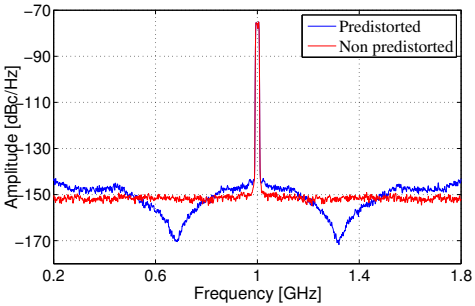

(e) $f_o = 1.4 \cdot 10^9$

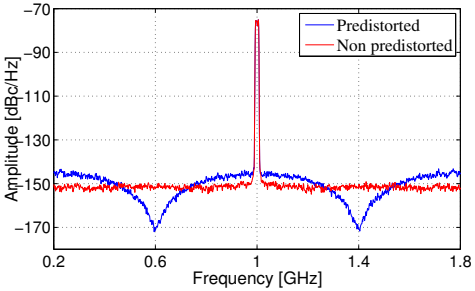

(f) $f_o = 1.5 \cdot 10^9$

Figure 7.21: Spectrum of the transmitted signal for different notch frequencies f_o for the frequency range $0.2GHz < f < 1.8GHz$

8. Conclusion and future work

8.1. Conclusion

This thesis considered the promising architecture of the polar transmitters as a replacement of traditional IQ transmitters. This work introduces two main contributions:

- Analysis of the properties of the polar signals have been done in chapter 3. Analysis of the time quantization in polar transmitters has been presented in section 4.4. Additionally, models of the polar transmitter components and their imperfections, such as DAC and DTC, have been presented.
- The main shortcoming of the polar transmitter which is the excess out-of-band noise has been combated by introducing some novel algorithms. In section 5.4, a novel algorithm has been introduced to trade-off the out-of-band noise spectral level to the sampling rate of the DAC. In chapter 6, a novel general feedforward noise shaping approach has been presented to place notches in the out-of-band noise. In chapter 7, two novel polar predistortion noise shaping algorithms have been presented.

8.2. Future work

The polar transmitter, being a new concept, still has several future challenges that need to be tackled. The following are several possible open topics to be investigated:

- In section 3.4, an analysis of the spectrum of the phase quantization error has been presented. Similarly, in section 4.4, an analysis of the time quantization error has been presented. There is a natural relationship between the phase and instantaneous period. Hence, it would be useful to investigate this relationship. Once this relationship is known, then the instantaneous period can be filtered in a way to ensure a noise-shaped transmitted signal.
- In this thesis, we have assumed a single high sampling rate $f_s = 1$ THz. In some architectures, it is difficult to achieve such high sampling rates and therefore

interpolation techniques are used to estimate some signals such as the instantaneous period. Using this model, the radius signal will arrive at the DAC at a low rate so that the DAC does not do any averaging operations as described in section 5.3. However, in the phase branch, the instantaneous period signal arrives as non-equidistant samples. The synchronization between the equidistant radius signal and non-equidistant instantaneous period signal is an open topic which needs investigation.

- Throughout this thesis, an ideal DTC was assumed, which outputs a phase modulated square wave signal. In reality, the generated signal does not have an exact square shape, but rather a smeared square signal. Additionally, the DTC does not generate a square wave with instantaneous periods exactly equal to the input instantaneous period, but rather introduces some LSB shifts of the instantaneous period. Such imperfections in the DTC can influence the spectrum of the transmitted signal widely, and therefore an analysis of such imperfections is strongly desired.
- The purpose of shaping the out-of-band noise in polar transmitters is to avoid interference between the transmit and received signals. The introduced distortions have raised the spectral level of the out-of-band noise away from the notch frequency. A possible approach to limit such interference is to analyze the received signal and try to modify the out-of-band noise of the transmit signal in a way such that the out-of-band components at the down link frequencies are orthogonal to the received signal. Such joint noise shaping techniques can further enhance the SNR of the downlink signal.

A. Quantization of polar signals

Consider the complex signal

$$s[n] \quad = \quad r[n] \cdot e^{\jmath\theta[n]} \ . \tag{A.1}$$

When the polar coordinates $r[n]$ and $\theta[n]$ are quantized, we yield the quantized complex signal represented as

$$s_q[n] \quad = \quad Q(s[n]) = (r[n] + e_r[n]) \cdot e^{(\jmath\theta[n] + e_\theta[n])} \ . \tag{A.2}$$

The following assumptions are made:

1. $e_r[n]$ and $e_\theta[n]$ are jointly stationary.
2. Mean of $e_r[n]$ and $e_\theta[n]$ are $\mu_{e_r} = 0$ and $\mu_{e_\theta} = 0$, respectively. The covariance function of $e_r[n]$ and $e_\theta[n]$ are $c_{e_r e_r}[n]$ and $c_{e_\theta e_\theta}[n]$, respectively. The covariance spectrum of $e_r[n]$ and $e_\theta[n]$ are $C_{e_r e_r}(\omega)$ and $C_{e_\theta e_\theta}(\omega)$, respectively.
3. $s[n]$, $e_r[n]$, and $e_\theta[n]$ are mutually independent.
4. The quantization errors are small compared to original signals $|e_r[n]| \ll |r[n]|$ and $|e_\theta[n]| \ll |\theta[n]|$.
5. The quantization noise $e_r[n]$ and $e_\theta[n]$ are considered white with variance $\sigma^2_{e_r}$ and $\sigma^2_{e_\theta}$, respectively.

The quantized complex signal can be represented in the form

$$s_q[n] \quad = \quad s[n] + e_s[n] \ , \tag{A.3}$$

where the term $e_s[n]$ comprises the quantization effects of the radius and phase signals. $e_s[n]$ can be denoted as the total quantization error

$$\begin{aligned} e_s[n] \quad &= \quad \frac{ds}{dr} e_r[n] + \frac{ds}{d\theta} e_\theta[n] \\ &= \quad e^{\jmath\theta[n]} e_r[n] + \jmath s[n] e_\theta[n] \\ &= \quad m[n] e_r[n] + \jmath s[n] e_\theta[n] \ . \end{aligned} \tag{A.4}$$

In order to derive the power spectral density of $e_s[n]$, we first derive its autocorrelation function as

$$\begin{aligned} r_{e_s e_s}[n] =& E(e_s[i+n]e_s^*[i]) \\ =& E(m[i+n]m^*[i]e_r[i+n]e_r[i]) \\ &+E(s[i+n]s^*[i]e_\theta[i+n]e_\theta[i]) \\ &+E(-\jmath m[i+n]s^*[i]e_r[i+n]e_\theta[i]) \\ &+E(\jmath s[i+n]m^*[i]e_\theta[i+n]e_r[i]) \ . \end{aligned} \tag{A.5}$$

According to assumption 3, we can formulate equation (A.5) as

$$\begin{aligned} r_{e_s e_s}[n] =& E(m[i+n]m^*[i])E(e_r[i+n]e_r[i]) \\ &+E(s[i+n]s^*[i])E(e_\theta[i+n]e_\theta[i]) \\ &-\jmath E(m[i+n]s^*[i])E(e_r[i+n])E(e_\theta[i]) \\ &+\jmath E(s[i+n]m^*[i])E(e_\theta[i+n])E(e_r[i]) \\ =& r_{mm}[n]r_{e_r e_r}[n] + r_{ss}[n]r_{e_\theta e_\theta}[n] \\ &+\jmath\left(r_{sp}[n] - r_{sp}^*[-n]\right)\mu_{e_r}\mu_{e_\theta} \ . \end{aligned} \tag{A.6}$$

Since $\mu_{e_r} = \mu_{e_\theta} = 0$, then equation (A.6) can be simplified as

$$r_{e_s e_s}[n] \quad = \quad r_{mm}[n]r_{e_r e_r}[n] + r_{ss}[n]r_{e_\theta e_\theta}[n] \ . \tag{A.7}$$

Consequently, the power spectral density of $e_s[n]$ can be represented as

$$R_{e_s e_s}(\omega) \quad = \quad R_{mm}(\omega) * R_{e_r e_r}(\omega) + R_{ss}(\omega) * R_{e_\theta e_\theta}(\omega) \ . \tag{A.8}$$

The spectrum of $m[n]$ can be calculated as

$$R_{mm}(\omega) \quad = \quad \sigma_{mm}^2 = E(|e^{\jmath\theta[n]}|^2) = 1 \tag{A.9}$$

Since $R_{e_\theta e_\theta}(\omega)$ and $R_{e_r e_r}(\omega)$ have constant flat spectra as stated in assumption 5, then we yield

$$R_{e_s e_s}(\omega) \quad = \quad \sigma_{e_r e_r}^2 + \sigma_{ss}^2\sigma_{e_\theta e_\theta}^2 \ . \tag{A.10}$$

B. Square wave harmonics

In this section, we derive the Fourier series of the following square wave

$$\bar{m}(t) = \operatorname{sgn}(\cos(\omega_c t + \theta(t))) \ , \tag{B.1}$$

where $\theta(t)$ is an arbitrary phase and ω_c is the carrier angular frequency.

B.1. Square wave with no modulating phase

Assuming $\theta(t) = 0$, then $\bar{m}(t)$ is periodic and can be represented using its Fourier series as

$$\begin{aligned}\bar{m}(t) &= \sum_{k=-\infty}^{\infty} c_k e^{jk\omega_c t} \\ &= \sum_{k=1,3,\ldots}^{\infty} a_k \cos(k\omega_c t) \\ &= \frac{4}{\pi}\left(\cos(\omega_c t) - \frac{1}{3}\cos(3\omega_c t) + \frac{1}{5}\cos(5\omega_c t) + \ldots\right) \ ,\end{aligned} \tag{B.2}$$

with

$$c_k = c_{-k} = \begin{cases} \frac{2}{\pi}(-1)^{l-1}\frac{1}{2l-1} \quad k = 2l-1 & \text{odd numbers,} \\ 0 & \text{even numbers,} \end{cases} \tag{B.3}$$

and

$$a_k = 2c_k \ . \tag{B.4}$$

B.2. Square wave with arbitrary modulating phase

Now assume that the baseband phase $\theta(t)$ is arbitrary and varying. The phase modulated signal can be represented as

$$m(t) = \cos(\omega_c t + \theta(t)) \ . \tag{B.5}$$

In this case, $m(t)$ is no longer a periodic signal and there is no Fourier series representation for $m(t)$. However, it will be shown that $m(t)$ can be written in a Fourier series like expression.
Assume that $\theta(t)$ is first approximated by a piecewise constant signal. Then $m(t)$ can be represented as

$$m(t) = \sum_{l=-\infty}^{\infty} \cos(\omega_c t + \theta_l) r_l(t) \ , \tag{B.6}$$

where

$$r_l(t) = \begin{cases} 1 & \text{when} \quad t \in D_l \ , \\ 0 & \text{when} \quad t \notin D_l \ , \end{cases} \tag{B.7}$$

where D_l is the time range of the l-th window, with

$$\sum_{l=-\infty}^{\infty} r_l(t) = 1 \qquad \forall t \ . \tag{B.8}$$

The square wave signal can then be represented as

$$\begin{aligned} \bar{m}(t) =& \text{sgn}(m(t)) = \text{sgn}(\sum_{l=-\infty}^{\infty} \cos(\omega_c t + \theta_l) r_l(t)) \\ &= \sum_{l=-\infty}^{\infty} \text{sgn}(\cos(\omega_c t + \theta_l)) r_l(t) \\ &= \sum_{l=-\infty}^{\infty} \left(\sum_{k=1,3,\ldots}^{\infty} a_k \cos(k\omega_c t + k\theta_l) \right) r_l(t) \\ &= \sum_{l=-\infty}^{\infty} \left(\sum_{k=\pm 1,\pm 3,\ldots}^{\infty} c_k e^{jk\theta_l} e^{jk\omega_c t} \right) r_l(t) \\ &= \sum_{k=\pm 1,\pm 3,\ldots}^{\infty} c_k \left(\sum_{l=-\infty}^{\infty} e^{jk\theta_l} r_l(t) \right) e^{jk\omega_c t} \ . \end{aligned} \tag{B.9}$$

The term $\sum_{l=-\infty}^{\infty} e^{jk\theta_l} r_l(t)$ can be simplified as

$$\begin{aligned} \sum_{l=-\infty}^{\infty} e^{jk\theta_l} r_l(t) &= \sum_{l=-\infty}^{\infty} e^{jk\theta(t)} r_l(t) \\ &= e^{jk\theta(t)} \sum_{l=-\infty}^{\infty} r_l(t) \\ &= e^{jk\theta(t)} \ . \end{aligned} \tag{B.10}$$

By substituting equation (B.10) in equation (B.9), we yield

$$\begin{aligned}\bar{m}(t) &= \sum_{k=\pm1,\pm3,\ldots}^{\infty} c_k e^{jk(\omega_c t+\theta(t))} \\ &= \sum_{k=\pm1,\pm3,\ldots}^{\infty} a_k \cos(k\omega_c t + k\theta(t)) \ . \end{aligned} \tag{B.11}$$

The derivation of equation (B.11) assumed that $\theta(t)$ is a stepwise function. Since the windows D_l can be arbitrary small, then each part of $\theta(t)$ can be approximated by a stepwise phase with arbitrary precision. Hence, equation (B.11) applies for any phase signal. It is worth noting that this is not a Fourier series, since $\bar{m}(t)$ is not a periodic signal. This decomposition approach is useful for spectral analysis.

Bibliography

3GPP. Lte; evolved universal terrestrial radio access (e-utra);user equipment (ue) radio transmission and reception (3gpp ts 36.101 version 8.23.0 release 8). TS 36.101, 3rd Generation Partnership Project (3GPP), January 2014. URL http://www.3gpp.org/DynaReport/36101.htm.

W. Ahmed. Out-of-band quantization noise suppression in direct digital-to-rf transmitter architechtures. In *Signal Processing and Information Technology, 2007 IEEE International Symposium on*, pages 1094–1099, 2007. doi: 10.1109/ISSPIT.2007.4458110.

S. Al-Ahdab, A. Mantyniemi, and J. Kostamovaara. A 12-bit digital-to-time converter (dtc) for time-to-digital converter (tdc) and other time domain signal processing applications. In *NORCHIP, 2010*, pages 1–4, 2010. doi: 10.1109/NORCHIP.2010.5669491.

M. Antonini, M. Barlaud, P. Mathieu, and I. Daubechies. Image coding using wavelet transform. *Image Processing, IEEE Transactions on*, 1(2):205–220, 1992.

I. Ban, U.E. Avci, D.L. Kencke, and P. L D Chang. A scaled floating body cell (fbc) memory with high-k+metal gate on thin-silicon and thin-box for 16-nm technology node and beyond. In *VLSI Technology, 2008 Symposium on*, pages 92–93, 2008. doi: 10.1109/VLSIT.2008.4588575.

I. Bashir, R.B. Staszewski, O. Eliezer, B. Banerjee, and P.T. Balsara. A novel approach for mitigation of rf oscillator pulling in a polar transmitter. *Solid-State Circuits, IEEE Journal of*, 46(2):403–415, Feb 2011. ISSN 0018-9200. doi: 10.1109/JSSC.2010.2096110.

D. Belson. Akamai's state of the internet q1 report. Technical Report 1, 2014. URL http://www.akamai.com/.

Z. Boos, A. Menkhoff, F. Kuttner, M. Schimper, J. Moreira, H. Geltinger, T. Gossmann, P. Pfann, A. Belitzer, and T. Bauernfeind. A fully digital multimode polar transmitter employing 17b rf dac in 3g mode. In *Solid-State Circuits Conference Digest of Technical Papers (ISSCC), 2011 IEEE International*, pages 376–378, Feb 2011. doi: 10.1109/ISSCC.2011.5746361.

J.K. Cavers. Amplifier linearization using a digital predistorter with fast adaptation and low memory requirements. *Vehicular Technology, IEEE Transactions on*, 39(4): 374–382, Nov 1990. ISSN 0018-9545. doi: 10.1109/25.61359.

Cisco. Cisco visual networking index: Global mobile data traffic forecast 2013 - 2018. Technical report, February 2014. URL http://www.cisco.com/.

M. Clara. *High-Performance D/A-Converters: Application to Digital Transceivers*. Springer, 2013.

M. Cooper, R.W. Dronsuth, A.J. Leitich, J.C.N. Lynk, J.J. Mikulski, J.F. Mitchell, R.A. Richardson, and J.H. Sangster. Radio telephone system, September 16 1975. URL http://www.google.com/patents/US3906166. US Patent 3,906,166.

L. Ding, G.T. Zhou, D.R. Morgan, Zhengxiang Ma, J.S. Kenney, Jaehyeong Kim, and C.R. Giardina. A robust digital baseband predistorter constructed using memory polynomials. *Communications, IEEE Transactions on*, 52(1):159–165, Jan 2004. ISSN 0090-6778. doi: 10.1109/TCOMM.2003.822188.

S. Eto, H. Akita, K. Isobe, K. Tsuchida, H. Toda, and T. Seki. A 333 mhz, 20 mw, 18 ps resolution digital dll using current-controlled delay with parallel variable resistor dac (pvr-dac). In *ASICs, 2000. AP-ASIC 2000. Proceedings of the Second IEEE Asia Pacific Conference on*, pages 349–350, 2000. doi: 10.1109/APASIC.2000.896980.

A. Gersho and Robert M. Gray. *Vector quantization and signal compression*. Kluwer Academic Publishers, Boston [u.a.], 1992. ISBN 0-7923-9181-0.

A. Ghosh, R. Ratasuk, B. Mondal, N. Mangalvedhe, and T. Thomas. Lte-advanced: next-generation wireless broadband technology [invited paper]. *Wireless Communications, IEEE*, 17(3):10–22, June 2010. ISSN 1536-1284. doi: 10.1109/MWC.2010.5490974.

B.P. Ginsburg and A.P. Chandrakasan. 500-ms/s 5-bit adc in 65-nm cmos with split capacitor array dac. *Solid-State Circuits, IEEE Journal of*, 42(4):739–747, April 2007. ISSN 0018-9200. doi: 10.1109/JSSC.2007.892169.

J. Groe. Polar transmitters for wireless communications. *Communications Magazine, IEEE*, 45(9):58–63, 2007. ISSN 0163-6804. doi: 10.1109/MCOM.2007.4342857.

J. Herre. Temporal noise shaping, qualtization and coding methods in perceptual audio coding: A tutorial introduction. In *Audio Engineering Society Conference: 17th International Conference: High-Quality Audio Coding*. Audio Engineering Society, 1999.

C. Hyunseok and H. Songcheol. A digital polar cmos power amplifier with a 102-db power dynamic range using a digitally controlled bias generator. *Microwave Theory*

and Techniques, IEEE Transactions on, 62(3):579–589, March 2014. ISSN 0018-9480. doi: 10.1109/TMTT.2014.2298386.

M. Ibrahim and Menkhoff A. A modulator and a method for generating a modulated signal (filed patent), 2014a.

M. Ibrahim and Menkhoff A. Feed forward noise shaping (filed patent), 2014b.

M. Ibrahim and Menkhoff A. A predistortion circuit for noise shaping in polar transmitters (filed patent), 2015.

M. Ibrahim and B. Yang. A theoretical analysis of frequency/time quantization noise in polar transmitters. In *Telecommunications Symposium (ITS), 2014 International*, pages 1–5, Aug 2014a. doi: 10.1109/ITS.2014.6947962.

M. Ibrahim and B. Yang. A theoretical study of the statistical and spectral properties of polar transmitter signals. In *Circuits and Systems (ISCAS), 2014 IEEE International Symposium on*, June 2014b.

M. Ibrahim, B. Yang, and A. Menkhoff. Oversampled digital-to-analog converter for noise reduction in polar transmitters. In *Signal Processing (ICSP), 2014 12th International Conference on*, pages 1531–1536, Oct 2014. doi: 10.1109/ICOSP.2014.7015254.

G. Junqing, A.F. Aref, and R. Negra. Analysis of design specification for digital polar rf transmitter at system and architectural level. In *Radio and Wireless Symposium (RWS), 2012 IEEE*, pages 443–446, Jan 2012. doi: 10.1109/RWS.2012.6175395.

L.R. Kahn. Single-sideband transmission by envelope elimination and restoration. *Proceedings of the IRE*, 40(7):803–806, July 1952. ISSN 0096-8390. doi: 10.1109/JRPROC.1952.273844.

J. Lopez, Yan Li, J.D. Popp, D.Y.-C. Lie, Chia-Chang Chuang, K. Chen, S. Wu, Tzu-Yin Yang, and Gin-Kou Ma. Design of highly efficient wideband rf polar transmitters using the envelope-tracking technique. *Solid-State Circuits, IEEE Journal of*, 44(9):2276–2294, Sept 2009. ISSN 0018-9200. doi: 10.1109/JSSC.2009.2022669.

D. K. C. MacDonald. Some statistical properties of random noise. *Proc. Cambridge Philosophical Society*, 45:368–372, Dec 1948.

D. Meeker, M. and L. Wu. Internet trends. Technical report, 5 2013. URL http://www.kpcb.com/insights/2013-internet-trends.

G. Moore. Moore's law — Wikipedia, the free encyclopedia. URL https://en.wikipedia.org/wiki/Moore%27s_law. [Online; accessed 8-November-2015].

S.R. Norsworthy, R. Schreier, G.C. Temes, and IEEE Circuit & Systems Society. *Delta-Sigma data converters: theory, design, and simulation*. IEEE Press, 1997. ISBN 9780780310452.

J.C. Pedro, J.A. Garcia, and P.M. Cabral. Nonlinear distortion analysis of polar transmitters. *Microwave Theory and Techniques, IEEE Transactions on*, 55(12):2757–2765, Dec 2007. ISSN 0018-9480. doi: 10.1109/TMTT.2007.909145.

R. Price. A note on the envelope and phase-modulated components of narrow-band gaussian noise. *Information Theory, IRE Transactions on*, 1(2):9–13, September 1955. ISSN 0096-1000. doi: 10.1109/TIT.1955.1055130.

F.H. Raab. Intermodulation distortion in kahn-technique transmitters. *Microwave Theory and Techniques, IEEE Transactions on*, 44(12):2273–2278, Dec 1996. ISSN 0018-9480. doi: 10.1109/22.556466.

F. Rezzi, I. Bietti, M. Cazzaniga, and R. Castello. A 70-mw seventh-order filter with 7-50 mhz cutoff frequency and programmable boost and group delay equalization. *Solid-State Circuits, IEEE Journal of*, 32(12):1987–1999, Dec 1997. ISSN 0018-9200. doi: 10.1109/4.643657.

S.O. Rice. Mathematical analysis of random noise. *Bell System Technical Journal, The*, 23(3):282–332, July 1944. ISSN 0005-8580. doi: 10.1002/j.1538-7305.1944.tb00874.x.

S.O. Rice. Mathematical analysis of random noise. *Bell System Technical Journal, The*, 24(1):46–156, Jan 1945. ISSN 0005-8580. doi: 10.1002/j.1538-7305.1945.tb00453.x.

D. Rudolph. Out-of-band emissions of digital transmissions using kahn eer technique. *Microwave Theory and Techniques, IEEE Transactions on*, 50(8):1979–1983, Aug 2002. ISSN 0018-9480. doi: 10.1109/TMTT.2002.801349.

D. Rudolph. Kahn eer technique with single-carrier digital modulations. *Microwave Theory and Techniques, IEEE Transactions on*, 51(2):548–552, Feb 2003. ISSN 0018-9480. doi: 10.1109/TMTT.2002.807810.

A. Shameli, A. Safarian, A. Rofougaran, M. Rofougaran, and F. De Flaviis. A novel dac based switching power amplifier for polar transmitter. In *Custom Integrated Circuits Conference, 2006. CICC '06. IEEE*, pages 137–140, Sept 2006. doi: 10.1109/CICC.2006.320851.

R. Staszewski, J. Wallberg, S. Rezeq, C. Hung, O. Eliezer, S. Vemulapalli, C. Fernando, K. Maggio, R. Staszewski, N. Barton, et al. All-digital pll and transmitter for mobile phones. *Solid-State Circuits, IEEE Journal of*, 40(12):2469–2482, 2005a.

R.B. Staszewski, Chih-Ming Hung, N. Barton, Meng-Chang Lee, and D. Leipold. A digitally controlled oscillator in a 90 nm digital cmos process for mobile phones. *Solid-State Circuits, IEEE Journal of*, 40(11):2203–2211, 2005b. ISSN 0018-9200. doi: 10.1109/JSSC.2005.857359.

R.B. Staszewski, K. Muhammad, and D. Leipold. Digital rf processing techniques for soc radios (invited). In *System-on-Chip for Real-Time Applications, 2005. Proceedings. Fifth International Workshop on*, pages 217–222, July 2005c. doi: 10.1109/IWSOC.2005.54.

R.B. Staszewski, D. Leipold, O. Eliezer, M. Entezari, K. Muhammad, I Bashir, C. M Hung, J. Wallberg, R. Staszewski, P. Cruise, S. Rezeq, S. Vemulapalli, K. Waheed, N. Barton, M. C Lee, C. Fernando, K. Maggio, T. Jung, I Elahi, S. Larson, T. Murphy, G. Feygin, I Deng, T. Mayhugh, Y. C Ho, K. M Low, C. Lin, J. Jaehnig, J. Kerr, J. Mehta, S. Glock, T. Almholt, and S. Bhatara. A 24mm2 quad-band single-chip gsm radio with transmitter calibration in 90nm digital cmos. In *Solid-State Circuits Conference, 2008. ISSCC 2008. Digest of Technical Papers. IEEE International*, pages 208–607, Feb 2008. doi: 10.1109/ISSCC.2008.4523130.

I. Syllaios, P.T. Balsara, and R.B. Staszewski. Envelope and phase path recombination in adpll-based wideband polar transmitters. In *Circuits and Systems Workshop: System-on-Chip - Design, Applications, Integration, and Software, 2008 IEEE Dallas*, pages 1–4, Oct 2008. doi: 10.1109/DCAS.2008.4695931.

R. Van de Plassche. *Integrated Analog-to-Digital and Digital-to-Analog converters*. Kluwer Academic Publishers, 1994.

B. Widrow and I. Kollár. *Quantization Noise: Roundoff Error in Digital Computation, Signal Processing, Control, and Communications*. Cambridge University Press, 2008. ISBN 9781139472845. URL http://books.google.fr/books?id=8q-xcGeEJDwC.

C. Yong-Chang, S. Yoo, and Y. Hyung-Joun. A fully digital polar transmitter using a digital-to-time converter for high data rate system. In *Radio-Frequency Integration Technology, 2009. RFIT 2009. IEEE International Symposium on*, pages 56–59, 2009. doi: 10.1109/RFIT.2009.5383681.

Y. Zhou and J. Yuan. An 8-bit 100-mhz cmos linear interpolation dac. *Solid-State Circuits, IEEE Journal of*, 38(10):1758–1761, 2003. ISSN 0018-9200. doi: 10.1109/JSSC.2003.817593.